Thermal-Hydraulic Performance Evaluation and Optimization of the T-Tube Divertor Design Using Numerical Simulations

A Dissertation
Presented to
The Academic Faculty

by

Sercan Akdeniz

In Partial Fulfillment
of the Requirements for the Degree
Master of Science in Mechanical Engineering

Georgia Institute of Technology

August 2017

Thermal-Hydraulic Performance Evaluation and Optimization of the T-Tube Divertor Design Using Numerical Simulations

Approved by:

Dr. Said I. Abdel-Khalik, , Co-advisor
School of Mechanical Engineering
Georgia Institute of Technology

Dr. Minami Yoda, Co-advisor
School of Mechanical Engineering
Georgia Institute of Technology

Dr. Dennis L. Youchison
Fusion Energy Divison
Oak Ridge National Laboratory

Date Approved: 07/17/2017

ACKNOWLEDGEMENTS

First of all, I would like to express my gratitude and appreciation to my co-advisors Drs. Said I. Abdel-Khalik and Minami Yoda for their invaluable advice and help throughout the process of successfully completing my degree. I could not have completed this overwhelming work in such a limited time without their guidance and support. I would also like to thank my committee member Dr. Dennis L. Youchison for his contributions to this thesis.

My colleagues Bailey Zhao and Shekaib Musa deserve an acknowledgment for their assistance in the laboratory, and for their companionship. They made my experience at Georgia Tech more enjoyable.

This page would not be complete without a praise to my brother, who guided me through all the process from the beginning to the end, and encouraged me to apply to Georgia Tech as a former holder of the same fellowship.

I would like to thank Dr. Juergen Rapp for making my stay at ORNL effortless and delightful. Direct contact with the ORNL employees made discussions more efficient.

Last but not least, I would like to thank Turkish Petroleum Corporation (TP) and its venerable employees for deeming me worthy of the fellowship, and giving their full support whenever I need.

TABLE OF CONTENTS

LIST OF TABLES

LIST OF FIGURES

LIST OF SYMBOLS AND ABBREVIATIONS

Variable	Definition	Units
$\bar{V}$	Average velocity at the slot	m/s
Nu	Local Nusselt number	-
$\overline{Nu}$	Average Nusselt number	-
Re	Reynolds number	-
Pr	Prandtl number	-
D_h	Hydraulic diameter	m
H	Nozzle-to-plate distance	m
d	Diameter of circular jet	m
W	Width of slot jet	m
A_{slot}	Slot cross-section area	m^2
ρ	Density	kg/m^3
$q"$	Heat flux	W/m^2
h	Convective heat transfer coefficient	$W/m^2 \cdot K$
ε	Turbulent dissipation rate	m^2/s^3
κ	Turbulent kinetic energy	m^2/s^2
u'	Fluctuation in velocity	m/s
$\bar{u}$	Time-averaged velocity	m/s
C_p	Specific heat	$kJ/kg \cdot K$
k	Thermal conductivity of fluid	$W/m \cdot K$
λ	Thermal conductivity of solid	$W/m \cdot K$
α	Thermal diffusivity	m^2/s

$q"_{rad}$	Radiative heat flux	W/m^2
ε_{rad}	Emissivity	-
σ	Stefan-Boltzman constant	$W/m^2 \cdot K^4$
F_{rad}	Shape factor	-
I	Turbulent intensity	-
l	Turbulence length scale	m
Ma	Mach number	-
$\dot{m}$	Mass flow rate	kg/s
T_∞	Inlet temperature	K
T_w	Wall temperature	K
T_0	Reference temperature	K
$T_{s,avg}$	Average surface temperature	K
y^+	Dimensionless distance from the wall	-
τ_w	Wall shear stress	Pa
V_f	Friction velocity	m/s
ν	Kinematic viscosity	m^2/s
μ_t	Eddy viscosity	m^2/s
μ	Dynamic viscosity	Pa·s

SUMMARY

A key technology issue in magnetic fusion energy is plasma-materials interactions (PMI). Because our understanding of how materials change when exposed to burning plasmas over extended periods is limited, Oak Ridge National Laboratory (ORNL) has proposed a linear plasma simulator, the Material-Plasma Exposure eXperiment (MPEX), to test various fusion-relevant materials. Since this facility will expose various materials to conditions similar to those in a burning plasma (except for fusion-relevant neutrons) at steady state, effectively cooling the target plate which will be exposed to steady-state heat fluxes of several MW/m^2 is a major challenge. The objective of this Master's thesis is to use numerical simulation to evaluate and improve the thermal-hydraulic performance of a helium-cooled divertor design adapted for cooling the target plate in a linear plasma simulator.

The T-tube divertor design, originally developed by the Advanced Reactor Innovations and Evaluations Compact Stellarator Study (ARIES-CS), was used as the starting point for these simulations because it can withstand a uniform heat flux of 10 MW/m^2 over an area of several cm^2 when cooled by helium (He) at 10 MPa and 600 °C. The T-tube was adapted for cooling the proposed target plate design for the MPEX using He at 4 MPa and room temperature. Given the much lower coolant temperatures, the simulations considered a target plate consisting of a copper chromium zirconium (CuCrZr) alloy, *vs.* the tungsten alloy proposed for the original T-tube.

The simulations considered two different He flow configurations; a number of modified geometries were evaluated in an attempt to improve the thermal-hydraulic performance of both configurations. The simulations also compared the performance of two different target plate materials, namely the original CuCrZr and a titanium zirconium molybdenum (TZM) alloy.

CHAPTER 1. INTRODUCTION

1.1 Introduction and Motivation

The first estimates of the Earth's total energy resources date from the 1920s [1]. The results of such studies have often been controversial, and have been repeatedly revised, usually increasing over time. Nevertheless, we know that we will run out of fossil fuels at some point, and the only question is 'when?' Another important issue for fossil fuels is that they are hydrocarbons, and burning these hydrocarbons produces carbon dioxide (CO_2). Using fossil fuels therefore contributes to global climate change by increasing the amount of CO_2 in the atmosphere. In the long term, finding a clean and reliable energy source is the only way to meet the world's energy demands.

Nuclear fission has been used to generate electricity since the first grid-connected power plant was commissioned in 1954 [2]. Nuclear fission does not contribute to climate change and is relatively safe, reliable, cost-effective and does not suffer from a scarcity of fuel; however, accidents such as Three Mile Island, Chernobyl, and most recently, Fukushima, have raised safety concerns and made countries reconsider fission as a carbon-free energy source. A promising carbon-free alternative that has the potential to provide energy on demand without the intermittency problems and storage issues associated with solar or wind power is nuclear fusion. Indeed, scientists believe that nuclear fusion can meet the world's energy demands for the foreseeable future if nuclear fusion energy can be made practical.

Although no nuclear fusion power plants have been built to date, fusion reactors in theory have a number of advantages over fission reactors. First of all, the fusion reaction is not supercritical. If the fuel supply is cut off, there is no material to continuously generate heat, which can and has been an issue in fission reactor accidents. Second, the products of the fusion reaction, while radioactive, are neither as highly radioactive, nor as long-lived, as the waste from fission reactors. Although the reactor materials become mildly radioactive, the primary byproduct of the fuel is inert helium. Finally, the fuels used in fusion are naturally abundant, or can be produced from naturally abundant precursors, and are easier to process, so fusion, unlike fission, does not require complex and costly enrichment facilities [3].

Preliminary theories about fusion were proposed in the early 20^{th} century, but these theories could not be proven until Edward Teller, inventor of the hydrogen bomb, discovered that deuterium (D) and tritium (T) can react at a relatively low activation threshold and release huge amounts of energy [4]. Even though the D-T reaction has been achieved, there remain many challenges before fusion can be used to generate electricity. Fusion power and fusion-related research thus remains an active area. Numerous designs for fusion power plants have been proposed and evaluated. Although there are two major approaches for achieving fusion, namely magnetic confinement and inertial confinement, magnetic confinement fusion energy (MFE) is the focus of this thesis.

Building a viable MFE reactor requires overcoming numerous challenges in both plasma physics and fusion technology. This thesis focuses on a specific challenge in fusion technology, namely plasma-material interactions (PMI), *i.e.*, the materials challenges due to the interaction of the very hot (with temperatures as great as 10^8 K) plasma inside the

reactor with the surrounding materials. Escaping particles and radiation from the plasma greatly restrict the number of materials that can be used for the interior wall of the reactor, and critical components need to have relatively long lifetimes to be a cost-effective solution.

This thesis specifically builds upon previous work at Georgia Tech of the thermal-hydraulic performance of gas-cooled divertors. The divertor "purifies" the plasma and makes long-term fusion possible by removing heat and byproducts of the fusion reaction from the reaction chamber [5]. This work focuses upon evaluating whether a specific design proposed by Advanced Research Innovation and Evaluation Study (ARIES) team, the helium-cooled T-tube divertor [6], can be used to cool materials samples exposed to fusion-relevant plasmas in a linear plasma simulator facility under development at Oak Ridge National Laboratory (ORNL), Material Plasma Exposure eXperiment (MPEX) [7], as detailed later in this chapter.

1.2 Fusion Energy and Magnetic Confinement

This section starts with a brief introduction to fusion energy and magnetic confinement fusion. The role and importance of plasma-facing materials will then be introduced. Finally, recent experimental work on PMI will be reviewed, focusing on the divertor.

Fusion is the process where two lighter nuclei merge, or "fuse," to form a heavier single nucleus while releasing tremendous amounts of energy. Figure 1.1 shows the binding energy per nucleon of each element in terms of its mass number.

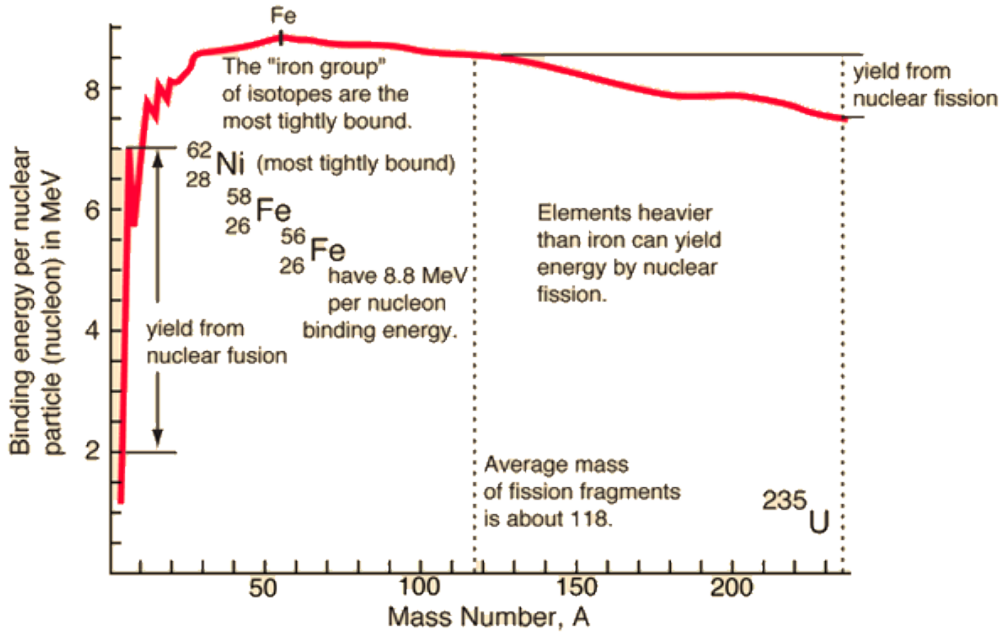

Figure 1.1 Binding energy per nucleon for each element [8]

Because energy is released, the two nuclei that fuse should have lower binding energies per nucleon than the resulting heavier nucleus. In other words, the energy released will be equal to the mass difference between the reactants and the products of the fusion reaction. Usually nuclei having atomic numbers less than 26, *i.e.*, Iron (Fe), can fuse because the peak at the energy curve occurs at Fe (with the exception of Ni-62, Fe has the highest binding energy per nucleon). However, if external energy is added, heavier nuclei can also undergo fusion reactions. Present nuclear power plants use the fission reaction, which is the reverse of nuclear fusion. Two lighter nuclei that are disintegrated from one heavier nucleus usually have atomic numbers greater than Fe in order to release energy.

The yield from each respective reaction type is directly related to the difference in the binding energy. As shown in Figure 1.1, in case of lower atomic numbers, the yield from fusion reactions may be more than the yield from fission reactions. The remarkably high yield of hydrogen nuclei make hydrogen isotopes leading candidates for fusion reactions.

Under normal conditions, the nuclei cannot get close enough due to Coulombic repulsion to fuse, so they must be heated to a critical temperature to overcome this repulsion, or the Coulomb barrier, within the nucleus. The state of this heated material, consisting of mostly ionized molecules, is known as a plasma [9]. Hydrogen isotopes with an atomic, or mass, number $A = 1$ have the smallest Coulomb barrier. Considering the large potential yield of helium fusion from Figure 1.1 and the relatively low Coulomb barrier of hydrogen isotopes, the fusion of hydrogen isotopes to produce a helium nucleus is a promising candidate for fusion power. Note that classical mechanics estimates of the energy required to overcome the Coulomb barrier are greatly reduced by the quantum mechanics-based assumption of finite probability that the particle will tunnel through the barrier [10].

In our sun, which is the best object to exemplify a fusion reactor, a complex chain reaction, called the proton-proton chain reaction, takes place, resulting in a net output of close to 25 MeV [8]. The sun uses its huge gravitational force to create large plasma densities at its core to start and maintain a fusion chain reaction. In this way, the Coulomb barrier can be exceeded by thermally energized nuclei, thanks to the gravitational force that confines plasma. Yet, it is not practical to create a gravitational force on the Earth equal to that in the sun, whose mass is 330,000 times that of our planet; therefore another way should be devised. While the temperature requirement for a self-sufficient fusion reaction

on the Earth is around 100 million K, this requirement is around 15 million K in the sun [10]. As mentioned before, two widely used techniques to sustain a fusion reaction on earth are magnetic and inertial confinement.

There are many possible fusion reactions, as can be seen in Table 1. However, for fusion power, scientists believe at present that the deuterium-tritium (D-T) reaction is the most promising because of its energy yield, activation threshold and the plentiful supply of deuterium.

Table 1 Nuclear reactions of interest [3]

Name	Abbreviation	Reaction (energy, MeV)	Total (MeV)	Energy (10^{-12} J)
DT	T(d,n)^{4}He	D + T → ^{4}He(3.54) + n(14.05)	17.59	2.818
DDn	D(d,n)^{3}He	D + D → ^{3}He(0.82) + n(2.45)	3.27	0.524
DDp	D(d,p)T	D + D → T(1.01) + p(3.02)	4.03	0.646
TT	T(t,2n) ^{4}He	T + T → n + n + ^{4}He	11.3	1.81
D-^{3}He	^{3}He(d,p) ^{4}He	D + ^{3}He → ^{4}He(3.66) + p(14.6)	18.3	2.93
p-^{6}Li	^{6}Li(p,α) ^{3}He	^{6}Li + p → ^{4}He + ^{3}He	4.02	0.644
p-^{11}B	^{11}B(p,2α)^{4}He	^{11}B + p → 3(^{4}He)	8.68	1.39
Reactions for breeding tritium (Natural lithium = 7.42 % ^{6}Li and 92.58 % ^{7}Li)				
n-^{6}Li	^{6}Li(n,α)T	^{6}Li + n(thermal) → ^{4}He(2.05) + T(2.73)	4.78	0.766
n-^{7}Li	^{7}Li(n,n′+α)T	^{7}Li + n(fast) → T + ^{4}He + n	−2.47 (endothermic)	−0.396

$$\mathbf{{}_1^2D + {}_1^3T = {}_2^4He(3.54\ MeV) + {}_0^1n(14.05\ MeV)} \qquad \mathbf{(1)}$$

For the D-T reaction (1), the activation energy is 4.4 keV, *vs.* 48 keV for the D-D reaction. This difference makes it much easier to initiate the D-T reaction. Deuterium is a naturally occurring stable hydrogen isotope, and can be found in water, at a trace level of 0.0015%. Given the vast amount of water available in the oceans, the supply of D appears

to be effectively infinite. On the other hand, T is a short-lived radioactive hydrogen isotope, so it must be bred, via neutron absorption by lithium, for example. The neutron could in theory be produced by the D-T reaction itself, suggesting that fusion power plants could include a breeding cycle, analogous to the breeding cycles possible for fission reactors [11].

The major engineering challenge for fusion power is to create and confine the reaction within a controlled environment while the plasma reaches temperatures exceeding 10^5 K. Several solutions have been proposed to cope with this challenge, and it has been agreed that confining plasma in a magnetic field is one of the most efficient ways. The theory of magnetic confinement was first proposed by Russian scientists in 1950s. TOKAMAK, which is an abbreviation of the magnetic confinement device in Russian, consists of a toroidal-shaped chamber with magnetic coils. It is widely used throughout the world [12]. A schematic view of the TOKAMAK design is shown in Figure 1.2.

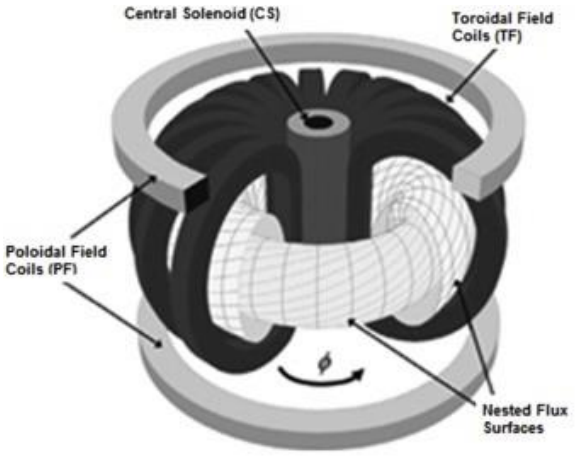

Figure 1.2 Schematic representation of the magnetic field system of a conventional Tokamak [13]

Superconducting magnets and electric currents surround the torus to create toroidal and poloidal magnetic fields that confine the plasma in a D-shaped torus. The currents flowing in poloidal coils create a toroidal field (TF) that spirals around the center. On the other hand, the currents flowing in toroidal coils create a poloidal field (PF) whose direction is vertical to the direction of TF, and that stabilizes the position of the flow in the plasma. Adding a poloidal magnetic field increases confinement time of the plasma substantially and helps to hold the plasma away from the torus walls. Another frequently applied alternative that helps to generate the poloidal field is to use poloidal magnets. The strength of the toroidal magnetic field is an order of magnitude more than the poloidal field's strength [14].

In addition to the challenges posed by particle confinement, the particles also need to be heated to overcome the Coulomb barrier and to increase the D-T fusion cross section. There are various methods to increase the temperature of ions and electrons. First, although electric current serves as a heater, in addition to creating a poloidal field, it is not possible to heat the plasma solely by electric current because the electrical resistance of the plasma decreases at elevated temperatures; thus, the plasma heating should be enhanced by different means. Projecting neutral deuterium atoms, which are immune to magnetic fields, into the plasma at higher velocities, also known as neutral beam injection, is one of the aforementioned methods. Radiofrequency heating is another method; this method uses radio waves at a specific frequency range that plasma is able to absorb. ITER will be using both of these technologies [15]. The desired operating condition for a fusion reaction is a point that there is no need for external heating, and this is usually called the ignition point.

At the ignition point, D-T reactions help plasma to sustain its heat to continue further chain reactions via emitted alpha particles [14].

1.3 Plasma Facing Materials

The cooling cycle, which will eventually be used for electricity generation, needs to operate at the highest temperatures possible for several reasons. First, power cycles are more efficient at higher turbine inlet temperatures. Whether for the Brayton or the Rankine cycle, increasing the temperature of the fluid entering the turbine will increase the area between the low and high pressure isobars in the T-s diagram, which represents the net work done by the cycle, and this will increase the thermal efficiency of the system. Second, operating at a higher ΔT lowers the pumping power for a system for a given coolant. Increasing the difference between inlet and outlet temperatures enables the system to run at lower mass flow rates, which is directly related to the pressure drop across the system. However, material properties in many cases also constrain the range of allowable temperatures. Tungsten (W), Beryllium (Be) and graphite (CFC) were believed to be the most suitable materials for the plasma-facing component in ITER and post-ITER studies. For example, the recrystallization temperature of W sets an upper temperature limit around 1300°C, while the ductile to brittle transition temperature (DBTT) of W sets a lower temperature limit of 600°C [16].

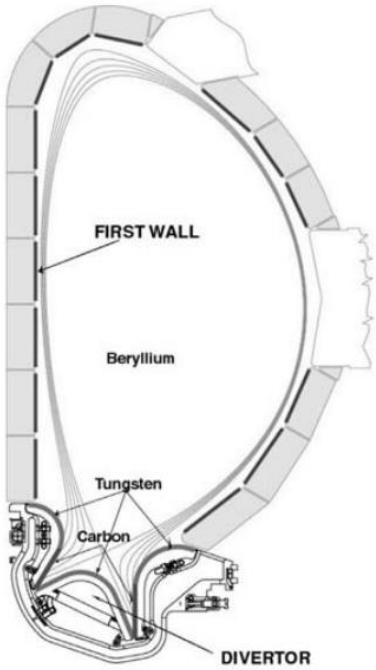

Figure 1.3 ITER cross-section showing the choice of materials for plasma facing components [17]

They have both some advantages and disadvantages [18]. In the current design, as a first wall material, Beryllium will be utilized in the main chamber. It has low atomic number (Z), high thermal conductivity and an ability to capture oxygen from plasma, which is important during the initialization. In addition, the low atomic number poses less contamination threat to the plasma. A high sputtering yield and low melting point are its weaknesses for dealing with more power.

The divertor is one of the most important parts of the inner chamber. It allows impurities caused by erosion of materials and fusion waste to be discharged from the system. As a high-Z material, tungsten has a low sputtering yield and high melting point,

which make it a good solution for the baffle zone and the top of the divertor. Graphite was considered to be put into use on the surfaces that are under the highest heat fluxes. Its nature makes graphite almost indestructible even in unexpectedly high and localized temperature spikes. However, the carbon accumulation concerns associated with graphite made the ITER designers abandon it. Transporting worn away material is complex; if carbon is used, it may end up at a point away from actual material and cause tritium absorption [17].

1.4 Linear Plasma Simulator and MPEX

Despite numerous theoretical studies and small-scale tests, no one can predict the actual response of materials in large-scale experiments. A large research and development effort is still underway to investigate the plasma-material interactions (PMI) in depth. The curved structure of the tokamak makes control of the radiation direction and its intensity challenging.

Linear plasma simulators are a convenient alternative way to study PMI issues. They provide better positioning for the material and better focus for the plasma, and they provide a more controlled exposure environment that is dedicated to the plasma modification of materials rather than confinement physics [19].

Other than general advantages of linear plasma devices over toroidal shaped ones, the MPEX design has some unique features over other linear plasma devices. First, instead of using an internal ion generating electrode, MPEX will be using radio frequency (RF) to eliminate any contamination within the system. Second, unlike most the linear plasma

devices, where heat flux from the plasma to the target plate is driven by convective heat transfer, MPEX, is similar to toroidal devices, in which heat transport is parallel to the magnetic field and is conduction driven. Finally, while other linear plasma devices use electro-static biasing or internal current between electrodes, MPEX will use high-power thermal plasma in front of the target, giving which provides a better comparison to a real fusion environment for realistic PMI studies [20].

As a part of multi-national consortium, US ITER is the domestic agency responsible for US contributions to ITER. On behalf of the Department of Energy, Oak Ridge National Laboratory (ORNL) hosts the ITER project office, along with many other partners around the country. One of the projects undertaken by ORNL is constructing a linear plasma simulator to develop and test materials along with capability of testing neutron irradiated materials. Thus, a prototype of the Material Plasma Exposure eXperiment (proto-MPEX) project has started to do PMI studies. It is anticipated that the findings of these experiments will make a significant contribution to material science, which is of paramount importance to ITER goals [21].

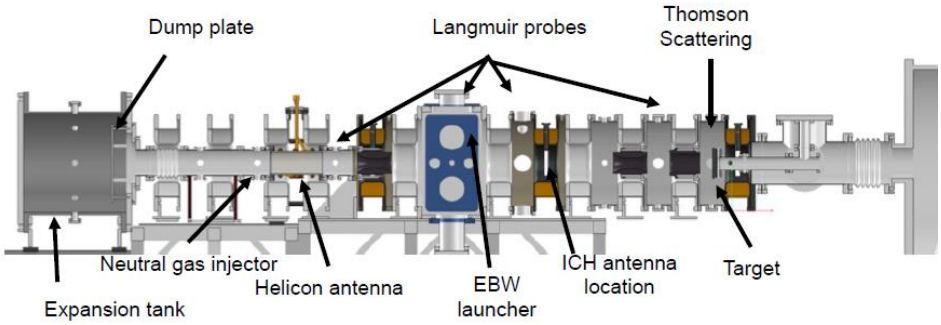

Figure 1.4 Schematic drawing of proto-MPEX [22]

The target plate, where much of the heat is transferred from the plasma, is a crucial element of the system. Proto-MPEX is restricted to operate at the order of seconds. In order to fill the gap between current material knowledge and planned usage of these materials in ITER, the system should be capable of operating at steady state. Most PMI targets will melt without active cooling. To achieve continuous operation, at least order of days, a new cooling system that is capable of handling an incident heat flux of the order of 10 MW/m^2 has to be implemented to the target station. Currently, proto-MPEX utilizes an RF helicon antenna, which is capable of delivering up to 120 kW heat at 13.56 MHz, a microwave heating around 30 kW power at 28 GHz, and an ion cyclotron heating around 30 kW at 7-9 MHz frequency. The plasma density in deuterium is higher than $6x10^{19}/m^3$ while the electron temperature reaches up to 10^5 K . The magnetic field on the axis is typically between 0.6 T and 1.4 T during operation [23]. For comparison, a typical Magnetic Resonance Imaging (MRI) whole-body system operates at 1.5 T [24].

Figure 1.5 Proto-MPEX Tungsten Target [25]

1.5 Objectives

As mentioned in previous sections, commercially available fusion power is a promising renewable energy source. However, there remain many challenges that must be overcome before fusion energy is commercially viable, including PMI. As part of the effort to understand and, in the long term, mitigate PMI, ORNL is designing a linear plasma simulator, MPEX, which will focus on changes in the properties of fusion-relevant materials when these materials are exposed to the ion fluxes typical of burning plasmas over long periods of time. These materials will also be exposed to very high steady-state heat fluxes ($q'' > 10 MW/m^2$) during these studies.

Cooling these materials, specifically target plates of these materials, will therefore require removing such high heat fluxes over several hours to days. Given that there are a number of gas-cooled divertor concepts that have been proposed to handle similar heat fluxes in the reactor chamber of MFE reactors, such gas-cooled divertor designs are a promising way to cool the target plates in the proposed MPEX facility. Therefore, this Master's Thesis aims to numerically evaluate and optimize a previously proposed helium-cooled divertor design, the T-tube, which will be discussed in the next Chapter, to cool the target plate of the linear plasma simulator MPEX, and to provide preliminary design parameters for future experimental studies. These numerical simulations use the commercially available computational fluid dynamics (CFD) software package ANSYS™ Fluent®.

CHAPTER 2. LITERATURE REVIEW

This chapter reviews gas-cooled divertor designs that are most applicable to the target plate of MPEX. Later, jet-impingement cooling is reviewed here since almost all divertor designs utilize some form of jet-impingement cooling. Finally, because the scope of this thesis is limited to numerical predictions; related CFD knowledge is presented.

2.1 Gas-Cooled Slot-Jet Divertors

As mentioned before, MPEX will be running at steady state, and its target plate, where the highest heat fluxes occur, will be subject to very high and most probably non-uniform heat fluxes at the order of 10 MW/m^2. The target plate cannot withstand that level of heat fluxes without active cooling; therefore, it needs to be cooled effectively. There are many different gas-cooled divertor designs that have been proposed for fusion reactors, and since the conditions in MPEX will be close to those fusion reactors, reviewing existing gas-cooled divertor concepts is a good starting point to find a cooling solution to the target plate of MPEX. In addition, MPEX basically is an experiment, the designers plan to have access to the back side of the target plate both physically and visually for experimental purposes.

Previously proposed divertor concepts use various type of cooling methods. These can be divided into three main categories based upon how they cool the target plates; slot jets, round jets and porous media. The advantages and the disadvantages of them, and their compatibility with the target plate of MPEX are discussed.

The T-tube concept shown in Figure 2.1, originally developed by the ARIES Compact Stellarator (CS) study, is an example of a divertor that relies on cooling by an impinging slot jet. The T-tube geometry consists of two concentric tubes with a 15 mm wide and 100 mm long slot on the top of the inner tube, opposite the inlet, which is in the center and bottom of the inner tube. Numerical simulations showed that the T-tube can extract a uniform heat flux up to $10\,MW/m^2$ without exceeding recrystallization temperature limits of WL10 Tungsten alloy (~1300 °C) for He entering at 600 °C and 10 MPa at a mass flow rate per slot length of 0.4 kg/(m·s) [6].

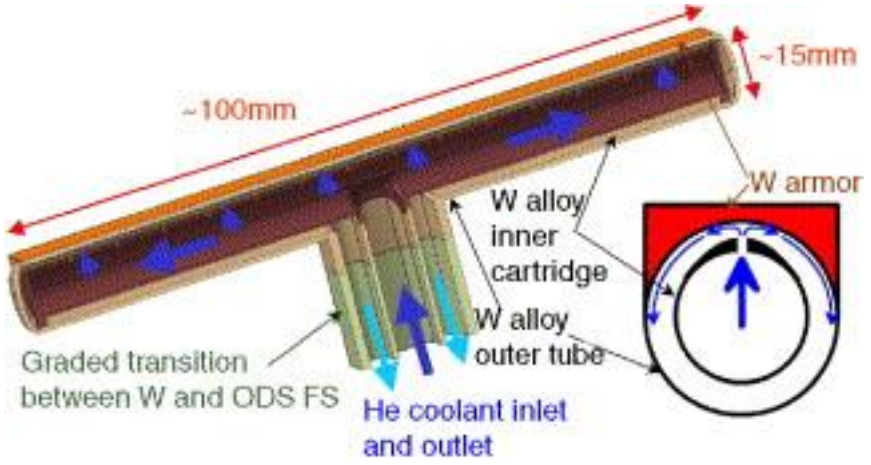

Figure 2.1 Cut off view of the T-tube concept showing the He flow configuration [6]

In this design, the helium, once it enters the inner tube, turns roughly 90° and flows along the cylinder axis before it is again turned ~90°, and exits through the slot as a 2D, or high aspect ratio rectangular jet. The jet then impinges on the inner surface of the outer tube 1.25 mm away, cooling the outer tube and the W armor tile brazed to the top of the

outer tube. The heated He then flows along the annular gap between the inner and outer tubes, exiting the T-tube at the bottom.

While the relatively larger surface area (~15 cm^2) of armor tile makes it a good candidate for the MPEX target plate cooling system, the requirement of a manifold at the bottom of the divertor necessitates an abundance of free space at the back of the target plate, which is not possible in the current MPEX design, and which prevents measurements by Infrared (IR) cameras for diagnostic purposes.

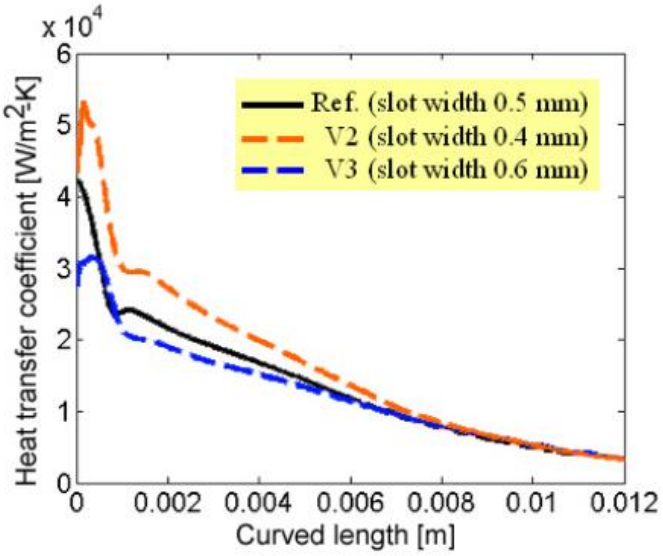

Figure 2.2 . Heat transfer coefficient vs. position along the inner surface of the outer tube measured from the slot (2D FLUENT® simulations) [16]

Previous 2D simulations of a cross-section of the T-tube suggest that the design is "robust" in that varying the slot width from 0.4 mm to 0.6 mm, *vs.* the nominal value of 0.5 mm, has little effect upon HTC (Figure 2.2), suggesting that the thermal performance of this design will not be affected significantly by machining variations or thermal expansion [16].

These numerical simulations of the T-tube were validated by experimental data, albeit using air at near-ambient conditions as the coolant. The experimental studies of the T-tube by Crosatti (Figure 2.3) used an axisymmetric test section with geometric dimensions that closely mimicked those of the T-tube, but the test section was subject to a uniform axisymmetric heat flux using electric resistance heating, *vs.* the one-sided heat flux in the actual T-tube concept. Moreover, the coolant (air) entered the test section at the end, *vs.* the center, of the inner tube, and flowed along to, *vs.* normal to, the tube axis.

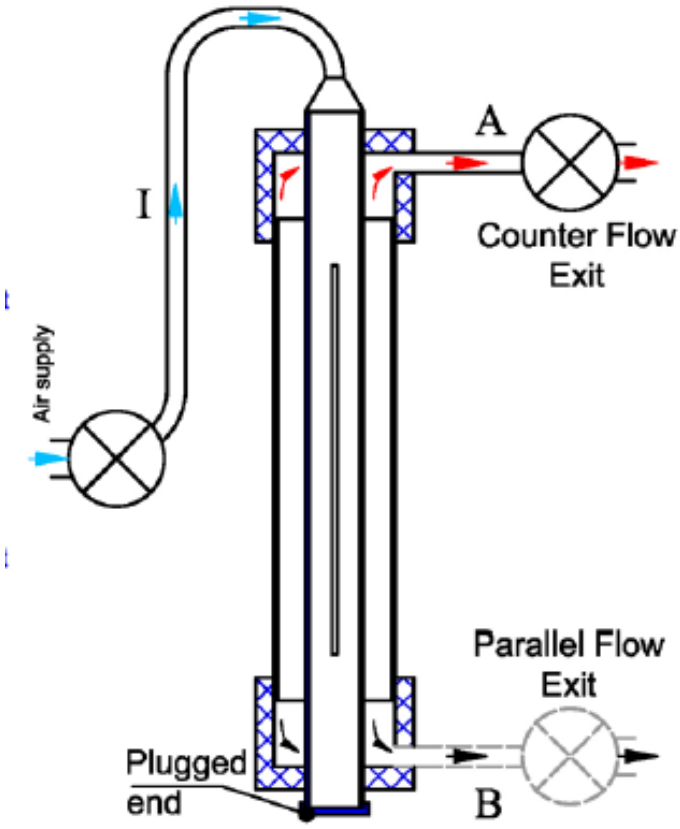

Figure 2.3 Schematic of Crosatti's experimental flow loop for counter and parallel flow configurations [26]

This modified T-tube design is actually better suited for MPEX than the original T-tube because it requires access only from the ends of the target holder, thereby maximizing the area on the backside of the target plate available for diagnostics and for monitoring instrumentation. In MPEX, however, the target will be subject to one-sided heating, as is the case in the original T-tube design.

Crosatti investigated three different flow configurations in his T-tube test section, of which only two, counter-flow and parallel flow (Figure 2.4) are reviewed here. The third, double inlet, flow configuration is not relevant to the work described here.

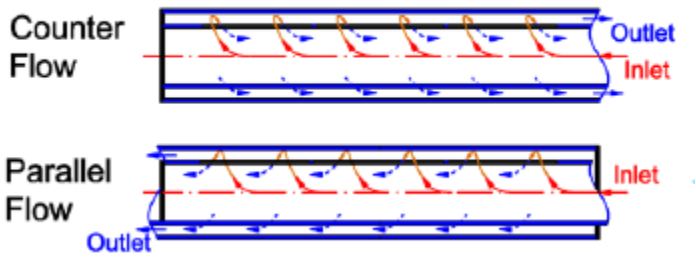

Figure 2.4 Sketch of the flows in the counter-flow and parallel flow cases [26]

In the counter-flow configuration, the inlet and outlet are at the same end of the test section. This configuration minimizes the flow path length and leads to very low velocities, and hence nearly stagnant flow, at the plugged end opposite the inlet and outlet, which causes significant variations in temperature and HTC along the tube axis. These variations increase with the length of the tube.

In the parallel flow configuration, the inlet and outlet are at opposite ends of the test section. This configuration, by forcing the fluid to traverse the entire axial extent of the T-tube, gives a more uniform temperature and HTC distribution compared with the counter-flow configuration for otherwise identical conditions.

Table 2 Comparison of Thermal Performance of Different Flow Configurations [26]

Configuration	h_{max} [W/m^2·K]	axial Δh [W/m^2·K (%)]	Performance
Double Inlet	2,168	1,066 (49.2)	Best
Parallel Flow	2,613	1,630 (62.4)	Intermediate
Counter Flow	3,345	2,683 (80.2)	Worst

Table 2 assesses the thermal performances of the three flow configurations based on their maximum differences in axial HTC. The counter-flow case has the worst performance, followed by the parallel flow, then the double inlet, configurations. Although beyond the scope of this thesis, the double inlet configuration has the best performance because it effectively reduces to two counter-flow configurations, each occupying half the axial length of the tube, which in turn leads to a much more uniform temperature and HTC along the length of the T-tube test section.

Arrays of impinging round jets are also frequently used to cool divertor target surfaces. The helium-cooled multi-jet (HEMJ) divertor, illustrated in Figure 2.5, is perhaps the best-known example of this type of divertor. A single HEMJ “finger” utilizes a hexagonal array of 25 round jets exiting from a curved surface, and impinging upon and cooling a concave curved surface about 0.9 mm away from the jet exits. Researchers at the

Karlsruhe Institute of Technology (KIT) in Karlsruhe, Germany proposed this specific design, which is rated for 10 MW/m^2 for He inlet conditions of 600 °C and 10 MPa [26]. This design has the highest experimentally tested HTC to date; however, the relatively small area (< 2 cm^2) cooled by a single HEMJ "finger" requires an efficient manifolding at the bottom to supply equal amounts of helium to each finger and enough free space to accommodate the whole assembly on the back side of the target plate. These requirements make it impractical for the current MPEX design.

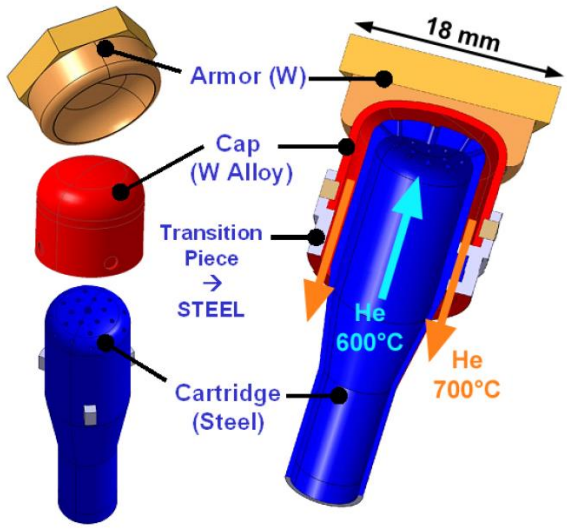

Figure 2.5 Schematic of the FZK HEMJ divertor finger module

Although it does not uses impinging-jets, porous material filled concepts are also studied for divertor designs. In the concepts based on porous media, the coolant flows through a porous medium, such as a foam usually made of a refractory metal, which is in direct contact with the heated surface. The porous media concepts can extract more heat because of their increased surface area and enhanced turbulent mixing because the porous medium obstructs and diverts the flow of coolant, much like flow baffles in heat exchangers [27]. On the other hand, heat transfer dynamics of porous media makes such approaches

prone to show flow mal-distribution in large scale (at the same order of magnitude with the whole flow domain) under non-uniformly heated circumstances, for example, locally heated foam-filled small channel tee-tube design [28]. Since the heat transfer occurs not only on a single impingement surface but also all the way down to the discharge point of the helium from the media, under non-uniform heating cases, gas may run away from the heated side because of increased pressure drop and a drop in local density at that particular section. This causes localized hot spots on the surface and may result in melting of the material. In their research, Youchison and Nygren have found that mal-distribution of Helium in a porous refractory material channel can be up to 32% for the hot leg of the channel in some extreme cases [28]. A higher pressure drop in porous media is another disadvantage that requires significantly higher pumping power.

As a result of literature review on previous gas cooled divertor designs, the T-tube design was found as the best match for MPEX because of its geometrical compatibility with the target plate of MPEX, heat flux handling capability and robustness. Therefore, the t-tube was selected to be analyzed further numerically as a candidate concept for the target plate cooling system of MPEX.

2.2 Jet Impingement Cooling

Most of the divertor designs in the literature depend on jet-impingement cooling to deal with very high heat fluxes incident on the first wall of the fusion reactor chamber. First, we define an impinging jet, and then various type of jet configurations are presented and discussed. Later, their advantages in heat transfer over wall-bounded flows are discussed and most common applications with impingement jets are mentioned. In the final

part, the effects of dimensionless numbers that are used for thermal performance characterization of impinging jets are summarized.

An impinging jet can be described as a jet, *i.e.*, a flow accelerated through, and exiting from, a contraction or nozzle that impinges upon a solid target surface. Nozzles with a round or rectangular cross-section are the most commonly used contraction geometries. A schematic of an impinging jet is given in Figure 2.6.

Although there are many types of impinging jets (Figure 2.7), the two most common types are submerged (c), and free-surface (a), jets. A submerged jet, such as a liquid-into-liquid, or gas-into-gas jet, is a jet where the jet fluid density is comparable to that of the surrounding fluid. A free-surface jet is in most cases a jet of liquid that issues into gaseous surroundings. This thesis focuses on confined gas-into-gas impinging jets, as detailed later on in this section.

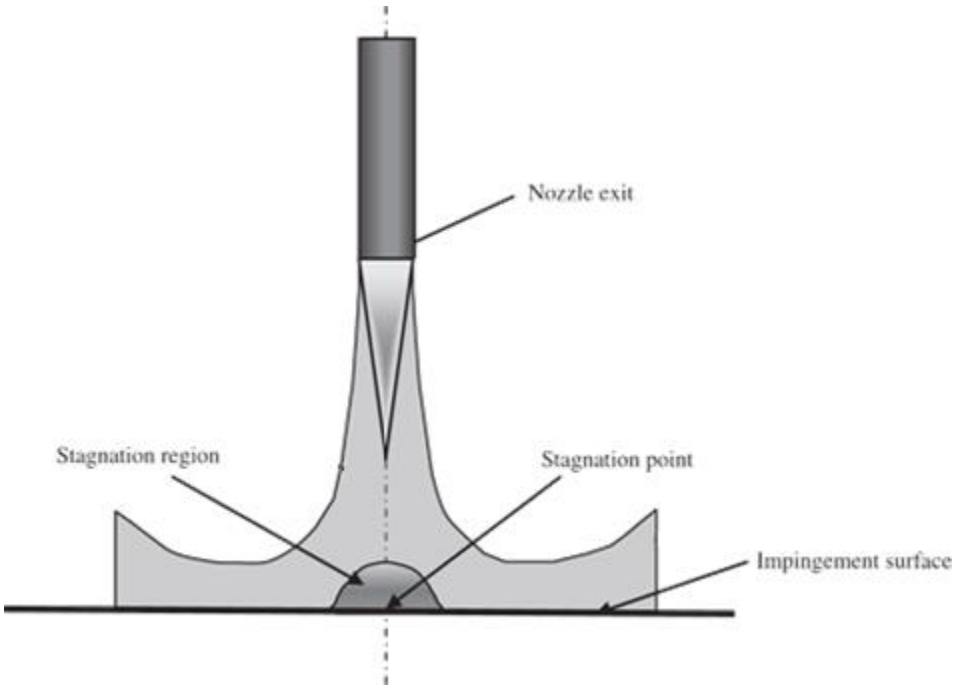

Figure 2.6 Sketch of an impinging jet [29]

Impinging jets are often used in applications that require high heat removal rates because they have extremely high heat transfer coefficients (HTC). The main advantage of jet impingement in heat transfer is due to its relatively thin thermal boundary layer. When the jet hits the target surface, it quickly decelerates and changes its direction; as a result, it forms a very thin stagnation-zone momentum boundary layer, and consequently thermal boundary layer ($Pr \cong 1$), which minimizes thermal resistance and hence significantly enhances the heat transfer [30]. In jet impingement, heat transfer rates can be as great as three times that for a wall-bounded flow at a given velocity. To achieve comparable HTC in a flow over and parallel to a flat plate, the device size would be two orders of magnitude larger than a comparable impinging-jet cooling system [31].

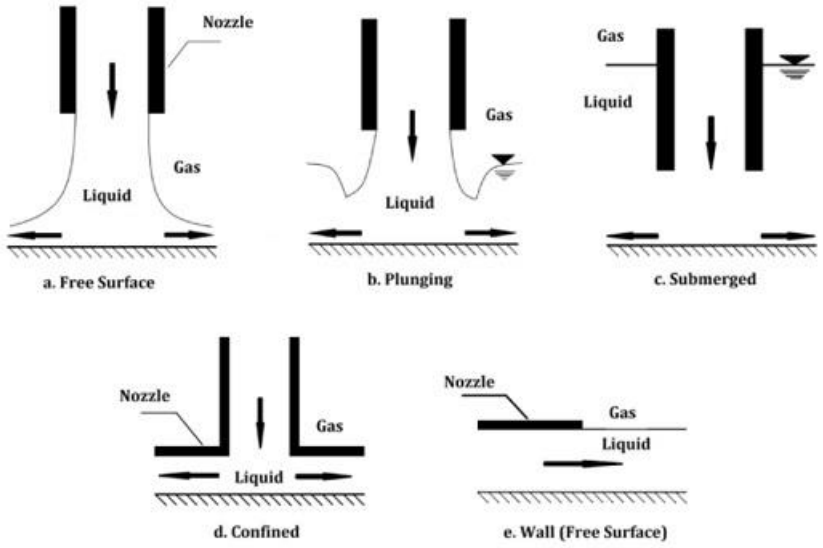

Figure 2.7 Different types of impinging jets

To assess and improve the thermal performance of a divertor that uses impinging jets, factors that affect heat transfer in an impinging jet are summarized and presented below. All factors are basically dimensionless numbers that characterize heat transfer in an impinging jet.

The heat transfer rate in an impinging jet is affected by a variety of parameters, the most important of which are the non-dimensional heat transfer coefficient or Nusselt number (*Nu*), the non-dimensional jet mass flow rate or Reynolds number (*Re*), the ratio of momentum diffusivity to thermal diffusivity or the Prandtl number (*Pr*), the dimensionless distance between the jet nozzle exit and the plate in nozzle exit diameters (H/D_h) and the dimensionless distance on the cooled surface from the stagnation point in nozzle exit diameters (x/D_h) [32]. The hydraulic diameter D_h is the nozzle exit diameter for circular jets and twice the nozzle width, $2W$, for rectangular jets of high aspect ratios

(W <<length L), which are known as slot jets. The characteristic velocity is the average velocity of the fluid, $\bar{V}$, at the nozzle exit. So the Reynolds number for a slot jet is

$$\boldsymbol{Re} = \frac{\boldsymbol{\rho D_h \bar{V}}}{\boldsymbol{\mu}} = \frac{\boldsymbol{D_h \dot{m}}}{\boldsymbol{A_{slot} \mu}} \quad \textbf{(2)}$$

where μ is the dynamic, or absolute, viscosity, and ρ the density, of the jet fluid at the nozzle exit, and $A_{slot} = LW$ is the cross-sectional area of the slot.

The area-averaged Nusselt number, $\overline{Nu}$, is given as a function of *Re* and *Pr* from dimensional analysis:

$$\overline{\boldsymbol{Nu}} = \boldsymbol{f(Re, Pr)} \quad \textbf{(3)}$$

where

$$\overline{\boldsymbol{Nu}} = \frac{\bar{\boldsymbol{h}} \boldsymbol{D_h}}{\boldsymbol{k}} \quad \textbf{and} \quad \boldsymbol{Pr} = \frac{\nu}{\alpha} \quad \textbf{(4)}$$

Here, ν is the kinematic viscosity, α is the thermal diffusivity and k is the thermal conductivity of the fluid.

The area-averaged heat transfer coefficient (HTC) is:

$$\bar{\boldsymbol{h}} = \frac{\overline{\boldsymbol{q''}}}{\overline{\boldsymbol{T_c}} - \boldsymbol{T_e}} \quad \textbf{(5)}$$

where $\overline{q''}$ is the area-average heat flux through the surface, $\bar{T}_c$ is the average surface temperature and T_e is the fluid temperature at the nozzle.

The local Nusselt number is given as:

$$\boldsymbol{Nu = \frac{hD_h}{k}} \quad \textbf{(6)}$$

where *h* is the local heat transfer coefficient instead area-averaged value.

Although most impinging-jet cooling studies have a jet impinging upon a flat surface, the T-tube design involves a slot jet that impinges on a curved, specifically concave, surface. Considering the different types of impinging jets shown in Figure 2.7, the T-tube is most similar to a confined impinging jet. A confined impinging jet is an impinging jet where the flow downstream of the stagnation region is confined by a surface, usually a nozzle plate, from the top. Although there is no definitive consensus on the "critical" value of H/D_h, defining when an impinging jet is considered confined, Gao and Ewing found that confinement had no effect on HTC for $H/D_h > 6$ [33]. On the other hand, Zuckerman and Lior reported that for $H/D_h > 12$, the confinement surface does not interfere with the flow [31]. Given that the T-tube has a much lower H/D_h of about unity, the impinging jet in this design is clearly a confined impinging jet.

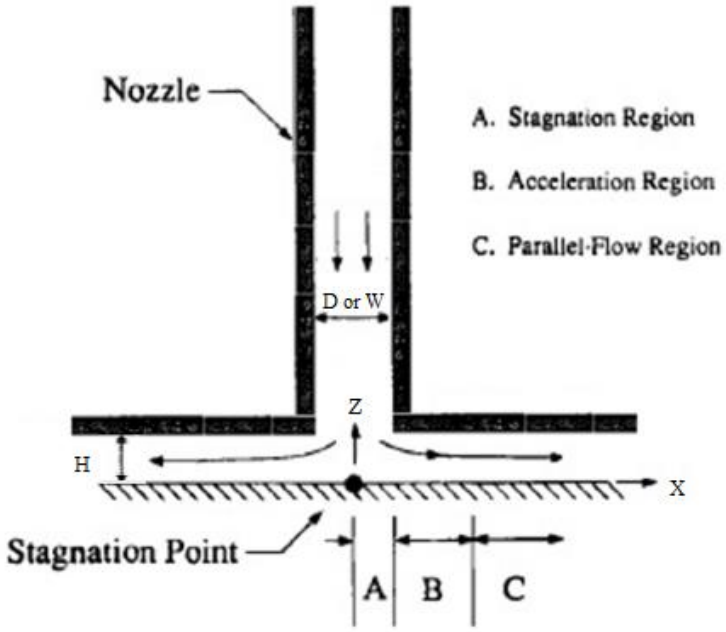

Figure 2.8 Flow regions of a confined jet [34]

Knowing the hydrodynamics of a confined jet helps to understand heat transfer phenomenon in a divertor design that uses jet impingement. In addition, it is essential to have a grasp about heat transfer mechanism in an impinging jet to make systematic improvements to the thermal performance of a divertor. Flow regions and their definitions of a confined jet are given below.

In Figure 2.8, which shows a confined impinging jet, the pressure reaches its peak maximum value at the stagnation point on the impingement surface. The stagnation region (A) is defined to be the region where $x/W < 0.5$ in the vicinity of the stagnation point. Beyond the stagnation region, the flow velocity increases in the acceleration region (B), reaching the average surface jet velocity by $x/W = 2$. Beyond the acceleration region ($x/W > 2$), the effect of jet impingement is negligible in the parallel-flow region (C) [34].

For cases with small nozzle-to-surface spacing (H/D_h < 1 [35]), the average jet velocity at the exit of the nozzle is almost that at the impingement surface. However, for H/D_h > 1, the jet velocity just before the impingement surface can be greater or less than the nozzle exit velocity, depending on whether the jet is a vertical jet, and accelerated or decelerated by gravity. In this case, surface velocity is calculated from the balance of energy [34].

Since the effect of impingement on heat transfer degrades quickly beyond two slot width of the stagnation point for slot jets, selection of the slot width becomes important for a given lateral distance. This needs to be taken into consideration for divertor designs.

Because the dimensionless distance between nozzle exit and the target surface is a factor in thermal performance of jet cooling, the studies investigate effects of nozzle-to-plate distance of both round and slot jets are summarized, and based on their results, the choice of H/D_h for the model is decided.

Many studies have tried to identify the optimum value for the spacing between the jet exit and the surface in nozzle exit diameters in terms of maximizing HTC. The results depend upon the type of impinging jet, such as the specific jet configuration (*e.g.* open or confined, single or multiple impinging jets), and whether the jet is circular or rectangular. Harnett et al. reported that H should be between 5 and 8 nozzle dimensions for a given set of average nozzle and surface jet velocities [34]. In another study, in which air is used as fluid, San and Shiao found that the Nusselt number at the stagnation point decreases with increasing H/d (for $2< H/d <6$) for a circular jet, where d is the diameter of the nozzle

[36]. Stevens and Webb have reported that H/d has very limited effect on the stagnation Nusselt number for a circular jet of water with $Nu \propto (H/d)^{-0.032}$ for $1.7 < H/d < 34$ [37].

Zhou and Lee conducted one of the most comprehensive studies of impinging slot jets of air to assess how HTC depends upon nozzle-to-surface spacing and x/B, where B is the slot width and x is the lateral distance from the stagnation point. Their results are given in Figure 2.9. While the highest stagnation Nusselt number is obtained at $Z/B = 6$, where Z is the distance from nozzle exit to plate , the smallest variation of Nusselt number along the x-direction, which is desirable because it minimizes the thermal stresses, occurs at $Z/B = 1$ [38].

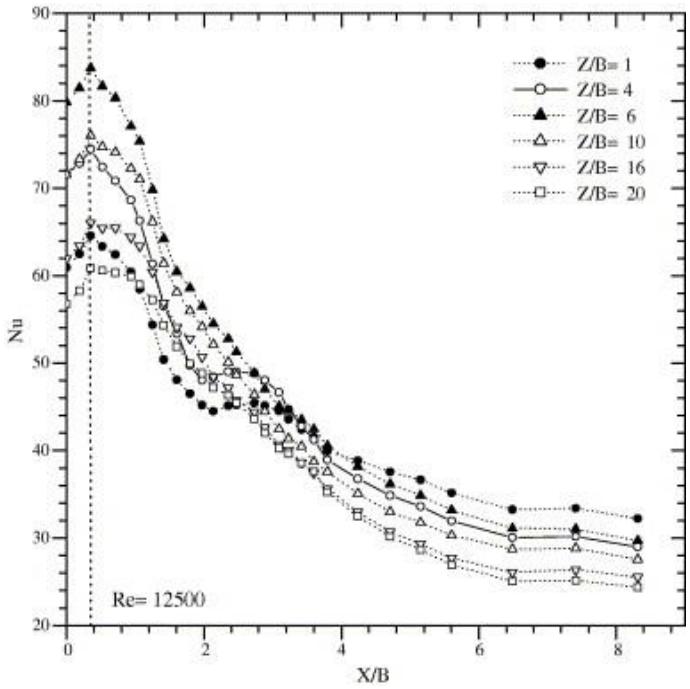

Figure 2.9 Lateral variation in local Nusselt number at Re = 12,500 [38]

Zukowski studied thermal performance of confined single slot jet of air impinging on a flat surface at four different Reynolds numbers (500, 1000, 1500 and 2000) with four different *H/B* ratios (4, 6, 8 and 10). The highest stagnation point Nusselt numbers were obtained with *H/B* = 6 and the minimum lateral variation was with *H/B* = 4 [39].

In their research, Lee et al. investigated the thermal performance of confined slot jets impinging on a concave surface. They tested three different Reynolds numbers (200, 400 and 600) and three different nozzle-to-plate spacing *H/B* (2, 6, and 10). The highest stagnation Nusselt number occurred with *H/B*=2 and the minimum lateral variation with *H/B*=10 [40]

Based on the studies summarized above, the optimum value of nozzle-to-plate spacing for the highest stagnation Nusselt number and for the minimum lateral variation is different for round and slot jets. There is no an exact consensus on the optimum value of the nozzle-to-plate distance for the highest Nusselt number or the minimum lateral variation of the Nusselt number. Therefore, based on the recommendations made by previous researchers who worked on designs similar to the T-tube [6, 26], *H/W*=2 is used for the simulations.

In impinging jets, heat transfer coefficient is directly related to the Nusselt number, and the Nusselt number is a function of the Reynolds number along with the Prandtl number (Eq. 3). However, this relation is an empirical correlation, and it depends on various factors such as jet configuration (*i.e.*, round or rectangular), and the Reynolds number range (*i.e.*, laminar or turbulent). Therefore, some of the correlations found for impinging jets are summarized below. Although the Prandtl number also has an effect on

the Nusselt number, it is not included in literature review due to being a material property rather than flow feature, and only Helium is used as working fluid in the simulations.

The Nusselt number depends strongly on the Reynolds number, and although there are various correlations for $Nu(Re)$ over different ranges of Re, almost all of these correlations assume a power-law relation of the type $Nu \propto Re^{n}$, where $n < 1$. Gordon and Akfirat found the following correlation for multiple slot air-jets in their study [41].

$$\boldsymbol{Nu = 0.36\, Re^{0.62} \quad \text{for } Re > 2000 \ \ and \ \frac{z_n}{B} > 8} \tag{7}$$

where the Reynolds number is based on slot width:

$$\boldsymbol{Re = \frac{D_h \dot{m}}{A_{slot} \mu}} \tag{8}$$

Lee et al. studied the heat transfer performance of an array of circular air jets as a function of the dimensionless distance from stagnation point x/D and Re. Their results, shown in Figure 2.10, also suggest a power-law relationship between Re and Nu [42].

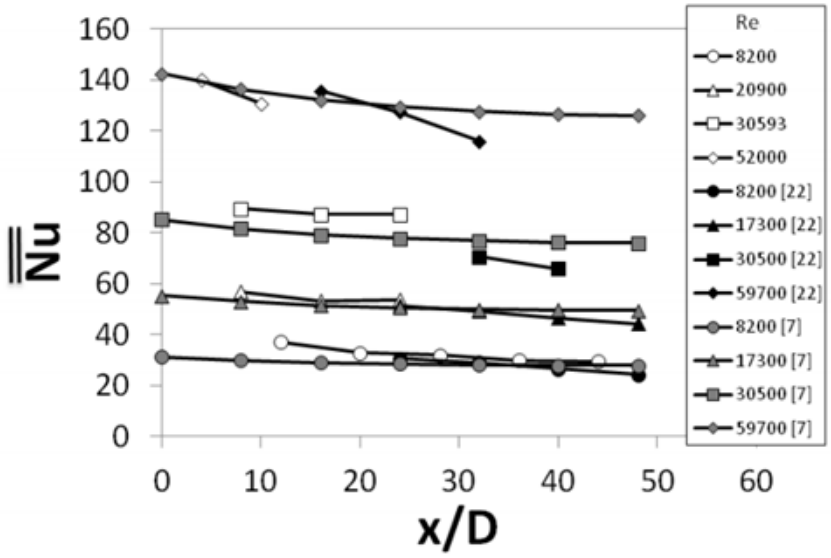

Figure 2.10 Spatially-averaged Nusselt numbers as a function of *x*/*D* for different values of Re [42]

Based on these results of the studies that investigate the effects of the Reynolds number on the Nusselt number, increasing the mass flow rate (also *Re*) does not benefit the heat transfer coefficient in an impinging jet at the same rate whether it is a round or a slot jet. Therefore, these power-law relations (power less than 1) needs to be taken into account while considering possible mass flow rates.

2.3 Numerical Models

The extremely high heat fluxes, temperatures, and pressures typical of fusion make obtaining experimental data at prototypical conditions both challenging and costly. Very few previous experimental studies have been performed at prototypical conditions,

however. Many of the experimental studies rely instead on dynamic similarity because of limited resources, and numerical models are usually validated with experimental data at more achievable conditions to simulate prototypical conditions. There are many options to simulate flow problems with different level of accuracy in exchange with computation time.

At present, direct numerical simulations (DNS) are the most accurate way to conduct simulations; however, they still remain impractical for high Reynolds number flows through complex geometries, as is the case for helium-cooled divertors. Hence, turbulence models are required to solve the governing equations, and selection of the turbulence model becomes an important issue for obtaining accurate numerical predictions. Although numerous turbulence models have been developed, only the models that are available in the commercial CFD software package ANSYS™ Fluent®, namely the k-ε turbulence models and the Spalart-Allmaras model, will be discussed here.

Although turbulent flow is predictable in terms of its mean quantities (averaged over time), the marked fluctuations typical of turbulence make it impossible to predict instantaneous quantities [43]. The mean turbulent flow properties can be determined from the Reynolds-averaged Navier-Stokes (RANS) equations. In Reynolds averaging, the instantaneous flow parameters are decomposed into a time average, or mean, and fluctuation around the mean. For the velocity, decomposition is as follows

$$\boldsymbol{u = \bar{u} + u'} \tag{9}$$

$\bar{u}$ = time-averaged velocity, u'= fluctuation around the mean

The RANS equations are obtained by re-writing the flow properties in this form in the Continuity and Navier-Stokes equations, and taking a time average of these four equations. In Cartesian coordinates, the resulting equations are:

$$\frac{\partial \rho}{\partial t} + \frac{\partial (\rho \bar{u})}{\partial x} + \frac{\partial (\rho \bar{v})}{\partial y} + \frac{\partial (\rho \bar{w})}{\partial z} = 0 \quad (10)$$

$$\frac{\partial}{\partial t}(\rho \bar{u}) + \frac{\partial}{\partial x}(\rho \bar{u}^2) + \frac{\partial}{\partial y}(\rho \bar{u}\bar{v}) + \frac{\partial}{\partial z}(\rho \bar{u}\bar{w}) = -\frac{\partial \bar{p}}{\partial x} + \left[\frac{\partial}{\partial x}(\mu \frac{\partial \bar{u}}{\partial x} - \rho \overline{u'^2} + \frac{\partial}{\partial y}(\mu \frac{\partial \bar{u}}{\partial y} - \rho \overline{u'v'}) + \frac{\partial}{\partial y}(\mu \frac{\partial \bar{u}}{\partial z} - \rho \overline{u'w'})\right] \quad (11)$$

$$\frac{\partial}{\partial t}(\rho \bar{v}) + \frac{\partial}{\partial x}(\rho \bar{v}\bar{u}) + \frac{\partial}{\partial y}(\rho \bar{v}^2) + \frac{\partial}{\partial z}(\rho \bar{v}\bar{w}) = -\frac{\partial \bar{p}}{\partial y} + \left[\frac{\partial}{\partial x}(\mu \frac{\partial \bar{v}}{\partial x} - \rho \overline{v'u'} + \frac{\partial}{\partial y}(\mu \frac{\partial \bar{v}}{\partial y} - \rho \overline{v'^2}) + \frac{\partial}{\partial y}(\mu \frac{\partial \bar{v}}{\partial z} - \rho \overline{v'w'})\right] \quad (12)$$

$$\frac{\partial}{\partial t}(\rho \bar{w}) + \frac{\partial}{\partial x}(\rho \bar{w}\bar{u}) + \frac{\partial}{\partial y}(\rho \bar{w}\bar{v}) + \frac{\partial}{\partial z}(\rho \bar{w}^2) = -\frac{\partial \bar{p}}{\partial z} + \left[\frac{\partial}{\partial x}(\mu \frac{\partial \bar{w}}{\partial x} - \rho \overline{w'u'} + \frac{\partial}{\partial y}(\mu \frac{\partial \bar{w}}{\partial y} - \rho \overline{w'v'}) + \frac{\partial}{\partial y}(\mu \frac{\partial \bar{w}}{\partial z} - \rho \overline{w'^2})\right] \quad (13)$$

These four equations involve ten unknowns (*vs.* four for the original Continuity and Navier-Stokes equations), namely the mean density, the three mean components of velocity, and the six independent components of the (symmetric) second-order Reynolds stress tensor. There are therefore six more unknowns than equations, which makes it impossible to solve the problem without six additional relations, which is commonly known as the turbulence closure problem.

The Boussinesq approximation, which is used both in Spalart-Allmaras and k-ε models, rewrites the Reynolds stresses in terms of an eddy viscosity, μ_t, the strain-rate

tensor, which is a function of the velocity gradients, and the turbulent kinetic energy, k [44]

$$\begin{bmatrix} \rho\overline{u'^2} & \rho\overline{u'v'} & \rho\overline{u'w'} \\ \rho\overline{v'u'} & \rho\overline{v'^2} & \rho\overline{v'w'} \\ \rho\overline{w'u'} & \rho\overline{v'w'} & \rho\overline{w'^2} \end{bmatrix} = -\mu_t \begin{bmatrix} \frac{\partial u}{\partial x}+\frac{\partial u}{\partial x} & \frac{\partial u}{\partial y}+\frac{\partial v}{\partial x} & \frac{\partial u}{\partial z}+\frac{\partial w}{\partial x} \\ \frac{\partial u}{\partial y}+\frac{\partial v}{\partial x} & \frac{\partial v}{\partial y}+\frac{\partial v}{\partial y} & \frac{\partial v}{\partial z}+\frac{\partial w}{\partial y} \\ \frac{\partial u}{\partial z}+\frac{\partial w}{\partial x} & \frac{\partial v}{\partial z}+\frac{\partial w}{\partial y} & \frac{\partial w}{\partial z}+\frac{\partial w}{\partial z} \end{bmatrix} + \frac{1}{3}\begin{bmatrix} \rho\overline{u'^2}+\rho\overline{v'^2}+\rho\overline{w'^2} & 0 & 0 \\ 0 & \rho\overline{u'^2}+\rho\overline{v'^2}+\rho\overline{w'^2} & 0 \\ 0 & 0 & \rho\overline{u'^2}+\rho\overline{v'^2}+\rho\overline{w'^2} \end{bmatrix} + \frac{2}{3}\mu_t\begin{bmatrix} \frac{\partial u}{\partial x}+\frac{\partial v}{\partial y}+\frac{\partial w}{\partial z} & 0 & 0 \\ 0 & \frac{\partial u}{\partial x}+\frac{\partial v}{\partial y}+\frac{\partial w}{\partial z} & 0 \\ 0 & 0 & \frac{\partial u}{\partial x}+\frac{\partial v}{\partial y}+\frac{\partial w}{\partial z} \end{bmatrix} \quad \textbf{(14)}$$

where the turbulent kinetic energy $k = \frac{1}{2}\,(\overline{u'^2}+\overline{v'^2}+\overline{w'^2})$

If the flow is incompressible, the last term cancels out, and the equation becomes:

$$\begin{bmatrix} \rho\overline{u'^2} & \rho\overline{u'v'} & \rho\overline{u'w'} \\ \rho\overline{v'u'} & \rho\overline{v'^2} & \rho\overline{v'w'} \\ \rho\overline{w'u'} & \rho\overline{v'w'} & \rho\overline{w'^2} \end{bmatrix} = -\mu_t \begin{bmatrix} 2\frac{\partial u}{\partial x} & \frac{\partial u}{\partial y}+\frac{\partial v}{\partial x} & \frac{\partial u}{\partial z}+\frac{\partial w}{\partial x} \\ \frac{\partial u}{\partial y}+\frac{\partial v}{\partial x} & 2\frac{\partial v}{\partial y} & \frac{\partial v}{\partial z}+\frac{\partial w}{\partial y} \\ \frac{\partial u}{\partial z}+\frac{\partial w}{\partial x} & \frac{\partial v}{\partial z}+\frac{\partial w}{\partial y} & 2\frac{\partial w}{\partial z} \end{bmatrix} + \frac{2}{3}\begin{bmatrix} \rho k & 0 & 0 \\ 0 & \rho\mathrm{k} & 0 \\ 0 & 0 & \rho\mathrm{k} \end{bmatrix} \quad \textbf{(15)}$$

By assuming that μ_t is a scalar (*vs.* a higher-order tensor), the Boussinesq assumption reduces the number of unknowns to two (*vs.* six). In contrast, the Reynolds stress model solves for all six unknowns instead of using the Boussinesq approximation, albeit at the cost of significant additional computational time [45].

In the Spalart-Allmaras (SA) model, the second and third term on the right-hand side of Eq. 14 are assumed to be negligible for thin shear flows [46]. The model introduces one additional transport equation for the turbulent eddy viscosity $v_t = \mu_t/\rho$:

$\tilde{v}$ is the transported variable in the Spalart-Allmaras model, and it is identical to the turbulent kinematic viscosity except in the viscosity-affected near-wall region.

$$\frac{\partial}{\partial t}(\rho\tilde{v}) + \frac{\partial}{\partial x}(\rho\tilde{v}u) = G_v + \frac{1}{\sigma_{\tilde{v}}}\left[\frac{\partial}{\partial x}\left\{(\mu + \rho\tilde{v})\frac{\partial\tilde{v}}{\partial x}\right\} + C_{b2}\rho\left(\frac{\partial\tilde{v}}{\partial x}\right)^2\right] + \frac{1}{\sigma_{\tilde{v}}}\left[\frac{\partial}{\partial y}\left\{(\mu + \rho\tilde{v})\frac{\partial\tilde{v}}{\partial y}\right\} + C_{b2}\rho\left(\frac{\partial\tilde{v}}{\partial y}\right)^2\right] + \frac{1}{\sigma_{\tilde{v}}}\left[\frac{\partial}{\partial z}\left\{(\mu + \rho\tilde{v})\frac{\partial\tilde{v}}{\partial z}\right\} + C_{b2}\rho\left(\frac{\partial\tilde{v}}{\partial z}\right)^2\right] - Y_v + S_{\tilde{v}} \quad (16)$$

$$\frac{\partial}{\partial t}(\rho\tilde{v}) + \frac{\partial}{\partial y}(\rho\tilde{v}v) = G_v + \frac{1}{\sigma_{\tilde{v}}}\left[\frac{\partial}{\partial x}\left\{(\mu + \rho\tilde{v})\frac{\partial\tilde{v}}{\partial x}\right\} + C_{b2}\rho\left(\frac{\partial\tilde{v}}{\partial x}\right)^2\right] + \frac{1}{\sigma_{\tilde{v}}}\left[\frac{\partial}{\partial y}\left\{(\mu + \rho\tilde{v})\frac{\partial\tilde{v}}{\partial y}\right\} + C_{b2}\rho\left(\frac{\partial\tilde{v}}{\partial y}\right)^2\right] + \frac{1}{\sigma_{\tilde{v}}}\left[\frac{\partial}{\partial z}\left\{(\mu + \rho\tilde{v})\frac{\partial\tilde{v}}{\partial z}\right\} + C_{b2}\rho\left(\frac{\partial\tilde{v}}{\partial z}\right)^2\right] - Y_v + S_{\tilde{v}} \quad (17)$$

$$\frac{\partial}{\partial t}(\rho\tilde{v}) + \frac{\partial}{\partial z}(\rho\tilde{v}w) = G_v + \frac{1}{\sigma_{\tilde{v}}}\left[\frac{\partial}{\partial x}\left\{(\mu + \rho\tilde{v})\frac{\partial\tilde{v}}{\partial x}\right\} + C_{b2}\rho\left(\frac{\partial\tilde{v}}{\partial x}\right)^2\right] + \frac{1}{\sigma_{\tilde{v}}}\left[\frac{\partial}{\partial y}\left\{(\mu + \rho\tilde{v})\frac{\partial\tilde{v}}{\partial y}\right\} + C_{b2}\rho\left(\frac{\partial\tilde{v}}{\partial y}\right)^2\right] + \frac{1}{\sigma_{\tilde{v}}}\left[\frac{\partial}{\partial z}\left\{(\mu + \rho\tilde{v})\frac{\partial\tilde{v}}{\partial z}\right\} + C_{b2}\rho\left(\frac{\partial\tilde{v}}{\partial z}\right)^2\right] - Y_v + S_{\tilde{v}} \quad (18)$$

G_v: Production of the turbulent viscosity

Y_v: Destruction of the turbulent viscosity

$S_{\tilde{v}}$: Source term

C_{b2} and $\sigma_{\tilde{v}}$ are constants

There are twelve unknown constants in the SA model that are estimated from experimental data. The transported variable $\tilde{v}$ can be related to the turbulent eddy viscosity:

$$\boldsymbol{v_t = \tilde{v} f_{v1}}, \quad \boldsymbol{f_{v1} = \frac{\left(\frac{\tilde{v}}{v}\right)^3}{\left(\frac{\tilde{v}}{v}\right)^3 + C_{v1}^3}} \tag{19}$$

where C_{v1} is another model constant and v is the molecular viscosity.

The simulation results of the SA model are accurate even at intermediate spatial and temporal resolutions. In addition, the model is simple and numerically stable because it has only one extra transport equation [46]. All these advantages make the SA model especially suitable for wall turbulence, even in the case of an adverse pressure gradient [45]. ANSYS™ Fluent® "relaxes" the condition that the flow in the boundary layers be well-resolved (*i.e.*, have a spatial resolution comparable to a wall unit) by implementing its enhanced wall treatment, which is discussed later, in the SA model [45].

The k-ε family of turbulence models are also widely used in simulations of turbulent flows. Fluent® has three types of k-ε models: standard k-ε (SKE) [47], re-normalized group k-ε (RNGKE) [48] and realizable k-ε (RKE) [49]. Although the transport equations for each type of k-ε model are slightly different, the models all solve two coupled transport equations for the turbulent kinetic energy, κ, and the turbulent dissipation rate ε. The equations for the SKE model are:

$$\frac{\partial}{\partial t}(\boldsymbol{\rho k}) + \frac{\partial}{\partial x}(\boldsymbol{\rho k u}) += \frac{\partial}{\partial x}\left(\left(\mu + \frac{\mu_t}{\sigma_k}\right)\frac{\partial k}{\partial x}\right) + \frac{\partial}{\partial y}\left(\left(\mu + \frac{\mu_t}{\sigma_k}\right)\frac{\partial k}{\partial y}\right)\frac{\partial}{\partial z}\left(\left(\mu + \frac{\mu_t}{\sigma_k}\right)\frac{\partial k}{\partial z}\right) + G_k + G_b - \rho\varepsilon - Y_M + S_k \quad (20)$$

$$\frac{\partial}{\partial t}(\boldsymbol{\rho k}) + \frac{\partial}{\partial y}(\boldsymbol{\rho k v}) = \frac{\partial}{\partial x}\left(\left(\mu + \frac{\mu_t}{\sigma_k}\right)\frac{\partial k}{\partial x}\right) + \frac{\partial}{\partial y}\left(\left(\mu + \frac{\mu_t}{\sigma_k}\right)\frac{\partial k}{\partial y}\right)\frac{\partial}{\partial z}\left(\left(\mu + \frac{\mu_t}{\sigma_k}\right)\frac{\partial k}{\partial z}\right) + G_k + G_b - \rho\varepsilon - Y_M + S_k \quad (21)$$

$$\frac{\partial}{\partial t}(\boldsymbol{\rho k}) + \frac{\partial}{\partial z}(\boldsymbol{\rho k w}) = \frac{\partial}{\partial x}\left(\left(\mu + \frac{\mu_t}{\sigma_k}\right)\frac{\partial k}{\partial x}\right) + \frac{\partial}{\partial y}\left(\left(\mu + \frac{\mu_t}{\sigma_k}\right)\frac{\partial k}{\partial y}\right)\frac{\partial}{\partial z}\left(\left(\mu + \frac{\mu_t}{\sigma_k}\right)\frac{\partial k}{\partial z}\right) + G_k + G_b - \rho\varepsilon - Y_M + S_k \quad (22)$$

$$\frac{\partial}{\partial t}(\boldsymbol{\rho\varepsilon}) + \frac{\partial}{\partial \mathrm{x}}(\boldsymbol{\rho\varepsilon u}) = \frac{\partial}{\partial x}\left(\left(\mu + \frac{\mu_t}{\sigma_k}\right)\frac{\partial \varepsilon}{\partial x}\right) + \frac{\partial}{\partial y}\left(\left(\mu + \frac{\mu_t}{\sigma_k}\right)\frac{\partial \varepsilon}{\partial y}\right)\frac{\partial}{\partial z}\left(\left(\mu + \frac{\mu_t}{\sigma_k}\right)\frac{\partial \varepsilon}{\partial z}\right) + C_{1\varepsilon}\frac{\varepsilon}{k}\left(G_k + C_{3\varepsilon} + G_b\right) - \frac{C_{2\varepsilon}\,\rho\varepsilon^2}{k} + S_\varepsilon \quad (23)$$

$$\frac{\partial}{\partial t}(\boldsymbol{\rho\varepsilon}) + \frac{\partial}{\partial y}(\boldsymbol{\rho\varepsilon v}) = \frac{\partial}{\partial x}\left(\left(\mu + \frac{\mu_t}{\sigma_k}\right)\frac{\partial \varepsilon}{\partial x}\right) + \frac{\partial}{\partial y}\left(\left(\mu + \frac{\mu_t}{\sigma_k}\right)\frac{\partial \varepsilon}{\partial y}\right)\frac{\partial}{\partial z}\left(\left(\mu + \frac{\mu_t}{\sigma_k}\right)\frac{\partial \varepsilon}{\partial z}\right) + C_{1\varepsilon}\frac{\varepsilon}{k}\left(G_k + C_{3\varepsilon} + G_b\right) - \frac{C_{2\varepsilon}\,\rho\varepsilon^2}{k} + S_\varepsilon \quad (24)$$

$$\frac{\partial}{\partial t}(\boldsymbol{\rho\varepsilon}) + \frac{\partial}{\partial z}(\boldsymbol{\rho\varepsilon w}) = \frac{\partial}{\partial x}\left(\left(\mu + \frac{\mu_t}{\sigma_k}\right)\frac{\partial \varepsilon}{\partial x}\right) + \frac{\partial}{\partial y}\left(\left(\mu + \frac{\mu_t}{\sigma_k}\right)\frac{\partial \varepsilon}{\partial y}\right)\frac{\partial}{\partial z}\left(\left(\mu + \frac{\mu_t}{\sigma_k}\right)\frac{\partial \varepsilon}{\partial z}\right) + C_{1\varepsilon}\frac{\varepsilon}{k}\left(G_k + C_{3\varepsilon} + G_b\right) - \frac{C_{2\varepsilon}\,\rho\varepsilon^2}{k} + S_\varepsilon \quad (25)$$

$\mathcal{E}$: The turbulent dissipation rate, which determines how much of the mean flow kinetic energy is converted to turbulent eddies, and eventually to thermal energy by friction.

G_k: Production of turbulence kinetic energy from velocity gradients

G_b: The generation of turbulence kinetic energy due to buoyancy

Y_M: Dissipation of the turbulence kinetic energy due to the effect of compressibility

σ_ε and σ_k turbulent Prandtl numbers for ε and k, with default values of 1.3 and 1.0 respectively in Fluent®

$C_{1\varepsilon}$ and $C_{2\varepsilon}$ model constants, with default values of (for SKE) 1.44 and 1.92 respectively in Fluent® [45]

$$C_{3\varepsilon} = tanh\left|\frac{v}{u}\right|$$

where v is the component of the flow velocity parallel to the gravitational vector and u is the component of the flow velocity perpendicular to the gravitational vector.

Then the eddy viscosity μ_t can be written in terms of k and ε as follows:

$$\boldsymbol{\mu_t = \frac{C_\mu \rho k^2}{\varepsilon}} \quad \textbf{(26)}$$

where C_μ is a constant, empirically determined from experiments, and it is 0.09 in Fluent®

The RNGKE and RKE models are intended to solve the problem with the SKE model for flows that have high mean shear rate or large separation regions, where μ_t is

over predicted in SKE [49]. The definition of μ_t and the transport equation for ε are different for the RNGKE and RKE models compared with those for the SKE model, as detailed in references [47-49]. In most cases, the RKE model gives predictions that are in better agreement with experimental results for separated flows and flows with significant secondary flow [45].

The behavior of the models in predicting flow properties near walls is important in turbulent flows. ANSYS™ Fluent® provides four different wall functions for their KE models: standard wall functions, scalable wall functions, non-equilibrium wall functions and enhanced wall treatment. Only enhanced wall treatment was used in these simulations. Viscous effects are more dominant than turbulent effects due to very small local turbulent Reynolds numbers in the viscous sublayer near a solid wall [50]. Fully resolving this viscous region with its very high velocity gradients requires a mesh with a very fine spatial resolution. Using wall functions, which are essentially semi-empirical formulas that blend the viscous layer with the fully turbulent region in the flow, makes it possible to accurately simulate the near-wall region with a substantially coarser spatial resolution, and hence far fewer cells [45]. The near-wall spatial resolution is typically characterized in terms of wall units, or the non-dimensional distance from the wall y^+, where:

$$\boldsymbol{y^+ = \frac{yV_f}{v}}, \qquad \boldsymbol{V_f = \sqrt{\frac{\tau_w}{\rho}}} \tag{27}$$

V_f: Friction velocity

τ_w: Wall shear stress

ρ: Fluid density

v: Fluid kinematic viscosity

According to Launder and Spalding, standard wall functions are intended to be used with especially coarse spatial resolution near the wall, where viscous effects are imperceptible compared to the turbulent effects (outer layer) [50]. As explained in the Fluent® manual, these functions lose their validity with decreasing y^+ number when viscous effects start to overcome turbulent effects (viscous sublayer) [45]. A feature exclusive to ANSYS™ Fluent®, enhanced wall treatment, combines near-wall modeling and wall functions by resolving the viscous sublayer if y^+ is of the order of unity. The user manual best describes the details of how each model is combined to develop enhanced wall treatment [45]. Flexibility in the spatial resolution of the mesh at the wall is one advantage of enhanced wall treatment. This reduces computational time by requiring less resolution without sacrificing accuracy in the flow features in the boundary layer.

CHAPTER 3. NUMERICAL SIMULATIONS

This chapter describes the numerical models used in this work to conduct numerical simulations using the commercial software package ANSYS™ Workbench. First, the development of the numerical model is briefly described. Then, the appropriate software settings and problem setup are explained. Third, the procedures used to evaluate mesh convergence are given. Finally, the criteria used to determine whether a particular numerical solution has converged are discussed.

A numerical model was constructed to start evaluation and optimization of the T-tube concept. This model is similar to that developed by Crosatti [26] of the original T-tube test section proposed by Ihli et al. [6] except for some minor differences in geometric dimensions, having 10 cm tube length and 20 mm outer diameter instead 15 cm tube length and 14.9 mm outer diameter and fittings and mounting brackets (Ref. [6, 26]). The numerical mesh was created by importing CAD models constructed in SOLIDWORKS® to ANSYS™ Workbench. All of the numerical meshes were created using the ANSYS™ Meshing Tool. The cut-cell method, which can be automated for the most part while creating a high-quality mesh which consists mainly of hexahedral elements, was used for numerical discretization [51]. The numerical model was then analyzed using ANSYS™ Fluent® 17.1, which solves the governing equations for mass, momentum, and energy in the fluid, and conduction heat transfer in the solid.

3.1 Parameters and Problem Setup

The appropriate boundary conditions and flow parameters must be specified to determine the flow through this numerical model of the T-tube using the commercial code, ANSYS™ Fluent®l. Fluent® provides two different methods to solve the mass and momentum equations, namely pressure-based and density-based methods. The density-based solver solves the governing equations simultaneously and due to strong interdependence between density, momentum and energy in compressible flows, such as hypersonic flows and shock wave boundary layer interactions, it usually gives more accurate results in these flows. Given that the Mach number (*Ma*) is less than 0.3 for these T-tube simulations, and the flow is therefore incompressible, the pressure-based solver was used in this thesis. The pressure-based solver in Fluent® has three different segregated schemes (SIMPLE, SIMPLEC, PISO) and one coupled scheme for pressure correction. Although the coupled solver requires more memory to store all the results for the momentum and pressure-based continuity equations while solving for velocity and pressure fields, it converges more rapidly [45]. Therefore, the coupled scheme was used in these simulations.

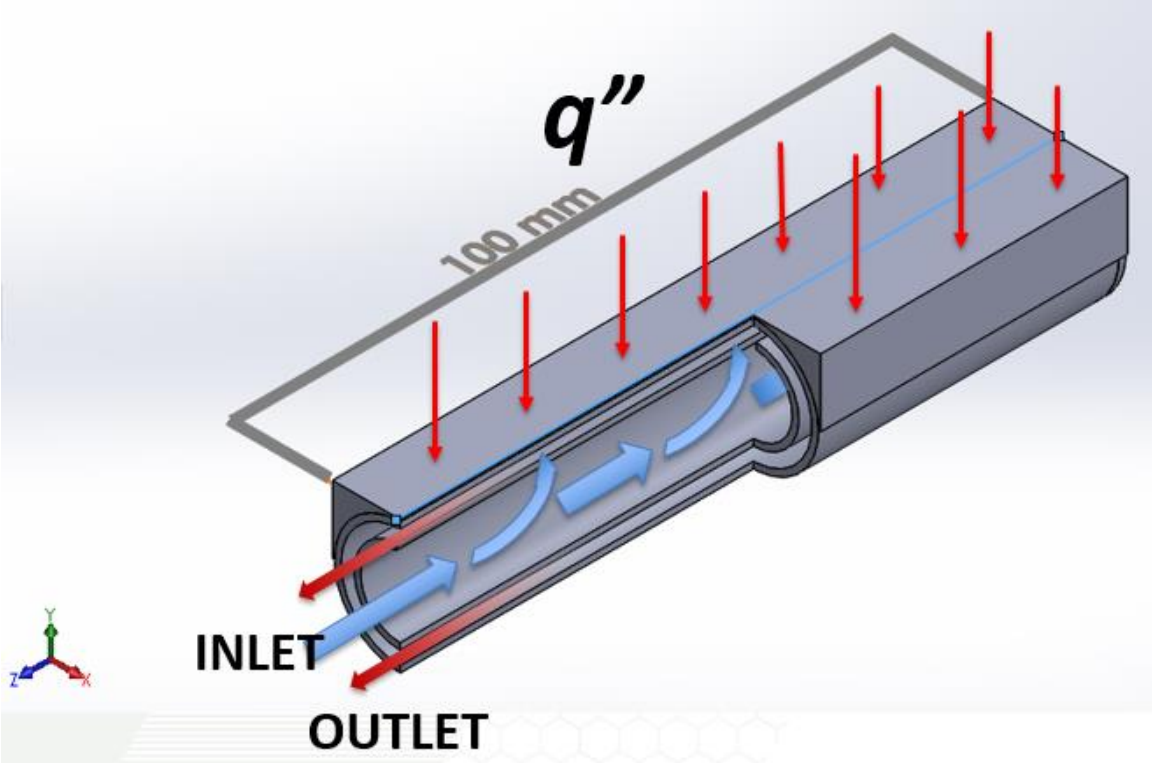

Figure 3.1 Cutaway view of the base model

The base model shown in Figure 3.1 consists of two concentric 100 mm long tubes, an armor tile and a plug. The wall thickness of each tube is 1 mm, the inner diameter (ID) of the inner tube is 12 mm, and the outer diameter (OD) of the outer tube is 20 mm. Helium enters the tube from the left side of the inner tube and flows along the axis, then accelerates through and exits the slot to form a 2D slot jet, impinging on the inner surface of the outer tube. The He then flows along the annular gap between the inner and outer tubes, and finally discharges from the left side of the annulus. The heat flux is applied to the upper flat surface of the armor tile. Because the divertor will be in a vacuum chamber, it is assumed that there is no convective heat transfer from the external surfaces.

As discussed in Chapter 2 numerical simulations of turbulent flows use a turbulence model to deal with the closure problem. The most common way to determine

the appropriate turbulence model for any turbulent flow simulation is validation—*i.e.*, compare the numerical predictions obtained with different turbulence models to experimental data on the same, or nearly identical, flow. Unfortunately, there are no appropriate experimental data to validate the simulations results presented in this thesis; the turbulence model used here was chosen based on a previous experimental validation of a simulation of a similar flow, albeit at quite different flow conditions, with experimental data summarized next.

Yang et al. [52] simulated heat transfer in slot jets of air impinging on a concave surface using the SKE turbulence model. They carried out simulations at *Re* between 5,920 and 23,700 and at a dimensionless jet-to-surface distance $H/B = 0.5 – 12$. A comparison of their numerical results with experimental data from previous studies [53, 54] showed that their predictions using the SKE turbulence model gave average Nusselt numbers that were within 15% of the experimental results in all cases.

In his study [26], Crosatti compared numerical predictions using the RNGKE and SKE models with his experimental data for the flow through a model T-tube, albeit for air at nearly ambient temperatures and pressures flowing through a brass test section. As shown in Figure 3.2, the predictions obtained with both models are similar, and in good agreement with the experiments.

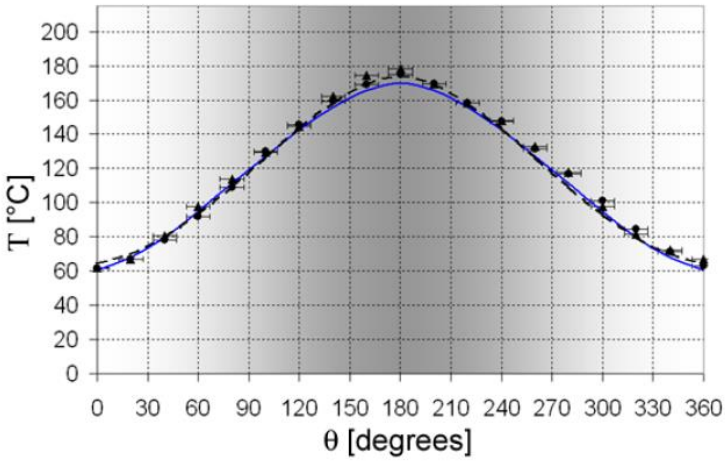

Figure 3.2 Experimental (•) and numerical (solid and dashed lines using standard and RNG k - ϵ models, respectively) results for T (θ) at TC locations #2 and #8 (double inlet, Re = 11, 000) [26]

Based on Crosatti and Yang et al.'s studies, the standard k-ε turbulence model was used for the simulations. Related correlations and equations to calculate turbulence parameters for the standard k-ε turbulence model are given below.

The turbulence parameters, namely the turbulence intensity I, and turbulence length scale l, are calculated from the following equations [45]:

$$\boldsymbol{I = 0.16(Re)^{-1/8}} \tag{28}$$

$$\boldsymbol{l = \frac{0.07L}{C_{\mu}^{3/4}}} \tag{29}$$

where L is the characteristic length and C_{μ}, one of the constants used in the k-ε model, has a default value of 0.09 in Fluent® .

For fully developed turbulent internal flows

$$L = D_H \tag{30}$$

$$\kappa = \frac{3}{2}\left(V_{avg} I\right)^2 \tag{31}$$

where κ is the turbulent kinetic energy V_{avg} is the average velocity at the inlet or exit.

Here,

$$V_{avg} = \frac{\dot{m}}{\rho_b A_b} \tag{32}$$

where $\dot{m}$ is the mass flow rate, A_b is the cross-sectional area and ρ_b is the density of the coolant at the inlet.

The turbulent dissipation rate is calculated from following relation:

$$\varepsilon = \frac{\kappa^{3/2}}{l} \tag{33}$$

Based on the given relations, turbulence parameters are as follows for 40 g/s mass flow rate:

Table 3 k-ε model input parameters

Location	Inlet	Outlet
Turbulent Kinetic Energy 'κ' $\left(\frac{m^2}{s^2}\right)$	5.10	3.77
Turbulent Dissipation Rate 'ε' $\left(\frac{m^2}{s^3}\right)$	2251.98	430.14

Heat transfer in a divertor is a conjugate heat transfer problem, which requires simultaneously solving conduction in the solid and convection and conduction in the fluid. The solid-liquid interface needs therefore to be coupled in conjugate heat transfer problems. In Fluent® , a fictitious "shadow" wall is created at the solid-liquid boundary to ensure that this boundary satisfies the no-jump temperature boundary condition and to couple the solid and fluid interfaces.

Although there is a third type of heat transfer, namely radiation, in addition to convection and conduction, radiation was not considered in these studies based on the following argument. In these simulations, the average surface temperature, $T_{s,avg}$, is about 700 K. Assuming that the divertor is inside of a reactor chamber, the shape factor, F_{rad}, is 1 and the emissivity of the copper alloy, ε_{rad}, is 0.6. The heat flux due to radiation

$$\boldsymbol{q''_{rad} = \varepsilon_{rad}\sigma F_{rad}(T_{s,avg}^4 - T_\infty^4)} \quad \textbf{(34)}$$

where T_∞= 300K is the temperature of the surrounding surfaces, and σ = 5.67×10^{-8} W/(m^2·K^4) is the Stefan-Boltzman constant. So

$$\boldsymbol{q''_{rad} \cong 7.9\ kW/m^2} \quad \textbf{(35)}$$

which is a negligible fraction (< 0.2%) of the total heat flux q''_{total} = 5000 kW/m^2. Radiation can therefore be neglected in these simulations.

Fluent® assumes constant material properties as a default, and its built-in material properties library does not include the copper alloy (CuCrZr) of interest in these studies. Given that these simulations consider materials at temperatures that are much higher than room temperature the model uses temperature-dependent properties for both the fluid and

solid domains. The specific heat (C_p) and thermal conductivity (λ) of the copper alloy (CuCrZr) used for the solid walls of the test section were obtained from the ITER Material Properties Handbook [55]. The constant-pressure specific heat C_p, thermal conductivity and viscosity of the coolant, helium used here were from the National Institute of Standards and Technology (NIST) WebBook [56]. Fluent® calculates the density of He from the ideal gas law. Further details of the temperature-dependent properties and related user-defined function (UDF) are given in Appendix A.

Although different mass flow rates and heat fluxes were used for different cases, most of the simulations were run with the same parameters. Unless otherwise stated for a particular case, flow and turbulence parameters that were used in the simulations are given in Table 4 and Table 3.

Table 4 Flow Parameters

Mass Flow Rate ($\dot{m}$)	40 g/s
Reynolds Number (Re)	40,000
Heat Flux (q")	5 MW/m^2
Inlet Temperature (T_{in})	300 K
Outlet Static Pressure (P_{out})	4 MPa

3.2 Mesh Refinement and Convergence

This section gives details on how the actual mesh used in these simulations was developed, and evaluated in terms of mesh convergence. In these simulations, a finer mesh is needed in regions with higher velocity and temperature gradients to accurately capture the flow features. Since using such a fine mesh for the entire model is very expensive in terms of computation time, size functions, which define the size of mesh elements, were used to minimize the number of required mesh elements. Figure 3.3 shows a typical mesh of the half-model used in most of the simulations. Here, the finest mesh is used over the impingement region and at the slot, which are the regions with the greatest velocity and temperature gradients, while a coarser mesh is used over the bulk of the inner tube. In addition, inflation layers are used at every fluid-solid interface to resolve the momentum and thermal boundary layers, again regions with large velocity and temperature gradients. Note that recommended value of y^+ for Enhanced Wall Treatment, discussed in the previous chapter and used for these simulations, is of order unity, and it is impractical to achieve this recommended value without using inflation layers. Here, a value of y^+ of about 3 was achieved using the inflation layers shown in the Figure. Since the geometry has bilateral symmetry, a 3D half model was used (for the case with non-uniform heating on only one side of the symmetry axis, a full model was used instead).

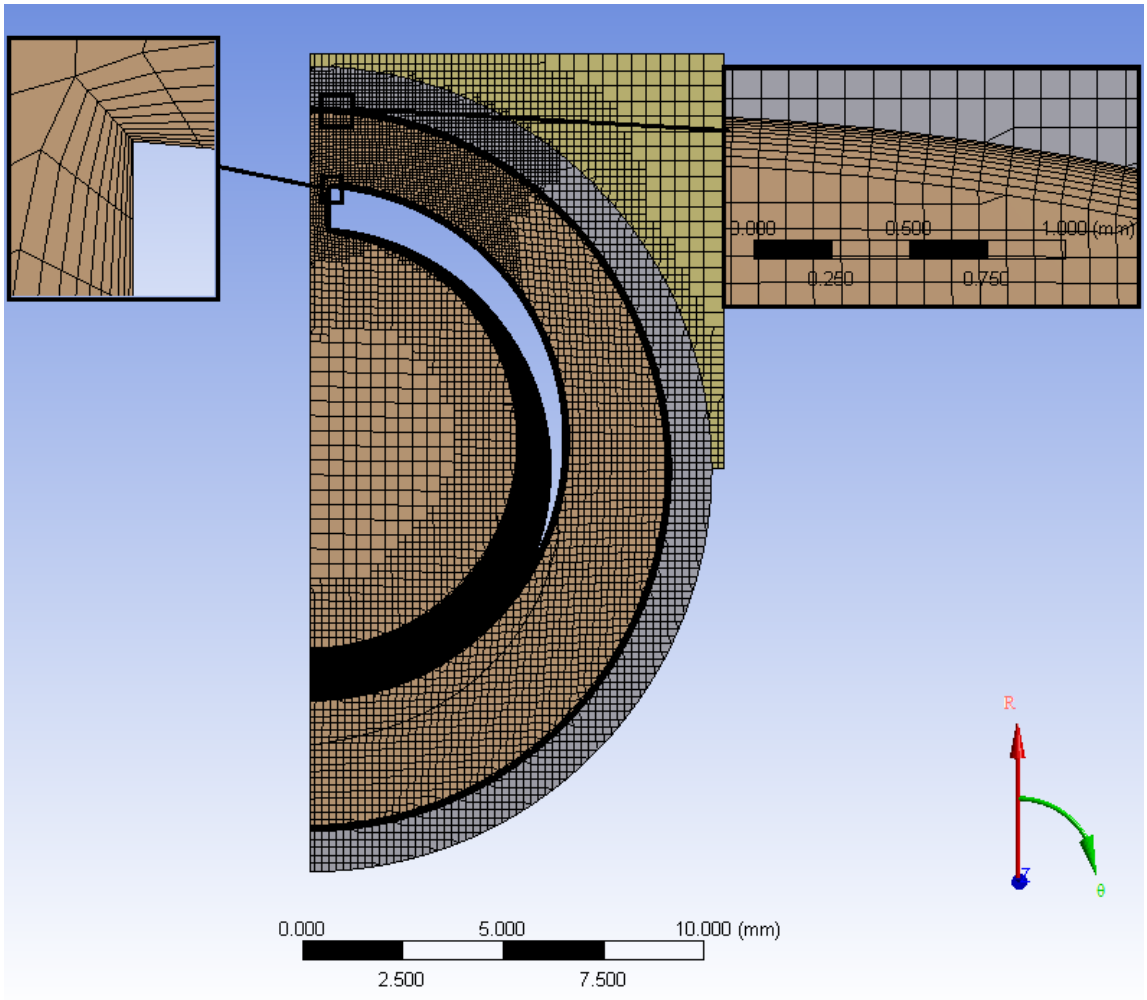

Figure 3.3 Cross-section of mesh and close-up on the slot and impingement surfaces showing inflation layers at the fluid-solid interface

A mesh convergence study was performed to determine the minimum number of mesh elements required to obtain an accurate representation of the flow (as defined later in this section). The mesh convergence study evaluated a half model of the case with a contraction of constant slope to a 2 mm diameter inlet manifold. Results were obtained for numerical half-models of this geometry with 0.5 million 1.1 million, 1.5 million, 2.6 million and 3.0 million elements by increasing element densities particularly on the impingement surface and at the slot. As can be seen in Figure 3.4, the temperature data

points, measured at 10 equally spaced point starting from the inlet side, obtained with simulations of numerical models with the greatest numbers of mesh elements, namely 2.6 million and 3 million, are in good agreement, even near the inlet (corresponding to an axial location of 0.13 m) and the outlet (corresponding to an axial location of 0.03 m), with a maximum temperature difference of 3 K. Since the discrepancy of 3 K is acceptable considering the iterative convergence error, which is discussed in the next section, we therefore conclude that the mesh of the half-model converges for a mesh of 2.6 million elements, and the mesh of the full model is converged for a mesh of about 5.2 million elements. The numerical models used in these simulations therefore contained at least 2.6 million and 5.2 million elements for the half- and full models, respectively, corresponding to a minimum spatial resolution of 6 μm, of the T-tube test section.

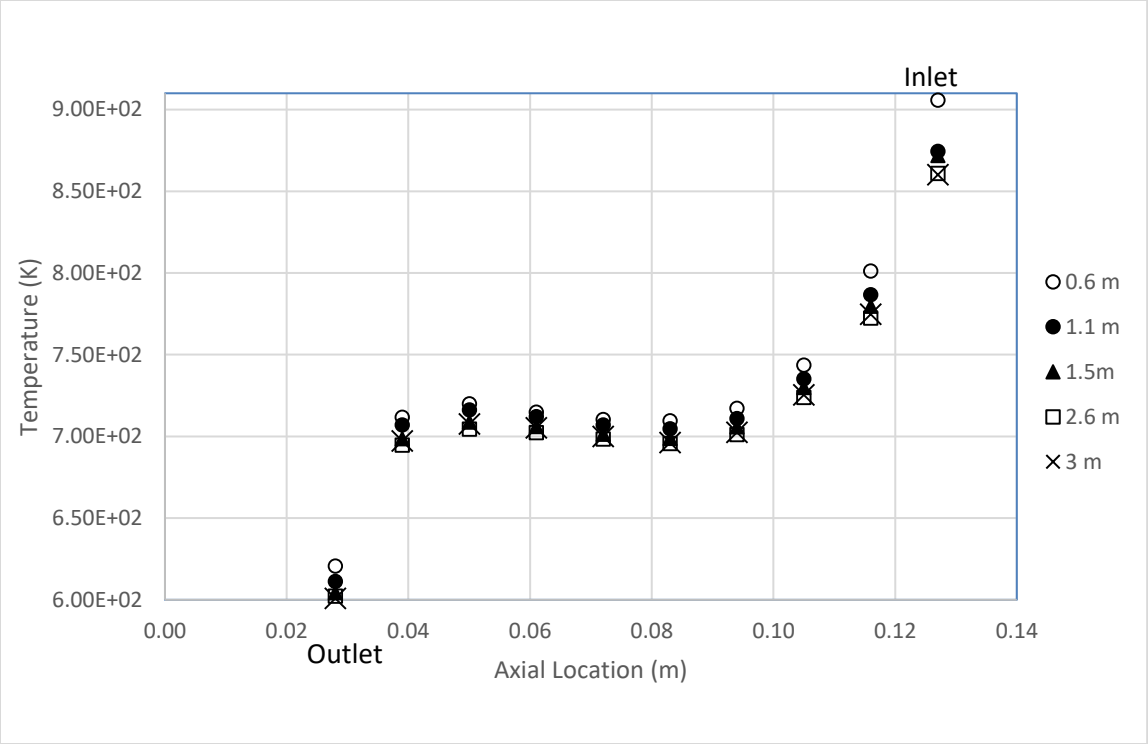

Figure 3.4 Temperature at the top of the armor for the five different meshes.

3.3 Solution Convergence

A solution (*vs.* mesh) convergence study was also performed for these simulations. Since it is impractical to achieve a "perfectly converged" solution, the numerical solution is usually defined to be "converged" when the discrepancy in some parameter of interest between two successive iterations is less than a pre-specified threshold value. The most common parameters used to determine convergence are residuals, imbalances and quantities of interest. The residual is the value of the difference in a particular quantity between two consecutive iterations, and is given as a fraction of the maximum residual value after *M* iterations, where *M* is 5 as default and can be set by the user in Fluent®. The

default value for residual convergence is 10^{-3} (*i.e.*, 0.1%) for all residuals in Fluent® except for the energy residual, where the default value is 10^{-6}. The energy imbalance, which is the difference between the total energy entering and leaving the system, is also widely used to determine solution convergence. Finally, variations in average flow properties such as pressure, temperature, lift force and mass flow rate over several iterations can be used to determine solution convergence. A solution can be defined to be "converged" if such variations are less than some pre-specified threshold value (or fraction of the average) after several iterations.

Most of the simulations presented here used the default residual convergence criteria given in Fluent®. As discussed in the next Chapter, the calculations requiring higher precision such as the comparison of mass flow rates in the non-uniform heating case, used a residual criterion of 10^{-5} (vs. the default value of 10^{-3}) for all residuals except the energy residual, where the criterion used was 10^{-8} (vs. the default of 10^{-6}). The fluctuations in flow properties such as the average inlet pressure, heated surface average temperature and heated surface maximum temperature (Figure 3.6) were also monitored to determine solution convergence. A typical convergence history for the case discussed in the mesh convergence study is shown in Figure 3.5

In Figure 3.5**,** all residuals decrease below 10^{-8} for energy and 10^{-5} for all other residuals after nearly 300 iterations and as shown in Figure 3.6, the maximum surface temperature does not change noticeably after about 150 iterations.

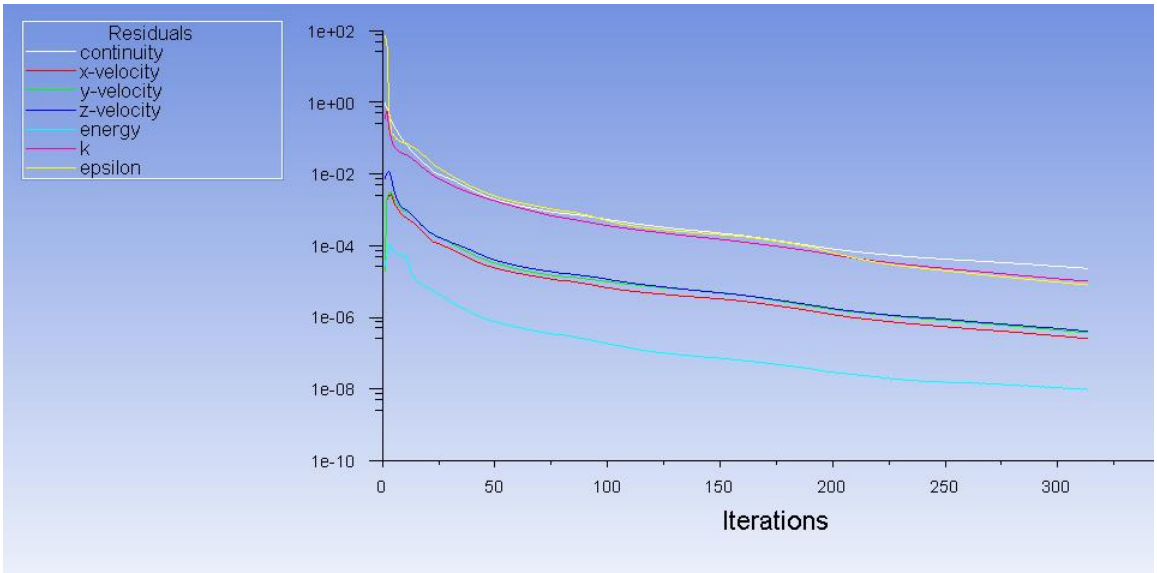

Figure 3.5 Convergence history for residuals

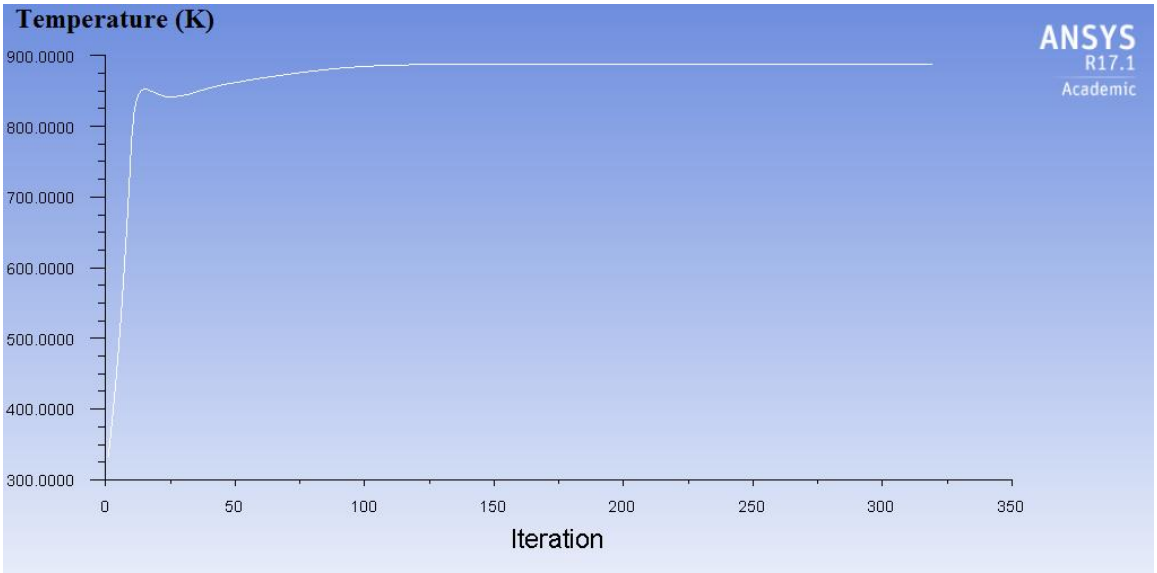

Figure 3.6 Convergence history of the maximum temperature at the top of the armor tile

CHAPTER 4. THERMAL-HYDRAULIC PERFORMANCE EVALUATION AND OPTIMIZATION

In this section, the effect of flow configuration on the thermal-hydraulic performance of the divertor module is evaluated. Two simple configurations, namely "counter-flow" and "parallel flow," with constant cross sections perpendicular to the flow directions are first investigated. Modified geometries with variable cross sections aimed at improving the thermal performance are then evaluated. The advantages and disadvantages of the two basic flow configurations and modifications thereof are presented.

4.1 Counter-Flow

Figure 4.1 is a schematic diagram of the counter-flow arrangement with constant cross section. The module consists of two concentric tubes, with one end open, while the other end is closed. The inner tube has a slot with uniform width along its entire length. The coolant enters the inner tube through the open end and flows axially along its length towards the closed end. As it flows axially towards the closed end of the tube, the coolant exits radially through the slot as a planar jet, thereby impinging on and cooling the outer tube. The heated coolant flows through the annular region between the two tubes and exits through the open end. In this configuration, the incoming cold coolant and the exiting heated coolant flow in opposite directions; hence, this configuration is referred to as the "counter-flow" arrangement.

The main advantage of the counter-flow arrangement is that both the inlet and outlet streams are accessible from one end, which simplifies manufacturing and integration

within the overall flow system. However, as the incoming coolant progresses towards the closed end of the tube, the flow rate decreases, thereby decreasing the jet velocity issuing from the slot. This, in turn, results in significant reduction in the average heat transfer coefficient, and a corresponding increase in temperature along the inner surface of the outer tube. A large axial temperature gradient is undesirable because the resulting thermal stresses which may exceed the limits dictated by material properties.

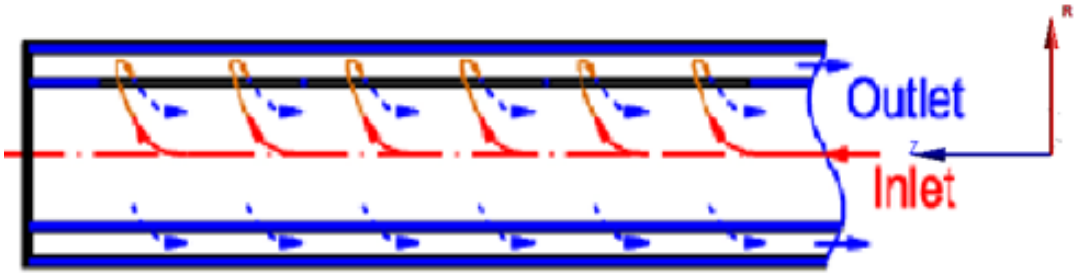

Figure 4.1 Schematic view of counter-flow

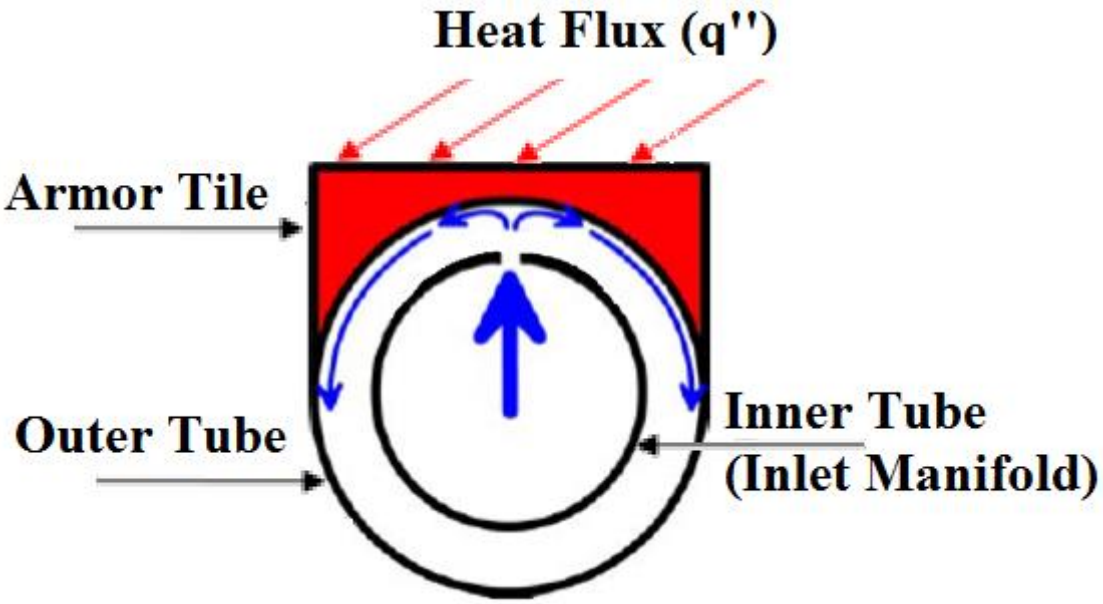

Figure 4.2 Schematic view perpendicular to the axis

Simulation results for a typical counter-flow configuration case are shown in Figure 4.3. Here, the inner diameter of the inner tube is 12 mm, the outer diameter of the outer tube is 20 mm and the slot width is 1 mm. The overall tube length is 100 mm. The coolant (helium) enters the tube with a temperature of 300 K at a flow rate of 40 g/s. The outlet pressure is 4 MPa and the incident heat flux is 5 MW/m^2. The corresponding Reynolds number at the exit of the slot is 4.0×10^4. The results show that the highest axial coolant velocity (~ 150 m/s) occurs at the exit near the bottom of the annulus (Figure 4.3). High coolant exit velocities increase the pressure drop in the module and, hence, the required pumping power. The coolant exit velocity can be decreased by increasing the annular gap between the inner and outer tubes (*i.e.*, the jet stand-off distance). However, jet impingement studies, as discussed in Chapter 2, show that the optimum stand-off distance is approximately twice the slot width. Alternatively, the tubes may be placed eccentrically with a larger gap at the bottom. While this may decrease the pressure drop, it may also results in significant azimuthal variations in the heat transfer coefficient and corresponding increases in temperature. While this specific configuration was not examined, a tapered inner tube design which effectively varies the cross sectional area of the annulus along the tube length has been evaluated (see Section 4.1.2 below).

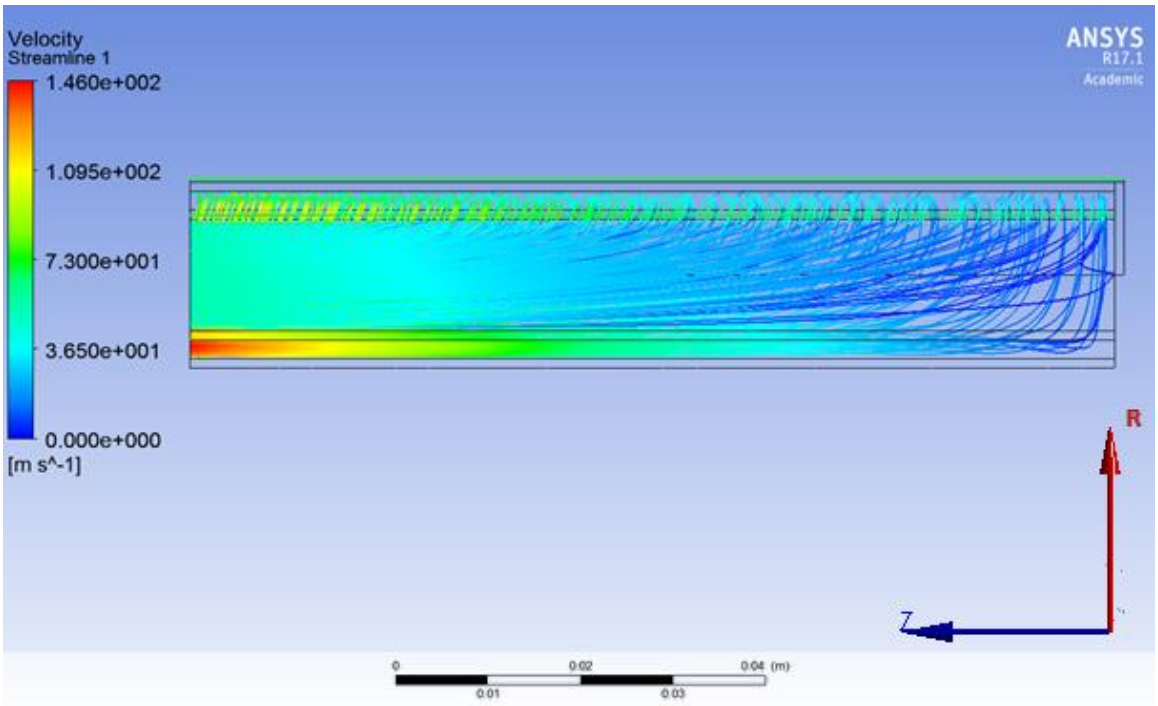

Figure 4.3 Velocity streamlines of counter-flow

The significant reduction in the heat transfer coefficient along the tube axis as the coolant approaches the stagnation zone near the closed end of the tube is a major concern for this flow configuration. Figure 4.4 shows axial variation of the heat transfer coefficient at the symmetry axis of the cooled surface for the conditions discussed above. The heat transfer coefficient decreases by more than a factor of two along the 10 cm length of the tube.

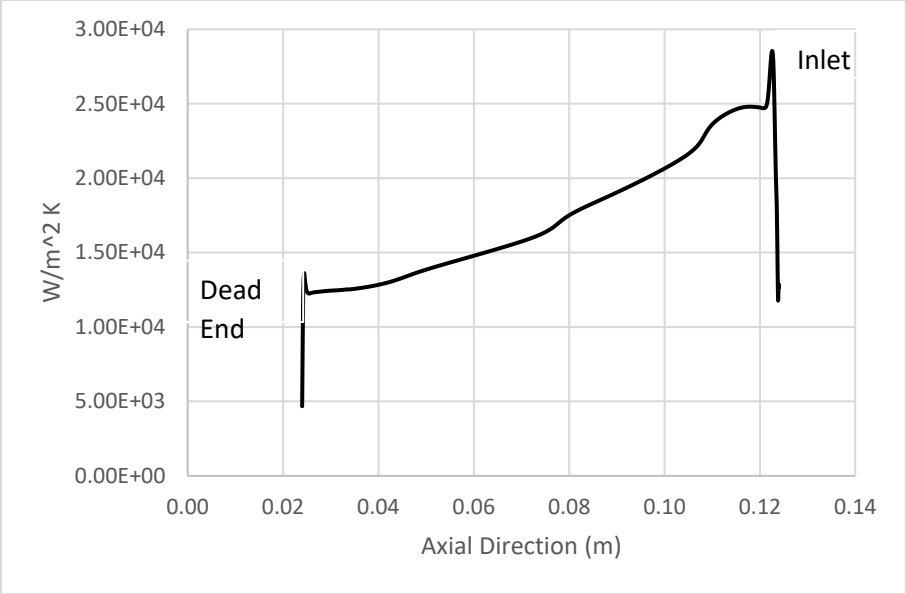

Figure 4.4 HTC variation on the cooled surface

The reduction in the heat transfer coefficient increases the outer tube wall temperature, and hence, the top surface temperature of the armor tile (see Figure 4.5). As noted earlier, the large temperature gradients along the 10 cm length of the module raise concerns regarding the resulting thermal stresses; these, however, will depend on various factors such as fixation of the modules. Mechanical analyses, including stress analyses, are not covered in this thesis.

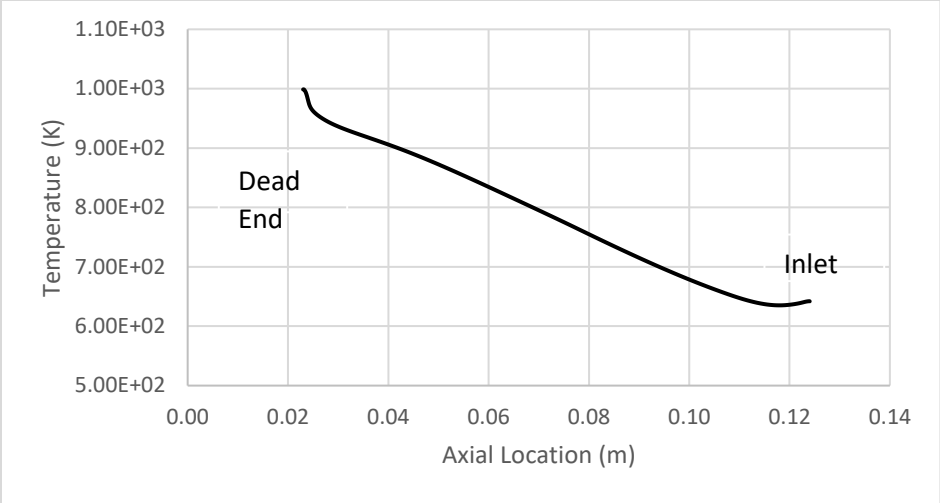

Figure 4.5 Temperature distribution at the top of the armor tile

Design Modifications for the Counter-Flow Configuration:

To reduce the axial variations in heat transfer coefficient and temperature, several possible modifications have been examined. Those having no or negative effect are mentioned briefly in section 4.1.1; only modifications with a positive effect on these axial variations are presented in Section 4.1.2.

4.1.1 Unsuccessful Modifications

Variable Slot Width Along Tube Axis

Instead of having a constant-width slot, a slot with a width varying linearly from 0.5 mm at the inlet end to 2.5 mm at the closed end of the tube was investigated (see Figure 4.6). All other parameters remain unchanged. The basic idea is that the coolant jet mass flow near the closed end of the tube can be increased by increasing the cross-sectional area

of slot. Clearly, while the coolant mass flow rate increases, the jet velocity may decrease, which, in turn, may further decrease the local heat transfer coefficient near the closed end of the tube, thereby increasing the tile surface temperature difference between the two ends of the tube.

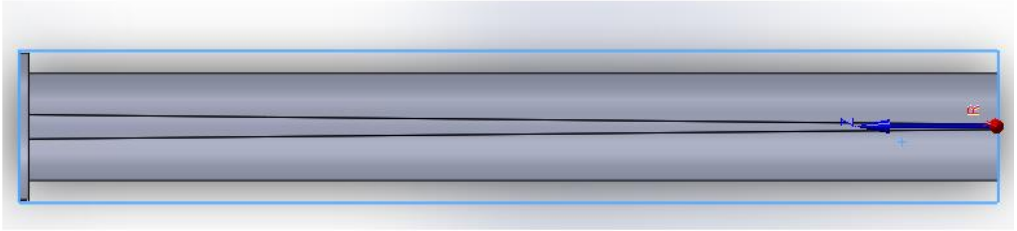

Figure 4.6 Top View of Varying Slot Width Model

Variable Slot Thickness

In this design, the slot entrance has been tapered so that the thickness decreases from the inlet side to the dead end side with a 45° slope (see Figure 4.7). The untapered portion of the tube wall has a thickness that decreases linearly from 1 mm near the tube inlet to 0 mm at the closed end of the tube. The basic idea is that having a shorter flow passage reduces the pressure drop, which increases the flow rate through the slot near the stagnant zone of the tube. Unlike the previous case of varying slot width, the idea here is that the increase in flow rate will also increase the jet velocity since the flow exit area remains unchanged. Surprisingly, the HTC decreased near the dead end compared to the base case with uniform tube cross section. The reason for this result might be flow disruption at the tapered section.

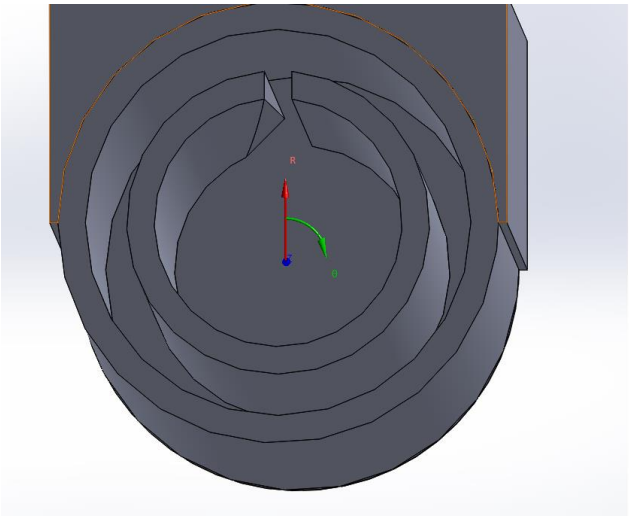

Figure 4.7 CAD View of Tapered Slot Inlet

Tapered Slot Thickness

As shown in Figure 4.8, the entire slot length is tapered from the inside diameter of the inner tube to the halfway point of the inner tube thickness. The basic idea is to reduce the flow resistance of the slot thereby increasing the flow rate (or reducing the overall pressure drop) and thereby improve performance. However, this change in geometry produced an insignificant change in temperature since the total flow rate was kept constant as that for the nominal case.

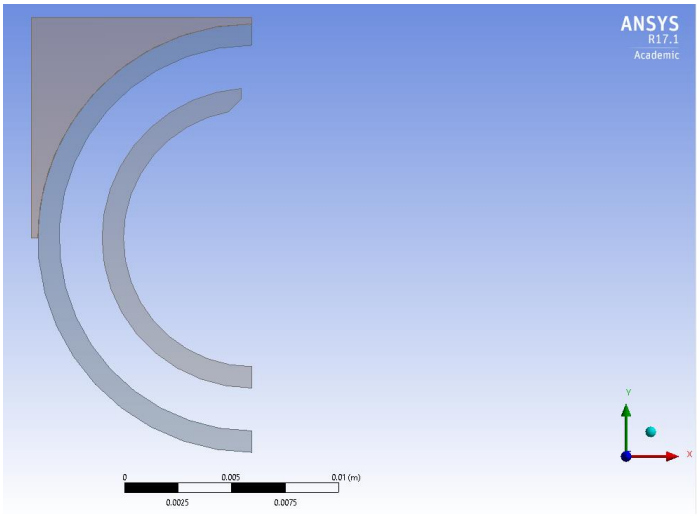

Figure 4.8 Tapered Slot Thickness

4.1.2 Successful Modifications

In this section, several geometric changes to the base case design have been analyzed. These changes were deemed significant, inasmuch as they reduce axial gradients in the heat transfer coefficient and surface temperatures.

Tapered Inlet Manifold Design

In this case, the inner tube diameter is not constant. Instead, its inner diameter changes along the axis from 12 mm near the inlet to 2 mm near the closed end of the tube. A similar study was reported in the literature for the ARIES-CS T-tube geometry (see Figure 4.9). The study does not report the axial temperature distribution; however, it states that maximum temperature decreases considerably [57]. It should be noted that unlike the straight tube shape examined here, the coolant flow in the T-tube design enters at the center of the T-tube and splits into two directions.

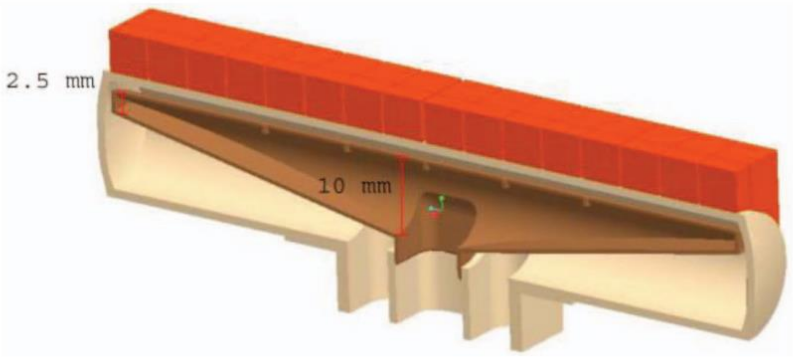

Figure 4.9 Modified T-tube design with cartridge tapered from 10 to 2.5 mm [57]

Three different axial variations of the inner tube diameter have been evaluated (see Figure 4.10). In the first case, the inner tube diameter is linearly tapered from its maximum value at the inlet to its minimum value at the closed end of the tube. In the second design the inner tube diameter varies exponentially between its maximum value near the inlet and its minimum value at the closed end. The third configuration uses three linear segments approximating the exponential variation of the inner tube diameter along its length. All three designs produced nearly similar results, with the first design producing slightly better performance in addition to being simpler to manufacture.

The logic for examining an exponentially varying diameter is that the jet velocity decreases along the axis nearly exponentially for an inlet with constant cross-section. It was argued that an exponentially contracting inner manifold might decrease the internal pressure gradient along the axis and might thus result in a more uniform jet velocity. However, the flow is not only driven by this pressure gradient, but also by the pressure difference across the slot. Therefore, modifying the inlet manifold for counter-flow gives limited control over flow distribution. Finally, the third geometry represents a curve fitted approximation of the exponentially varying diameter, which may be easier to machine.

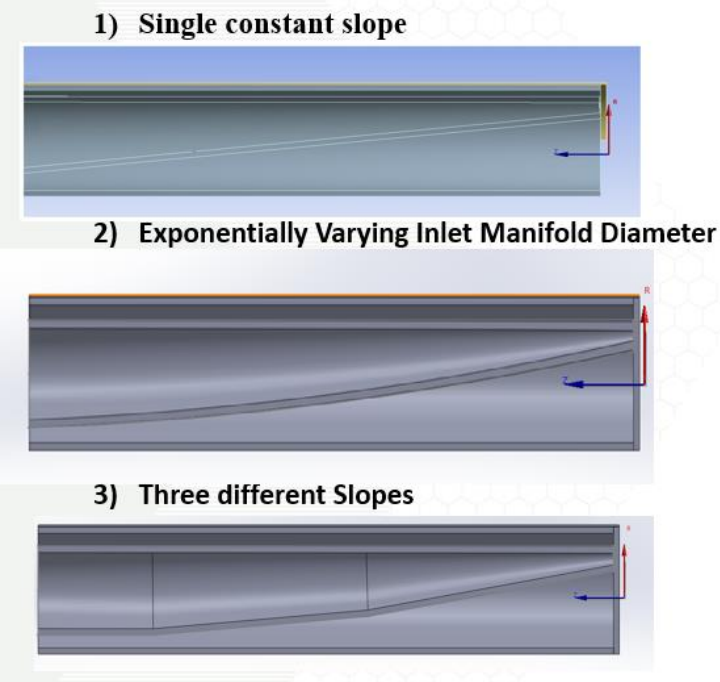

Figure 4.10 CAD model of different contraction patterns

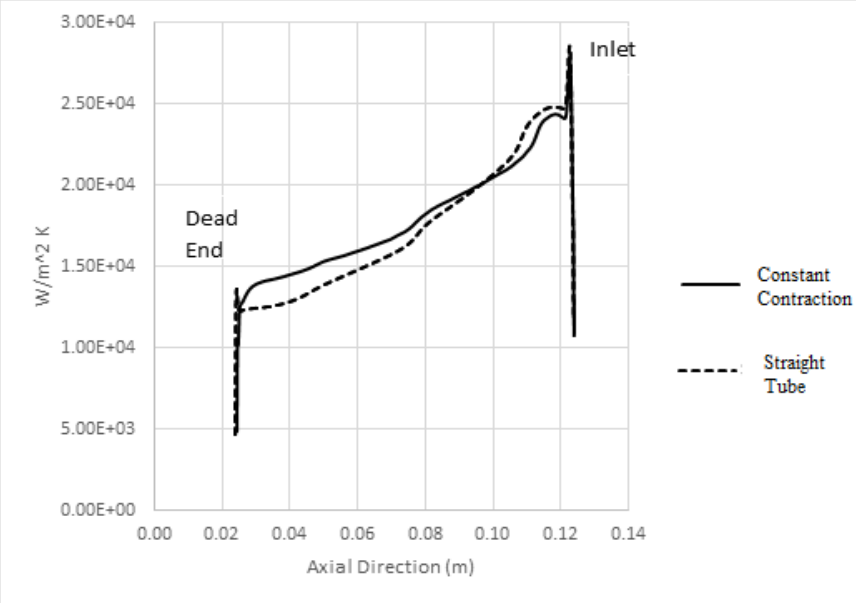

Figure 4.11 HTC Comparison at θ=0°

Figure 4.11 shows variations of the heat transfer coefficient for the linearly tapered inner diameter (case 1 above) against that for the base case with uniform inner diameter. The results show that although the tapered manifold design produces a lower HTC near the tube inlet, it provides better cooling near the closed end of the tube. The later effect is significant since poor heat transfer near the closed end side of the tube is the limiting factor for the counter-flow case.

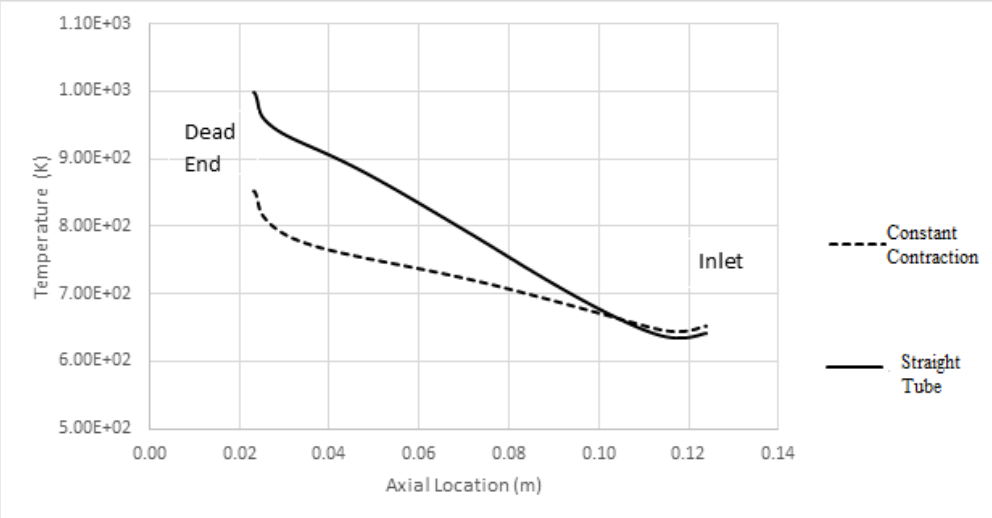

Figure 4.12 Temperature comparison of straight tube and modified manifold at the top of the armor tile

The enhancement in the heat transfer coefficient near the closed end of the tube, significantly reduces the tile surface temperature at that location as compared to the base case with uniform inner tube diameter (see Figure 4.12). The change in temperature is a result of not only the axial variation of the heat transfer coefficient, but also the azimuthal variations of the heat transfer coefficient as shown in Figure 4.13.

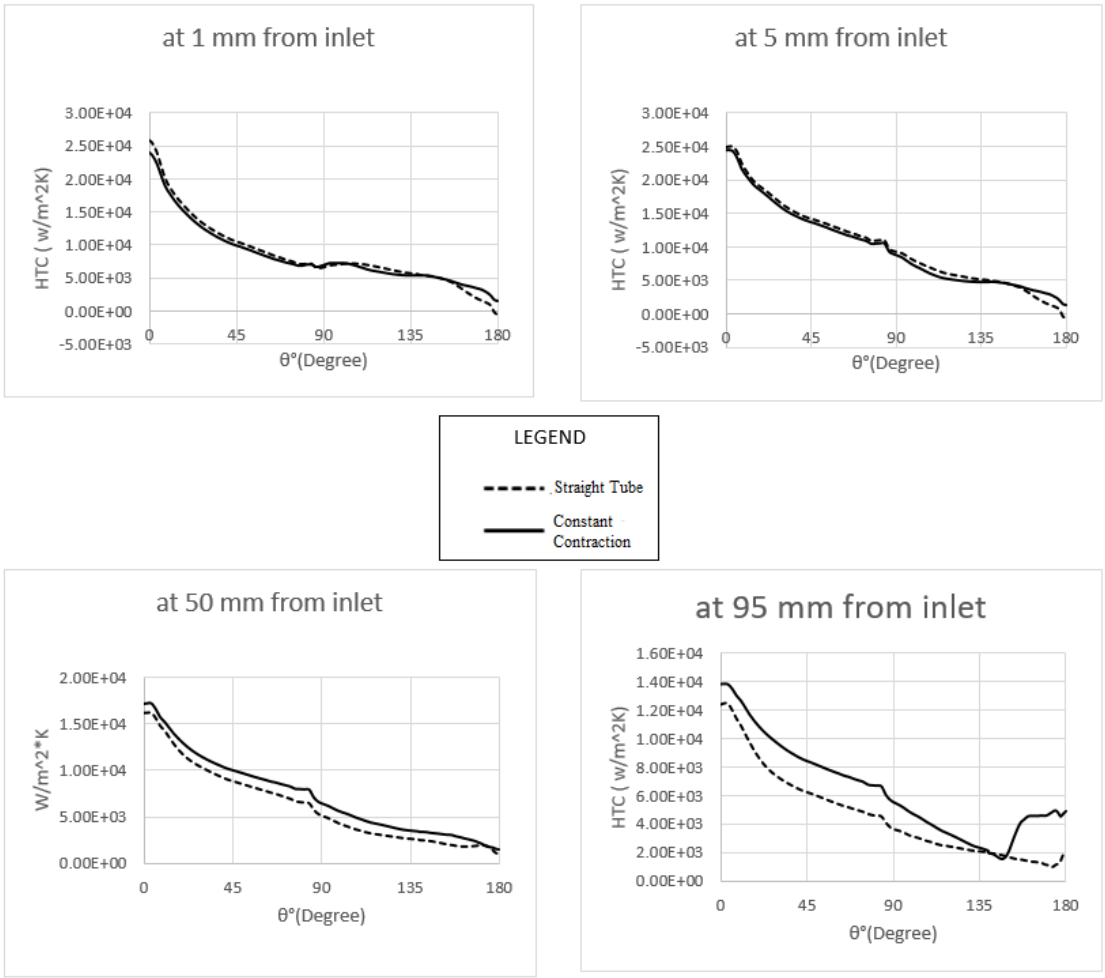

Figure 4.13 Azimuthal HTC comparison at different sections

As shown in Figure 4.13, the azimuthal distributions of HTC for two axial locations near the inlet (1 mm and 5 mm from the inlet) are nearly identical to those for the base case. On the other hand, at locations closer to the dead end, the results diverge, and the modified manifold case can sustain higher HTC over a wider range of angles.

There is an unexpected increase in HTC at 95 mm from the inlet, which boosts the cooling effect for the modified geometry. The jump is caused by flow recirculation in that region. Such recirculation can be clearly seen by comparing the streamline plots for both

the base case with constant diameter (Figure 4.14) and that for the tapered manifold configuration (Figure 4.15).

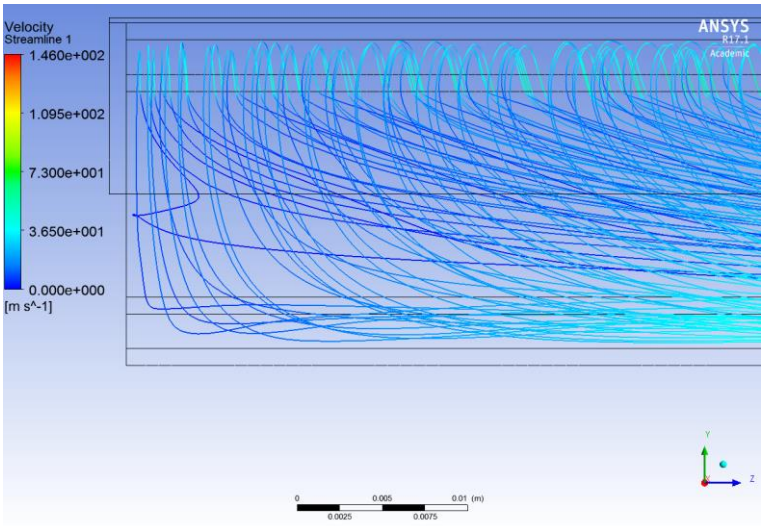

Figure 4.14 Stream line plot of straight tube

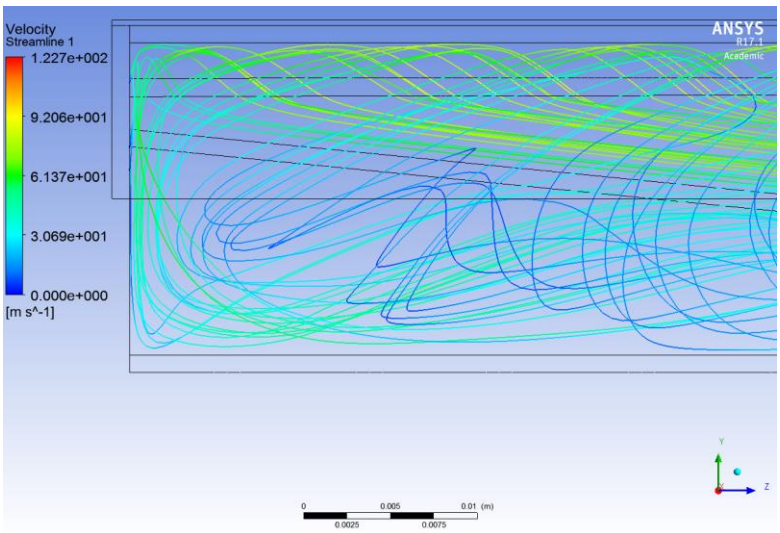

Figure 4.15 Stream line plot of modified geometry

The above discussion points to two inherent problems with the counter-flow arrangement. The first pertains to the flow restriction at the outlet. This issue remains even when the inner tube diameter is gradually reduced to enhance the coolant flow and heat transfer characteristics near the closed end of the tube. The second problem is that modification of the inner tube diameter has a limited impact on the jet velocity variation along the tube axis. The jet velocity is primarily affected by the pressure difference between the annulus and the inner tube. Since the lowest pressure is at the exit, while the highest pressure is at the inlet, the maximum pressure difference across the slot will always occur at the inlet axial position, while the minimum driving pressure difference across the slot will occur near the closed end of the tube. Hence, with a uniform slot geometry, there is no way to maintain a constant jet velocity along the tube axis.

4.2 Parallel Flow

In this section, the parallel flow configuration is investigated. In this case, the inner tube is closed at the far end, while the exit annulus is plugged at the near end of the concentric tube arrangement (see Figure 4.16). Therefore, the cold coolant will always flow from the inlet towards the closed end and will be gradually discharged as a planar jet exiting the slot and impacting the inner surface of the outer tube. The inner tube flow rate will gradually decrease in the flow direction until it reaches zero at the plugged end of the tube, while the heated coolant flow rate will gradually increase as it flows within the annulus towards the exit. In this case, both the cold coolant flowing through the inner tube, and the heated coolant flowing through the annulus will flow in parallel.

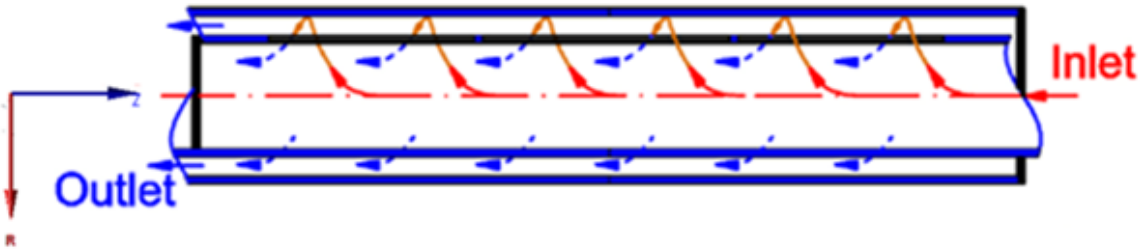

Figure 4.16 Schematic view of parallel flow

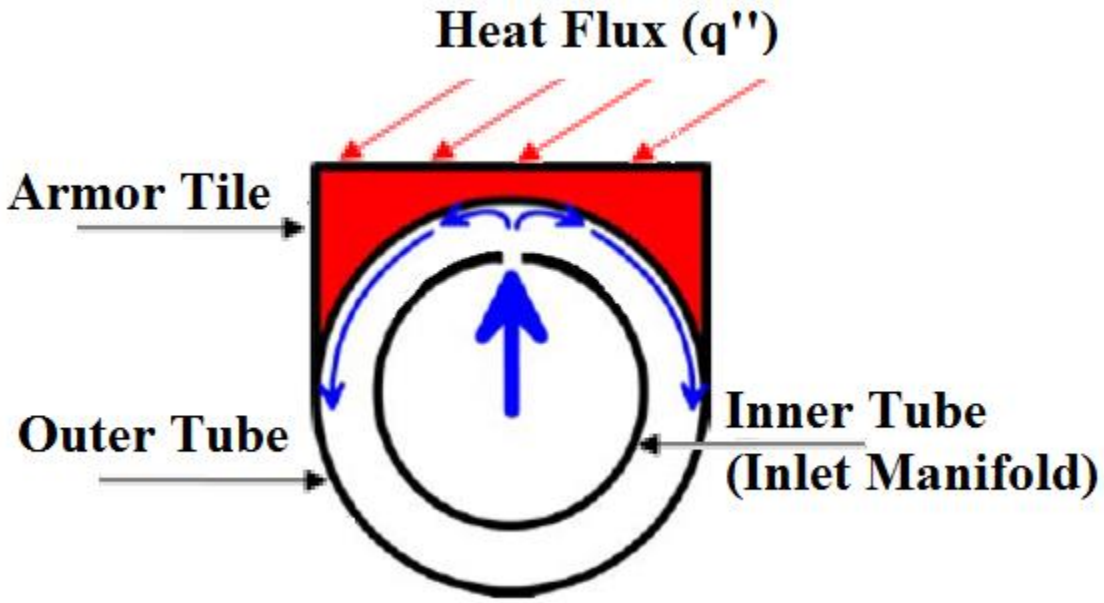

Figure 4.17 Schematic view perpendicular to the axis

The primary advantage of the parallel flow arrangement is that it offers the possibility of a more uniform pressure difference along the tube axis between the cold incoming coolant and the heated exiting stream, thereby providing the opportunity for a more uniform jet velocity, and hence, a more uniform heat transfer coefficient along the flow direction. This, in turn, reduces the temperature gradients along the tube length, and hence, the thermal stresses within the structure. This, however, may not be realized without significant modifications to the base line geometry. As can be noted from Figure 4.16, the

main disadvantage of the parallel flow arrangement is the possibility of flow stagnation within the annulus near the inlet, which may negatively impact the heat transfer coefficient in that region.

Simulation results for the parallel flow arrangement using the same set of parameters as those used for the counter-flow case are shown in Figure 4.18 below. The axial momentum of the incoming coolant at the inlet section makes it more difficult for the coolant to flow radially through the slot in the immediate vicinity of the inlet. This reduces the heat transfer coefficient and causes a significant increase in wall temperature near the inlet.

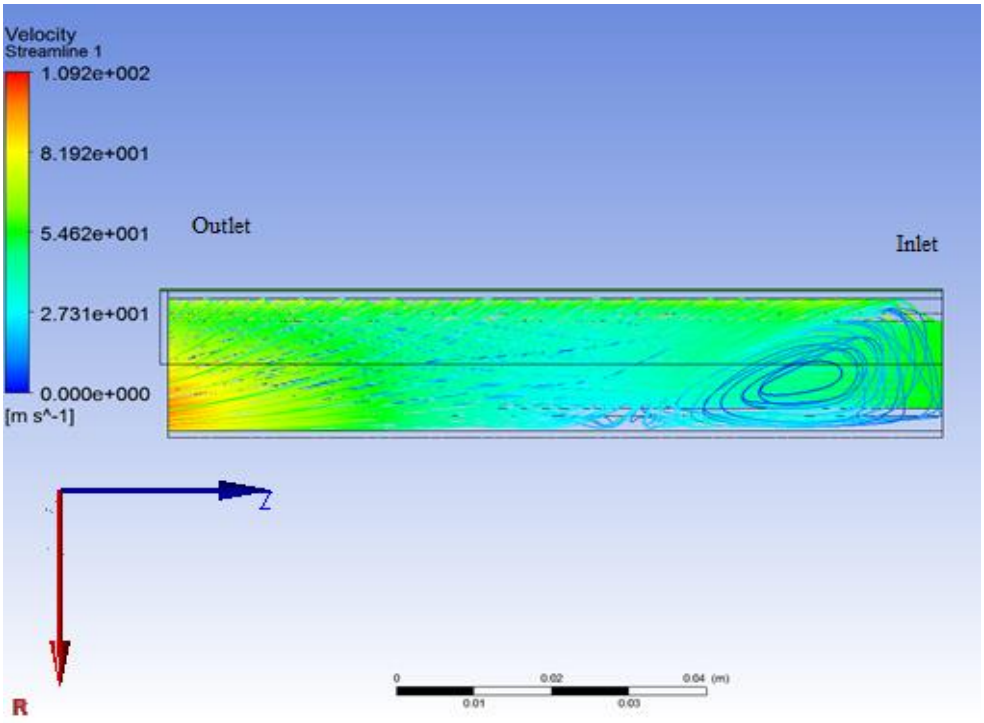

Figure 4.18 Velocity streamlines of parallel flow

Figure 4.19 compares the axial variation of the heat transfer coefficient for the parallel flow and counter-flow arrangements, while Figure 4.20 compares the tile surface temperature distribution for the two cases. The results show similar, albeit reversed, patterns for the axial variations of HTC and tile surface temperature. It is noted, however, that the calculated tile surface temperature values for the parallel flow arrangement are generally higher than those for the counter-flow configuration.

As was done for the counter-flow case, several geometric modifications to the parallel flow "base case" have been examined. Modifications that result in no improvements are presented in Section 4.2.1 below, while those that significantly enhance performance are presented in Section 4.2.2.

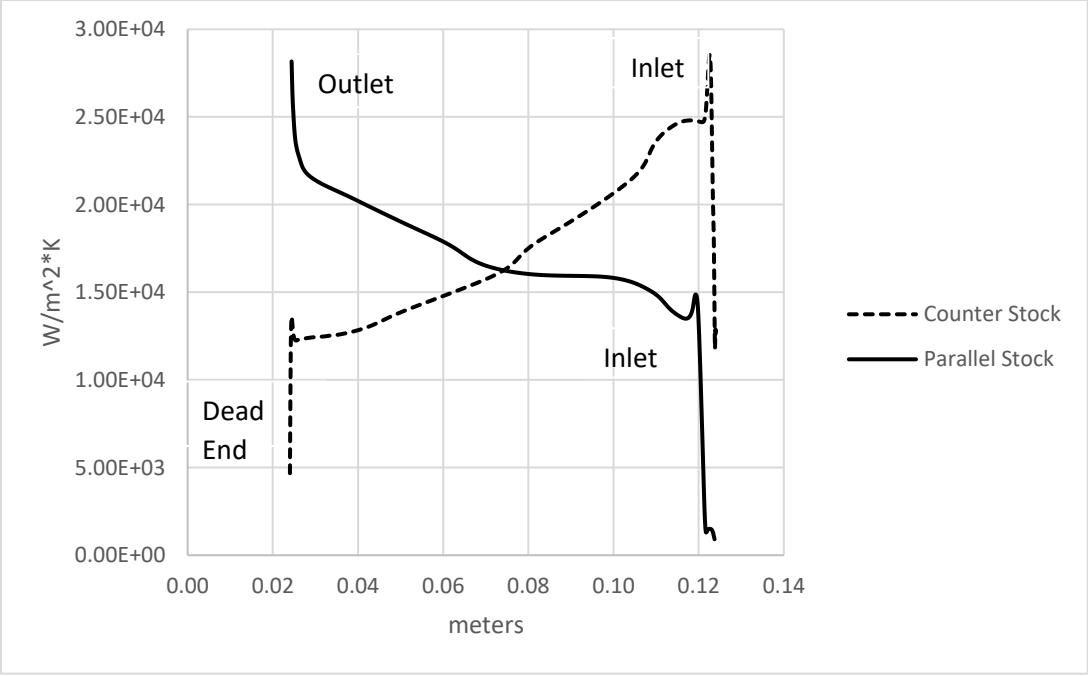

Figure 4.19 HTC Comparison at θ=0°

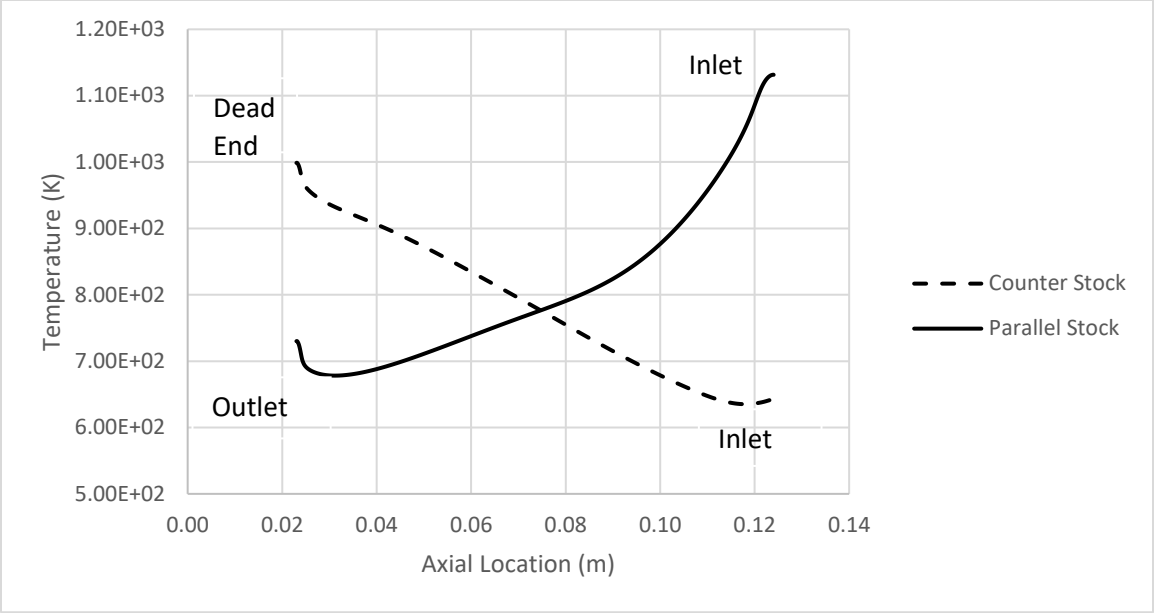

Figure 4.20 Temperature comparison at the top of the armor tile for stock geometries

4.2.1 Unsuccessful Modifications

Parabolic Shaped Inlet Manifold

Since the elevated temperatures for the base case were observed near the two ends, the inner tube was modified to contract at the middle and again expand near the outlet in order to enhance the uniformity of the flow distribution along the slot. Although the temperature in this configuration becomes lower at the outlet side, the temperature at the inlet side, which is the limiting condition for the parallel flow configuration, increases. Additionally, the temperature variation becomes more pronounced that the base case. Hence, no further analysis was done for this configuration.

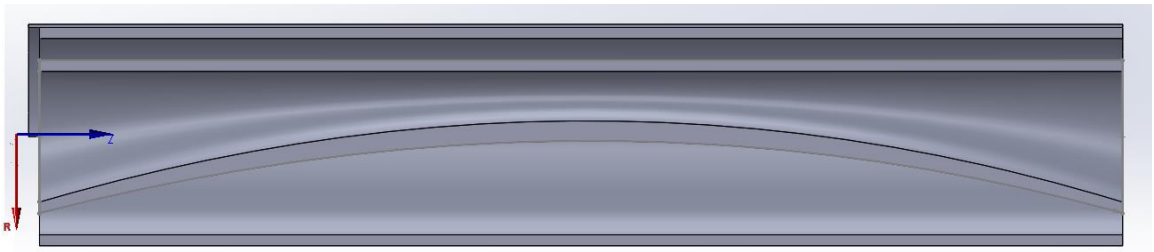

Figure 4.21 CAD View of Parabolic Shaped Inlet Manifold

Wider Slot Width at Higher HTC Locations

Increasing the jet cross section results in lower velocities and eventually lower HTC. One would expect this change to produce a more uniform temperature distribution than the base case, albeit sacrificing some heat dissipation capacity (Figure 4.22). As expected, due to the lower velocities, the overall temperature distribution was generally higher; however, in contrast to the assumed benefit, the temperature increase near the inlet was higher than the temperature increase at the outlet end, and therefore the total temperature variation was worse than was observed for the constant width case. This may be caused by the enhanced non-uniformity in coolant flow caused by the modification in geometry.

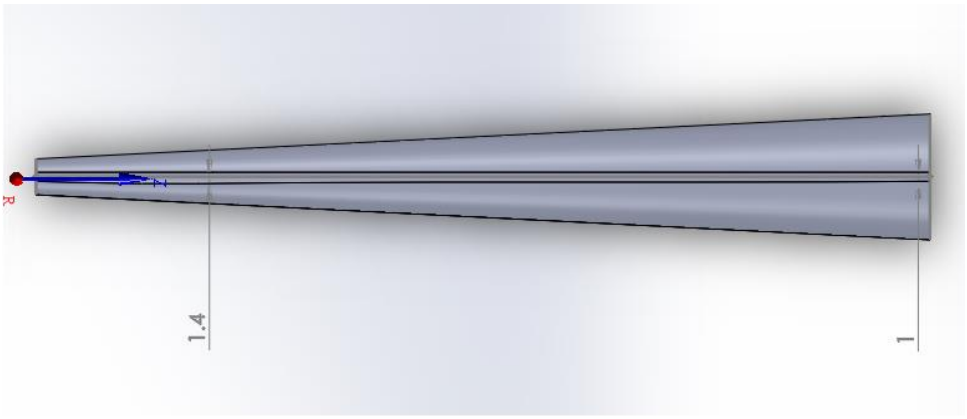

Figure 4.22 Top View of the Inlet Manifold with Variable Slot Width

4.2.2 Successful Modifications

Variable Inlet Manifold Diameter

In this case, the same variable inlet manifold geometries tested for the counter-flow case are examined. The inner tube diameter varies from 12 mm at the open inlet to 2 mm at the blocked end. Simulations were performed at the same operating conditions used for the base cases [40 g/s mass flow rate (*Re* = 40,000), 4 MPa outlet pressure and 5 MW/m^2 incident heat flux].

Comparisons between the heat transfer coefficients for the base parallel flow case and the linearly varying tapered inlet manifold case are shown in Figure 4.23. The heat transfer coefficients for the tapered manifold case are significantly more uniform than those for the base case. Additionally, the heat transfer coefficients are generally higher for the tapered inlet manifold case, except near the exit where the increase in the annulus cross

section area causes a reduction in axial flow velocity and a reduction in the heat transfer coefficient on the outer tube surface.

Figure 4.24 shows the corresponding tile surface temperature distributions for both the base case and the tapered manifold case. As expected, the increase in the heat transfer coefficient along most of the tube length results in a significant reduction in tile surface temperature. Also, the reduction in the heat transfer coefficient near the exit due to the reduction in axial flow velocity cause the wall temperature, and hence the tile temperature to increase above its value for the base case with constant inner tube diameter. Nevertheless, the temperature distribution for the tapered manifold case is significantly more uniform than the base case.

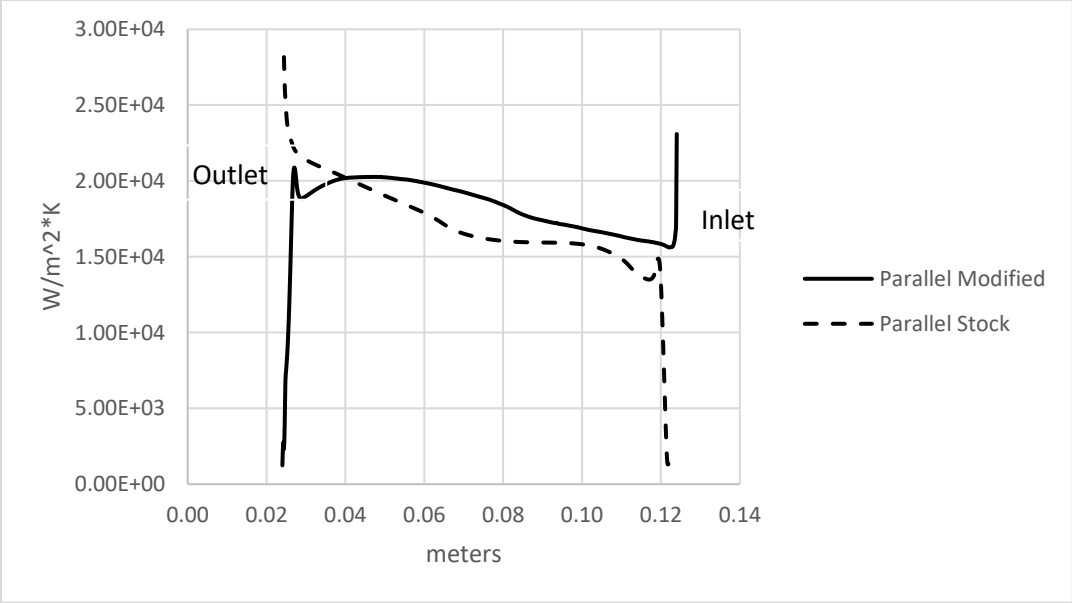

Figure 4.23 HTC Comparison of the stock and the modified geometries for parallel flow at θ=0°

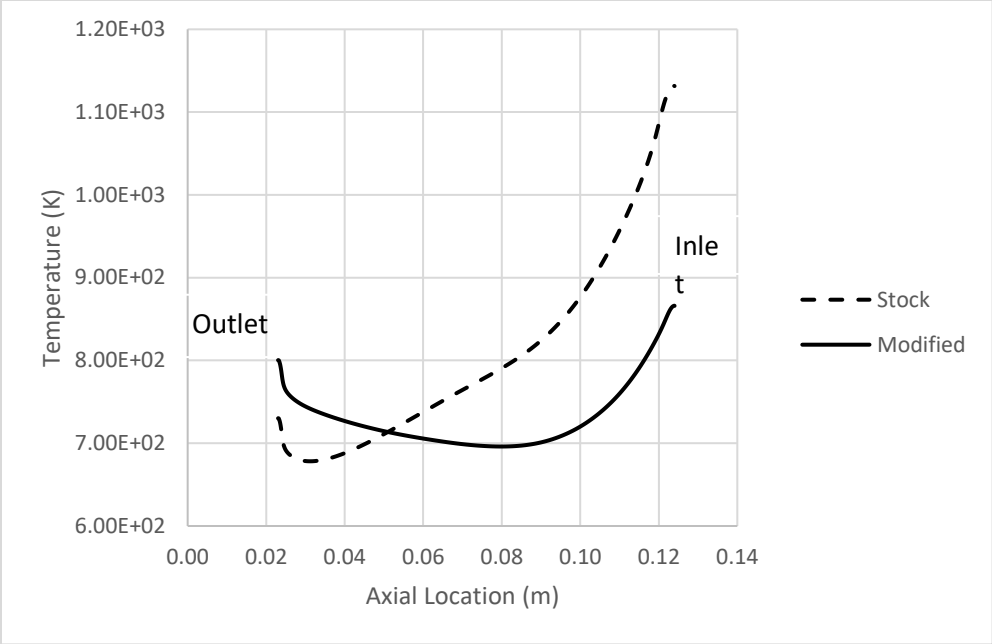

Figure 4.24 Temperature comparison of the stock and the modified geometries at the top of the armor tile

Table 5 lists the pressure drop values for both the parallel and counter-flow cases with both a uniform and tapered inner manifolds. The pressure drop values for the parallel flow configurations are generally lower than those for the counter-flow case.

Table 5 Pressure drops for 40 g/s (Re = 40,000)

Counter-Flow Case:	**Parallel Flow Case:**
Straight Tube: 39.0 kPa	Straight Tube: 24.8 kPa
Modified Tube: 39.6 kPa	Modified Tube: 27.8 kPa

The benefit of the contracting inlet manifold configuration can be explained by examining the pressure difference across the slot along the tube axis, i.e. the driving pressure difference for flow through the slot at different axial locations. To delineate the exact pressure difference across the slit, the radial pressure profiles along the vertical line of symmetry (mid-way across the slit) were extracted from the numerical results for three axial locations along the flow direction, namely 1 cm from the inlet, mid-way along the tube length, and 1 cm from the exit. The results for the geometry with straight inlet manifold are given in Figure 4.25, while those for the geometry with a contracting inlet manifold are given in Figure 4.26.

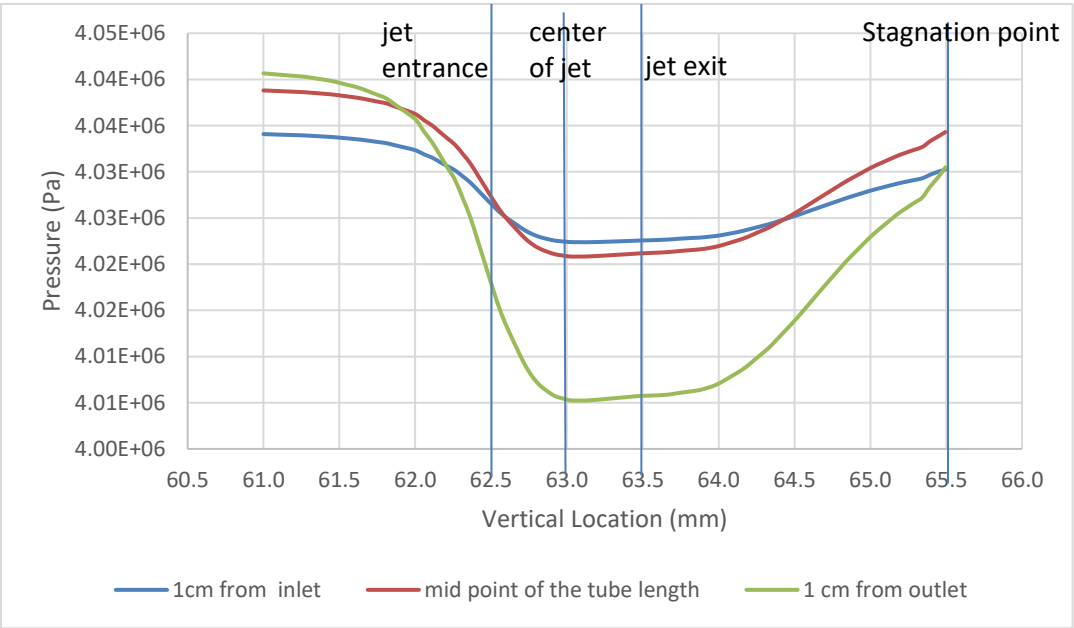

Figure 4.25 Static pressure in vertical direction on the symmetry axis with straight inlet manifold

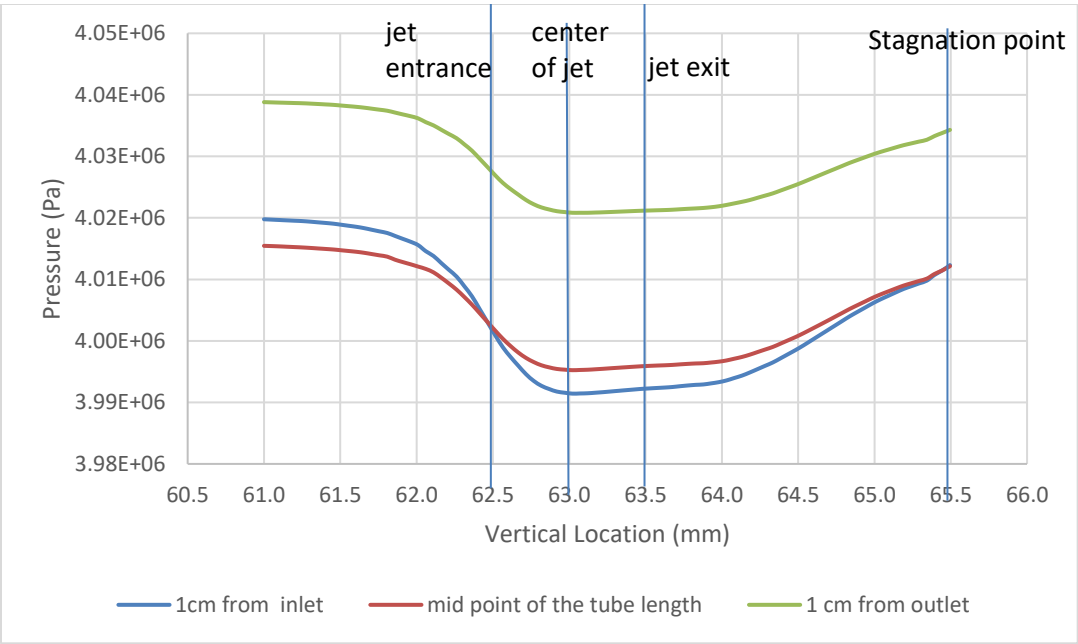

Figure 4.26 Static pressure in vertical direction on the symmetry axis with contracting inlet manifold

In Figure 4.27, the pressure difference between the inlet and exit of the slit is shown. As can be seen from Figure 4.27, in straight tube case, the pressure difference across the slit increases monotonically along the tube axis between the inlet and outlet sections. This, in turn, means that the mass flux and jet velocity increases as the flow proceeds from the inlet to the exit sections, which causes the heat transfer coefficient near the exit to be significantly higher than its value near the inlet. By tapering the inlet manifold, the pressure difference across the slit near the inlet is significantly increased, which increases the jet velocity and heat transfer coefficient, thereby reducing the axial temperature gradient caused by the stagnant zone near the inlet section

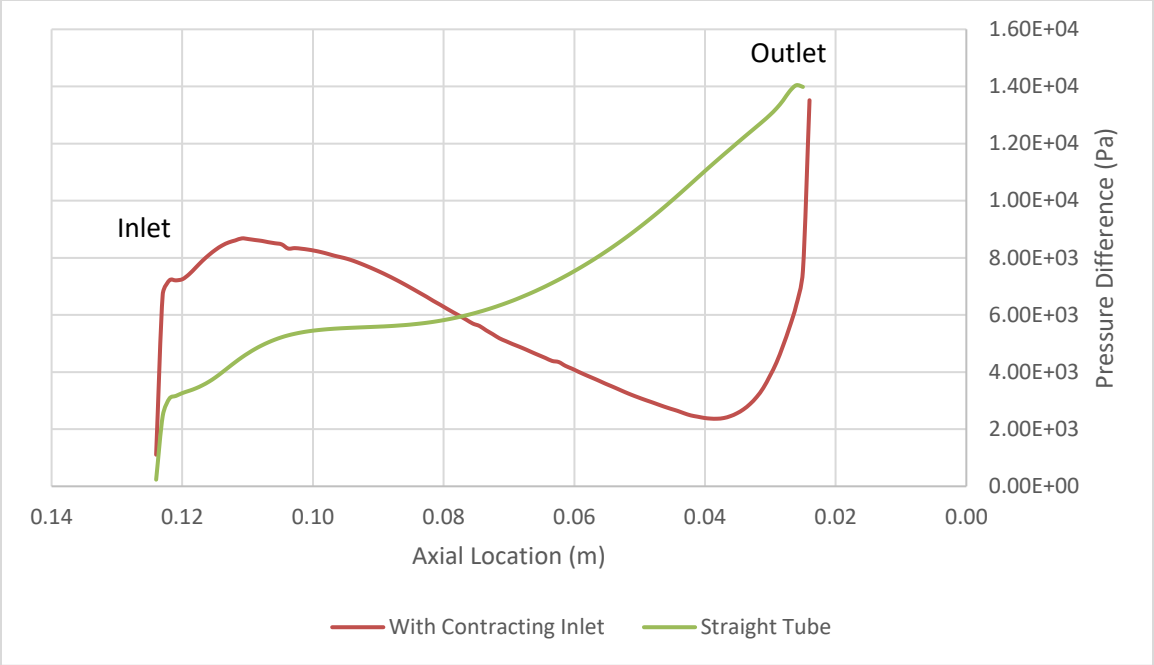

Figure 4.27 Static pressure difference between exit and entrance of the jet along the tube axis

Partial Secondary Slot at the Inlet

The main problem with the parallel flow base case is that the heat transfer coefficient rapidly decreases in the azimuthal direction near the inlet. To mitigate this problem, two "auxiliary" slots extending only a short distance along the flow direction were added near the inlet at a different angular location. The width and the length of these slots were 0.5 mm and 15 mm, respectively. Slots at two different azimuthal locations, 30 and 45 degrees from the zenith (and the main slot), were considered. The calculated performance for this modified geometry was compared to that for a manifold contraction from 12 to 4 mm. A similar concept, referred to as the "Multi-channel Concept" has been reported in the literature [58]. The optimum azimuthal location of the "auxiliary" slots is

affected by several factors. If we consider only the fluid flow, the stagnant zone expands in the azimuthal direction, and therefore, the length of the "auxiliary" slots is also a factor that affects flow. In addition, if the "auxiliary" slots are located very close to the main slot, the flow coming out of the slots may interfere with the flow of the main slot as it flows from the jet impact region azimuthally around the annulus, and may degrade the performance. On the other hand, the temperature of the cooled surface is another determinant of the optimum location of the secondary slot. The temperature of the cooled surface varies in the azimuthal direction; increasing the HTC at hotter locations results in higher total heat extraction. All in all, the optimum location of the "auxiliary" slot is a function of multiple variables and requires further study, which is not included in this thesis. Another benefit of the extra flow passage is a decrease in pressure drop. In this case the pressure drop is 10kPa less than a single slot design at 40 g/s mass flow rate (*Re* = 40,000).

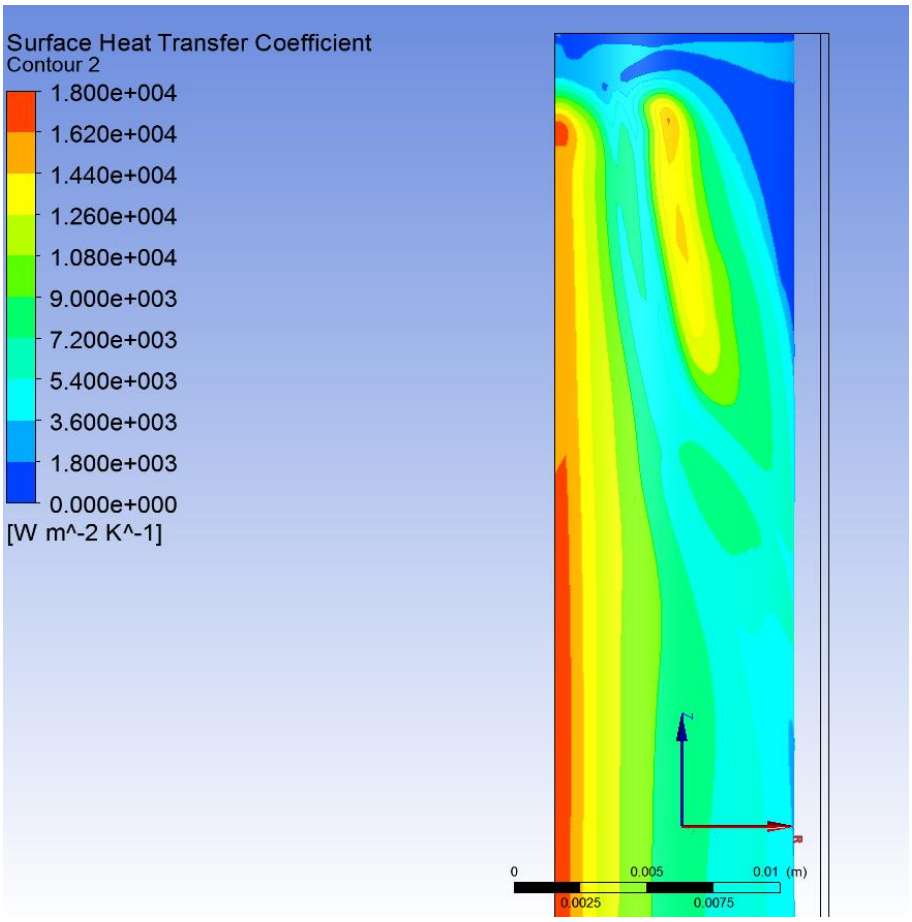

Figure 4.28 Top view of HTC contour plot with double slot

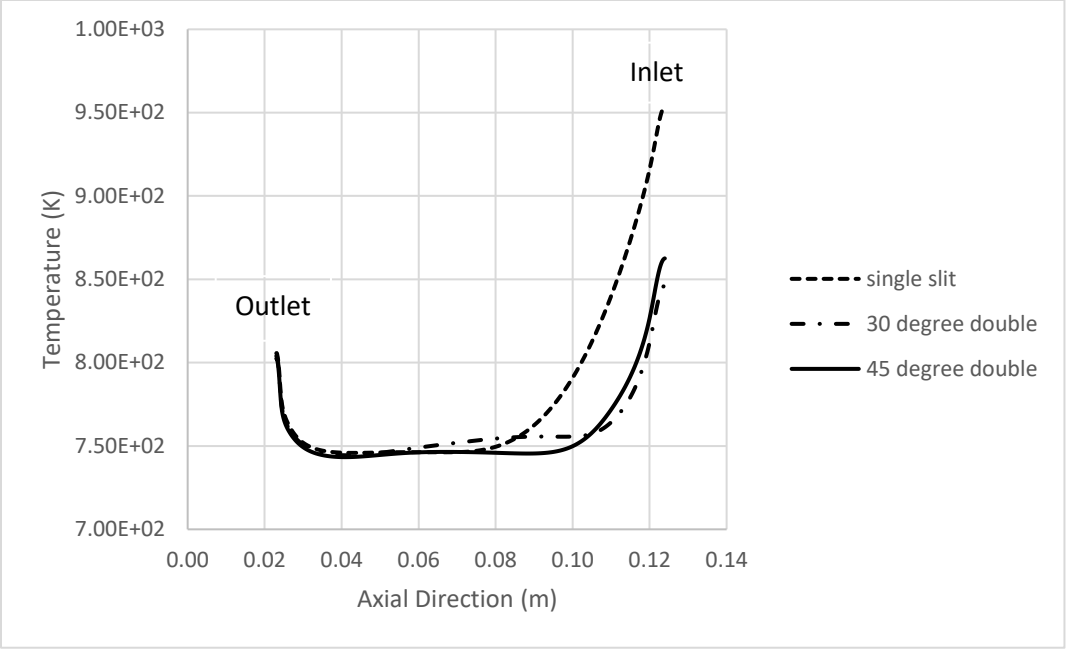

Figure 4.29 Temperature comparison of single slot and double slot cases at the top of the armor tile

Figure 4.28 shows a contour plot of the heat transfer coefficient for the case with a double slot. The temperature distributions for the case of constant manifold contraction from 12 to 4 mm with a single slot is compared against those for two cases of constant manifold contraction from 12 to 4 mm with double slots, where the secondary (short) slot is located at either 30° or 45° from the zenith. The addition of the secondary slot clearly improves the temperature distribution and diminishes the stagnant zone near the inlet. The results also indicate that the additional slot resulted in slightly better performance when it was located at 30 degree from the zenith. The maximum temperature at the inlet side on the symmetry axis of the top of the armor tile decreased by more than 100 K.

4.2.3 Effect of Inlet Manifold Contraction Ratio

In the previously described case of uniformly contracting inner manifold, the axial velocity distribution was investigated. It was found that the velocity increases near the outlet end, which means the contraction ratio may be larger than the optimum value. Hence, the effect of different inner manifold contraction ratios was evaluated. The diameter at the inlet remains unchanged (12 mm), while the diameter at the closed end was varied from 2 mm to 5 mm with 1 mm increments. The operating parameters are assumed to remain unchanged [40 g/s mass flow rate (Re = 40,000), 4 MPa outlet pressure and 5 MW/m^2 incident heat flux].

The results are shown in Figure 4.30, where the heat transfer coefficients for the various inner manifold geometries are shown. In all cases, the heat transfer coefficient is nearly uniform along the entire length. These results suggest that the temperature distributions may be equally uniform. This, however, is not the case as can be seen in Figure 4.32, which shows that the heat transfer coefficient near the inlet rapidly decreases azimuthally, while azimuthal variations in the heat transfer coefficient near the exit are significantly less pronounces because of the high axial coolant velocity in the annulus, which has a comparable effect on the HTC as the planar jet impact at that location. The distributions of temperature at the top of the armor tile along the flow direction corresponding to the different inlet manifold contraction ratios are shown in Figure 4.32.

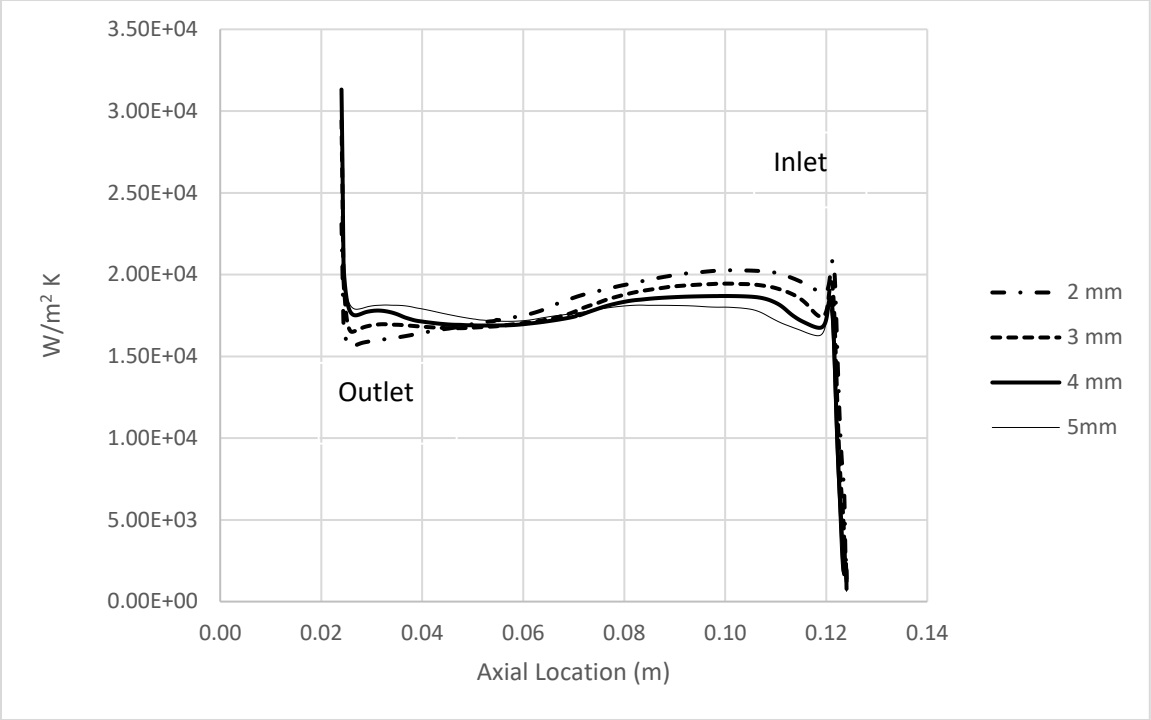

Figure 4.30 HTC Comparison of different outlet side diameters at θ=0°

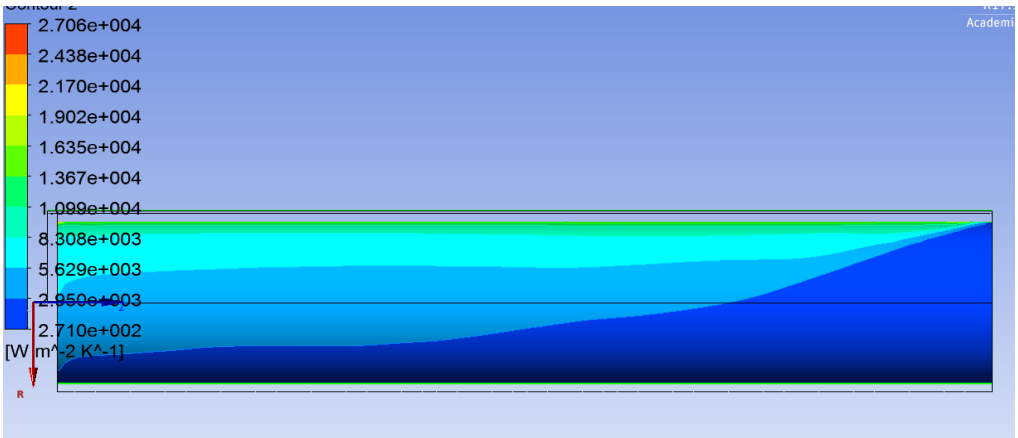

Figure 4.31 HTC contour of contraction to 4mm geometry

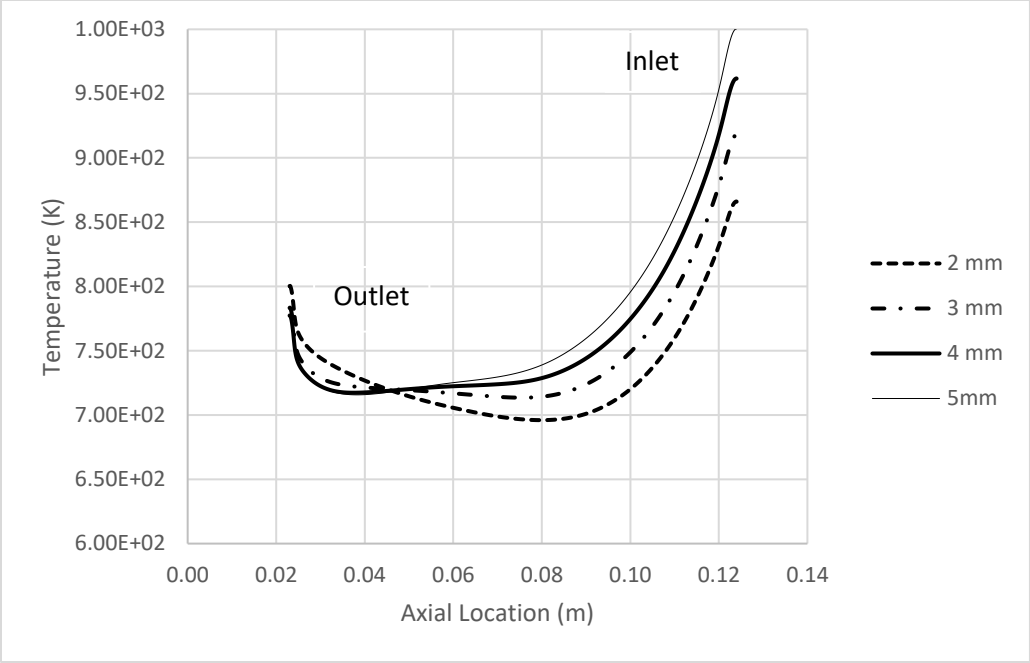

Figure 4.32 Temperature comparison of different outlet side diameters at the top of the armor tile

Table 6 provides the pressure drop values for the base parallel flow case, along with the values for cases for tapered inlet manifold with different diameters at the closed end. The highest pressure drop corresponds to the case with a tapered inlet manifold with a 2 mm diameter at the closed end (*i.e.*, the highest contraction ratio). There is a trade-off between the pressure drop before the slot (*i.e.*, in the inlet manifold) and after the slot (*i.e.*, in the annulus). Smaller diameters at the closed end of the inlet manifold lead to smaller pressure drop in the inlet manifold; however, they also cause higher pressure drop in the annulus because of higher velocities. Although the total mass flow rate that passes through the outer annulus increases in the axial direction, the cross-section stays constant in the straight tube case. This results in higher pressure drops. As can be deduced from Table 6,

increased diameter at the outlet end decreases the pressure drop; one might ask why higher diameters have not been studied. The answer is the temperature limit. Increasing the diameter near the outlet end significantly increases the temperature gradient (see Figure 4.32).

Table 6 Pressure drops of different outlet side diameters

	straight tube	5 mm	4 mm	3 mm	2 mm
Pressure Drop	24.8 kPa	21.6 kPa	22.6 kPa	24.7 kPa	27.8 kPa

4.2.4 Effect of Fully Developed Inlet Boundary Condition

In all of the previous simulations, a uniform velocity inlet boundary condition has been used. To make the simulation assumptions closer to the prototypical conditions, a fully developed turbulent flow velocity profile was also used as the inlet boundary condition (Figure 4.33). The velocity distribution at the module inlet will depend on the piping system design. Nevertheless, the change in the inlet velocity distribution should affect the development of HTC near the inlet side. The extent of that effect has been examined (see Figure 4.34 through Figure 4.37). Figure 4.34 and Figure 4.35 show contour plots for the heat transfer coefficient and velocity vectors for the base geometry using the uniform inlet velocity boundary condition. Similar results corresponding to the turbulent flow fully developed inlet velocity distributions are shown in Figure 4.36 and Figure 4.37, respectively.

As can be seen in Figure 4.34 and Figure 4.36, with a fully developed inlet velocity boundary condition, the HTC increases quickly away from the inlet location. On the other hand, in the uniform inlet velocity condition, development of the high heat transfer region is retarded. The reason for this can be seen in Figure 4.35 and Figure 4.37. In the uniform case, due to the higher axial velocity at the close proximity of slot; in other words for not fully developed flow (in terms of velocity), the velocity vectors are more skewed towards the axial flow direction, which retards the development of the thermal boundary layer. Despite this difference between the two cases, the ultimate effect on the temperature distributions is negligible (see Figure 4.38). The difference in the calculated temperatures at the top of the tile are only about 2 K, except near the inlet where a difference of about 20 K is observed. The results indicate that use of the uniform velocity boundary condition is conservative, *i.e.* it "overestimates" the calculated temperatures.

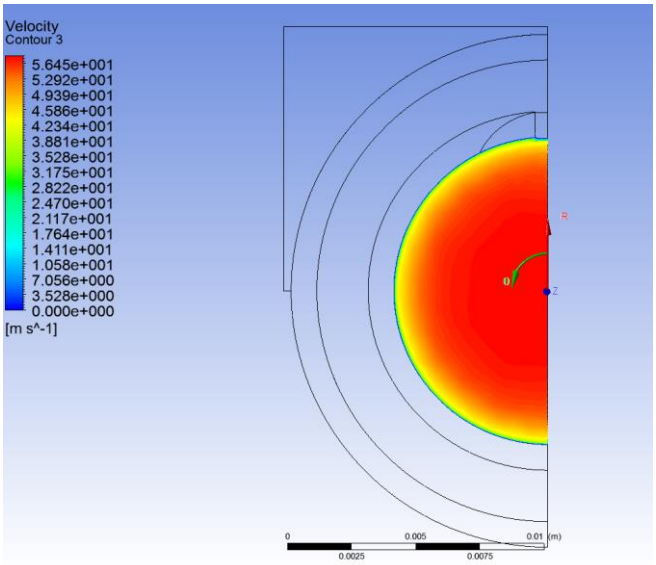

Figure 4.33 Fully developed inlet velocity profile

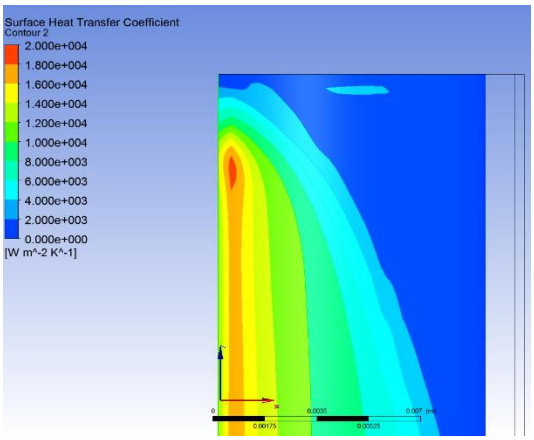

Figure 4.34 Top View of Uniform Inlet B.C

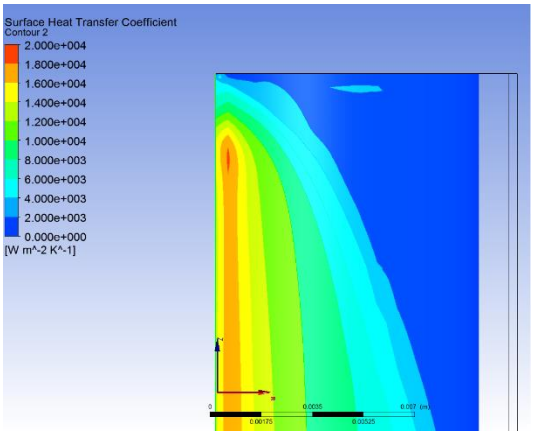

Figure 4.36 Top View of Fully Developed Inlet B.C

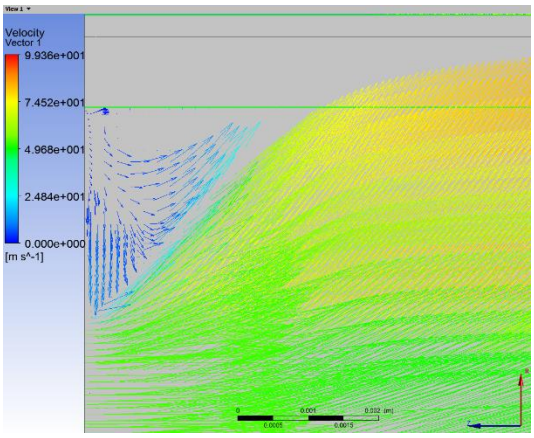

Figure 4.35 Velocity Vectors at the Slot for Uniform Inlet B.C

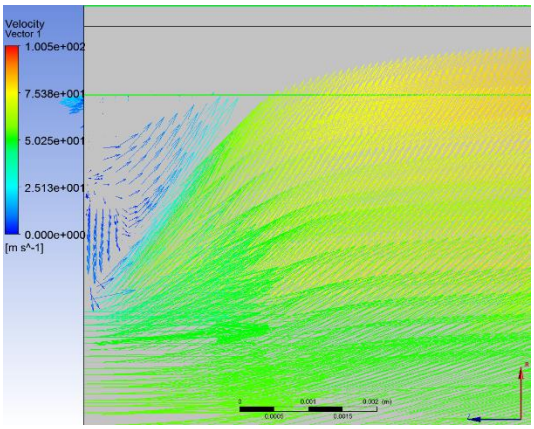

Figure 4.37 Velocity Vectors at the Slot for Fully Developed Inlet B.C

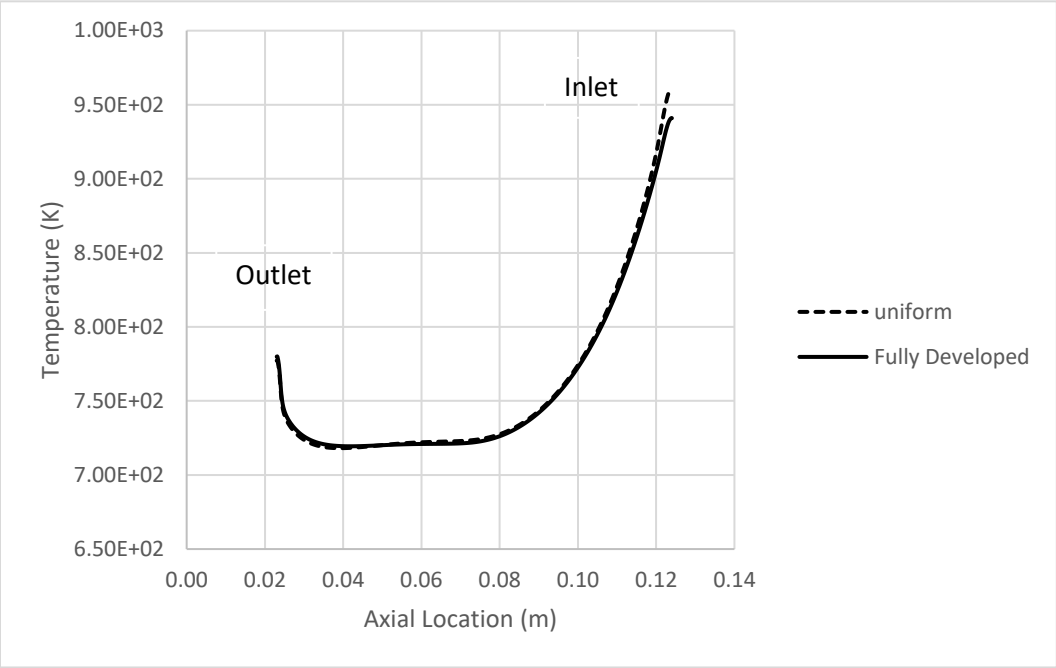

Figure 4.38 Temperature comparison of uniform and fully developed velocity inlet B.Cs at the top of the armor tile

4.2.5 Non-Uniform Heating

Based on initial test results of proto-MPEX at ORNL, the heat flux incident on the target plate will likely be highly non-uniform. The heat flux pattern depends on the plasma heating power and the contribution of different heating sources [23]. A typical helicon-mode temperature distribution is given in Figure 4.39. Most of the previous divertor designs assume that the heat flux will be uniform over the entire heated surface. Localized high temperatures may cause mal-distribution of the gas coolant by increasing its viscosity and more importantly by decreasing the local density of the gas. Specifically, the designs where the cold side coolant is in direct contact with the heated surface, and the designs with refractory materials such as porous refractory material divertors, are more vulnerable

to showing signs of mal-distribution [28]. To determine if this particular design with rectangular jet is prone to demonstrate any change in helium flow with increasing heat flux, different incident heat fluxes ranging from 1 MW/m^2 to 10 MW/m^2 were evaluated.

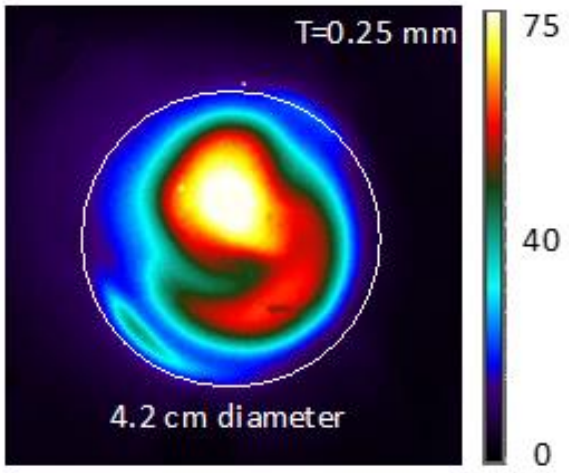

Figure 4.39 A typical helicon-mode temperature pattern for a 0.25 mm thick target plate [23].

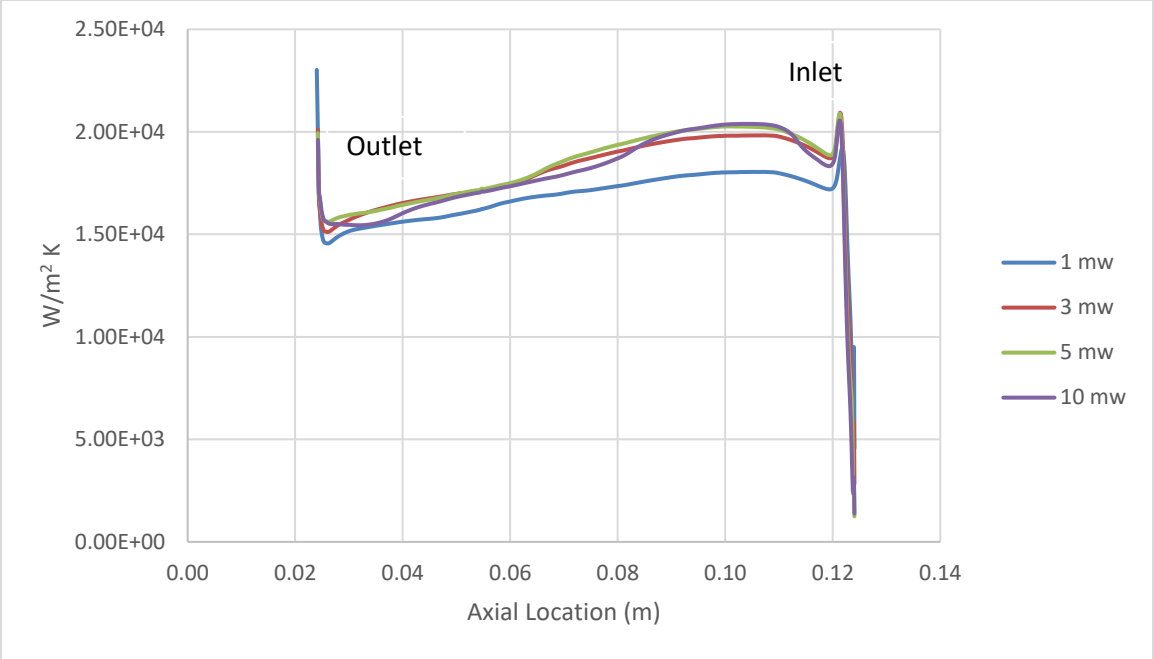

Figure 4.40 Comparison of HTC under different heat fluxes at θ=0°

Except for the 1 MW/m^2 case, the other three cases show similar pattern for HTC with variations of a few percent at most. The reason why the 1 MW/m^2 case is so different may be related to how ANSYS Fluent® calculates HTC. It uses a reference temperature to calculate the heat transfer coefficient by rearranging $q"_w = h_c(T_0 - T_w)$, where T_0 is the specified outside or external boundary temperature and T_w is the temperature at the wall [45]. Different heat fluxes result in different wall temperatures, and therefore slightly different heat transfer coefficients.

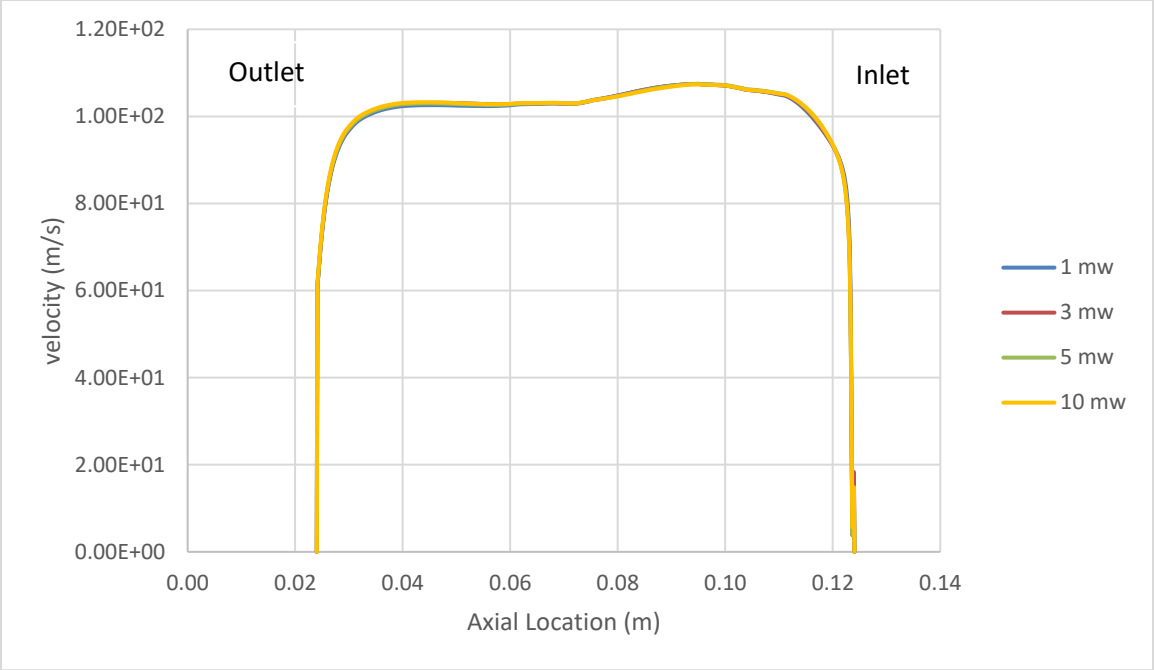

Figure 4.41 Comparison of jet velocity for different heat fluxes

To assess whether there is any difference in flow distribution under different heat fluxes at 40 g/s mass flow rate (*Re* = 40,000) and 4 MPa outlet pressure, the jet cross-section was divided into 4 equal rectangular sections and total mass flow rates were calculated for each different case. The first section was at the inlet side, which is on the left hand side in Figure 4.42 and the fourth section is at the outlet side, which is on the right hand side in Figure 4.42.

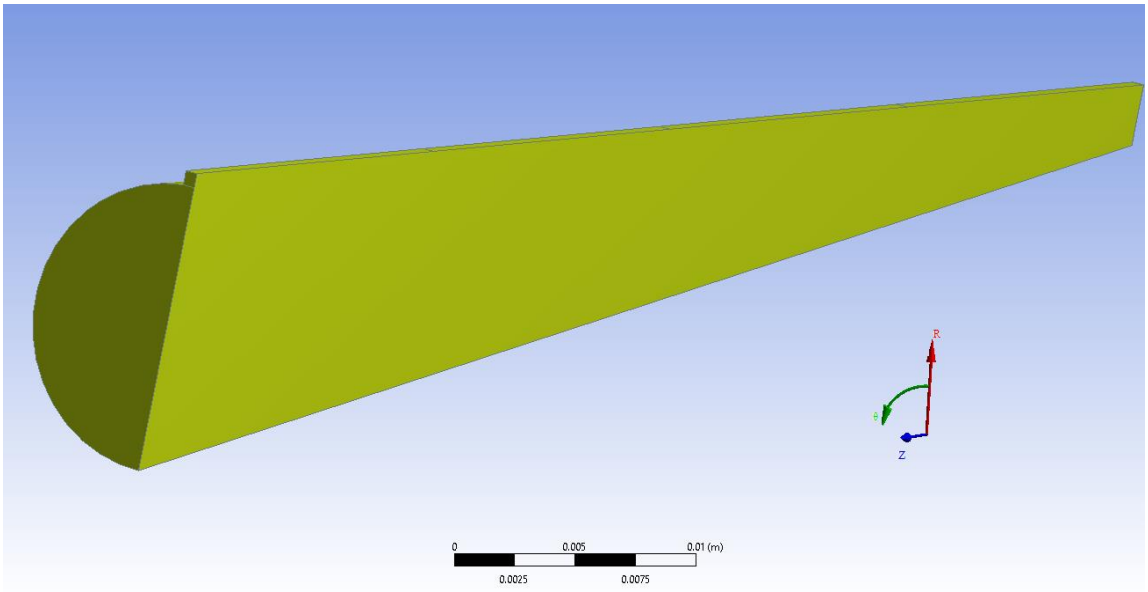

Figure 4.42 Location of the Sections

As shown in Table 7, no significant difference was observed between the two extreme cases, zero and 10 MW/m^2. Since the heat fluxes were uniform, they did not cause any mal-distribution in the flow.

Table 7 Comparison of mass flow rates in each section

	grams/second			
Heat Flux / Mass Flow	first region	second region	third region	fourth region
1 MW/m^2	5.6097	5.6232	4.6695	4.0520
3 MW/m^2	5.6071	5.6189	4.6682	4.0601
5 MW/m^2	5.6046	5.6151	4.6674	4.0675
10 MW/m^2	5.6032	5.6013	4.6672	4.0830
No Heat	5.6050	5.6286	4.6708	4.0500
Max Difference	0.12%	0.49%	0.08%	0.81%

A study similar to the previous one was conducted to measure the effect of axially non-uniform heat flux. As given in Figure 4.43, the top of the armor tile was divided into 4 equal pieces and heat flux was applied to only one of the pieces at 40 g/s mass flow rate (*Re* = 40,000) and 4 MPa outlet pressure to check whether helium will diverge from the heated segment or not. In contrast to the last case, the mass flow rate was calculated at the side surface of the jet instead of at the slot in order to include helium, if any, that changes its section after impingement.

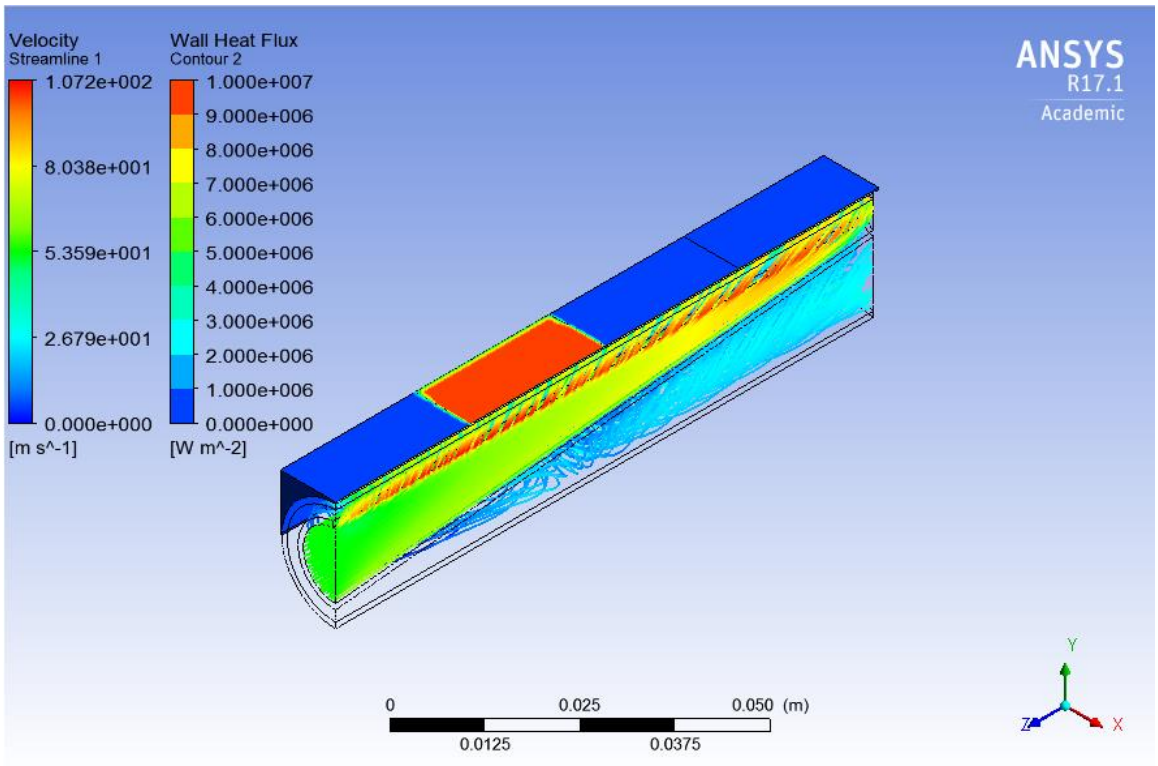

Figure 4.43 Illustration of segments and heat flux

Table 8 Comparison of mass flow rates in each section (only the second section is heated)

	grams/second			
Heat Flux / Mass Flow	first region	second region	third region	fourth region
No Heat	5.1355	5.5421	4.5673	4.3090
$5\ MW/m^2$	5.1325	5.5342	4.5598	4.3090
$10\ MW/m^2$	5.1344	5.5228	4.5516	4.3115
Max Difference	0.06%	0.35%	0.34%	0.06%

As is clear in Table 8, the differences between mass flow rates for different heat fluxes are negligible. Note that due to the velocity profile along the axis, it is not expected for each region to have the same mass flow rate.

Secondly, the same conditions were applied to only the first section instead of the second section. Because there was a stagnant zone at the inlet side, the impact of non-uniform heating might be more pronounced.

Table 9 Comparison of mass flow rates in each section (only the first section is heated)

	grams/second			
Heat Flux / Mass Flow	first region	second region	third region	fourth region
No Heat	5.1355	5.5421	4.5673	4.3090
5 MW/m^2	5.1266	5.5235	4.5587	4.3089
10 MW/m^2	5.1192	5.5096	4.5527	4.3036
Max Difference	0.32%	0.59%	0.32%	0.13%

Although the maximum differences are slightly higher than those for the previous case; however, they are still less than 1% and are thus negligible. This is an expected result based on the behavior of gases at higher temperatures. The density of the gas decreases and viscosity of the gas increases with the increased temperature, and this causes more mal-distribution

In another case, the incident heat flux was applied to only one side of the model and the flow distribution of helium was monitored. One might expect a divergence of coolant from the heated side due to density change and corresponding increase in pressure drop.

Due to the non-uniform heating from one side, a half-model cannot be used to investigate the flow distribution in this case. Because of computational limitations, it was necessary to keep the element count lower, so only the fluid side is modeled, and the worst

case scenario, melting point of CuCrZr, is set as the temperature boundary condition from one side as can be seen in Figure 4.44.

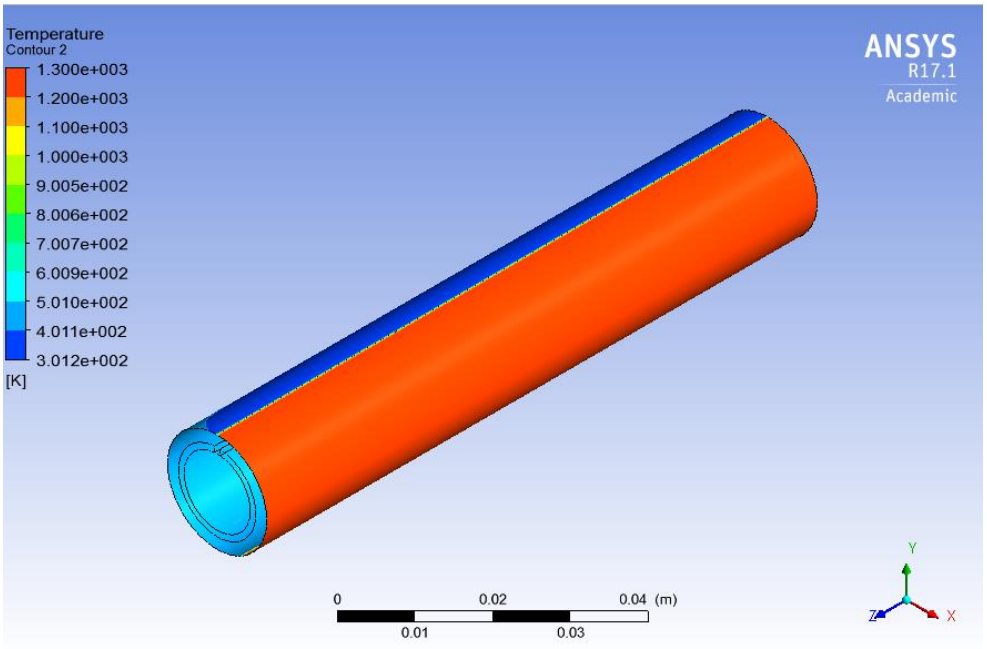

Figure 4.44 Illustration of only fluid domain and temperature boundary condition

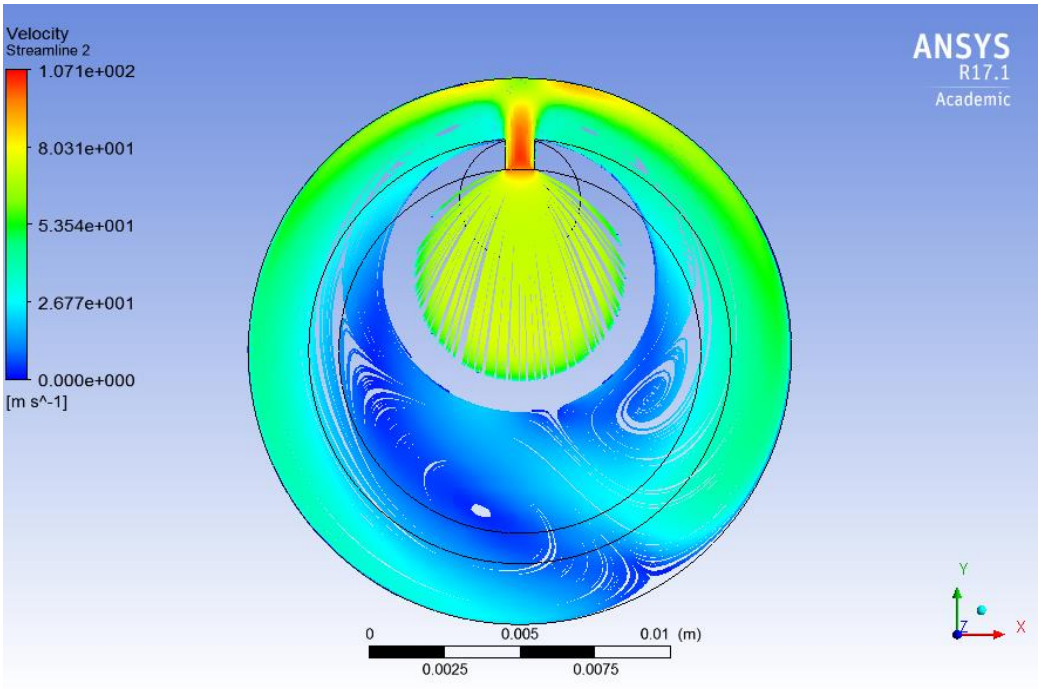

Figure 4.45 Surface streamlines on the mid-section

In Figure 4.45, streamlines show that the flow is not symmetrical. Unexpectedly, mass flow measurements from both the slot and the side of the jet show that although the difference is limited, the heated side received more mass flow (Table 10).

Table 10 Comparison of mass flow rate for right and left sides for 40 g/s

	kilograms/second	
Temperature / Mass Flow	Left Side	Right Side(heated)
No Heat	1.8471E-02	1.8292E-02
1300 K	1.8039E-02	1.8718E-02
Max Difference	2.34%	2.28%

Table 11 Comparison of mass flow rate for right and left sides for 20 g/s

	kilograms/second	
Temperature / Mass Flow	Left Side	Right Side(heated)
No Heat	9.2079E-03	9.2167E-03
1300 K	8.9381E-03	9.4504E-03
Max Difference	2.93%	2.47%

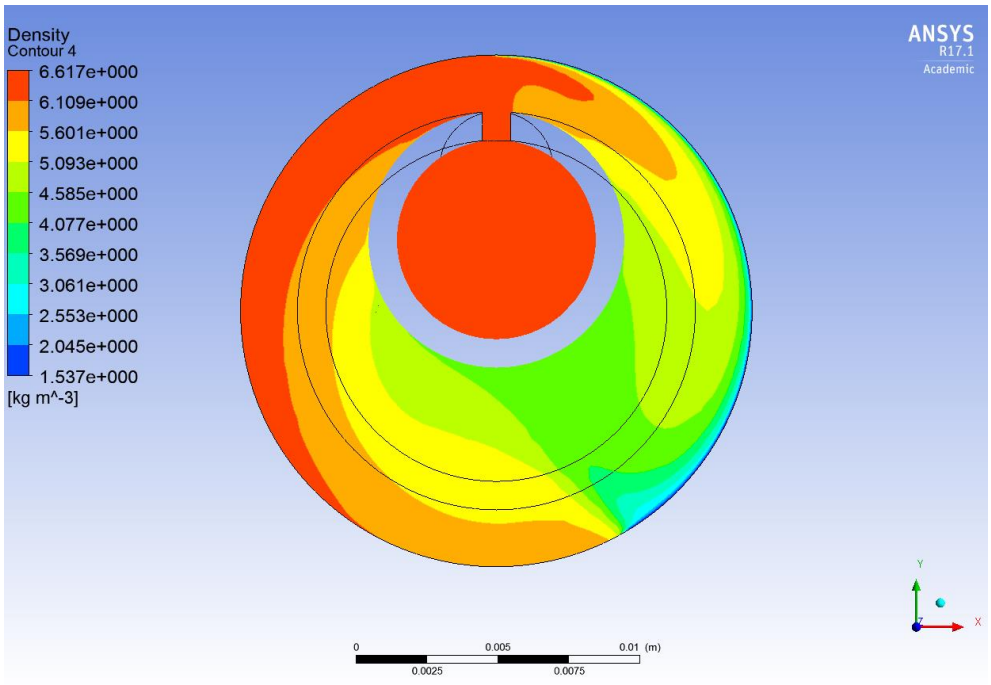

Figure 4.46 Density contours on the mid-section

The density contours in Figure 4.46 reflect the non-uniform heating pattern, with a much lower density on the heated side compared with the unheated side.

The mal-distribution in the flow might be more apparent in the boundary layer. A 0.05x50 mm cross-section perpendicular to the jet direction was selected for mass flow calculations (0.05 mm represents the thermal boundary layer thickness based on $\frac{T_s - T}{T_s - T_\infty} = 0.9$ where T_s is the cooled surface temperature and T_∞ is the inlet temperature of helium).

The mass flow rate through the left side (unheated) is 0.764909 g/s and that through the right side (heated) is 0.415305 g/s; the deviation from the mean is around 30%. This difference suggests that the mass flow that participates in heat transfer is significantly less for the heated side than for the non-heated side.

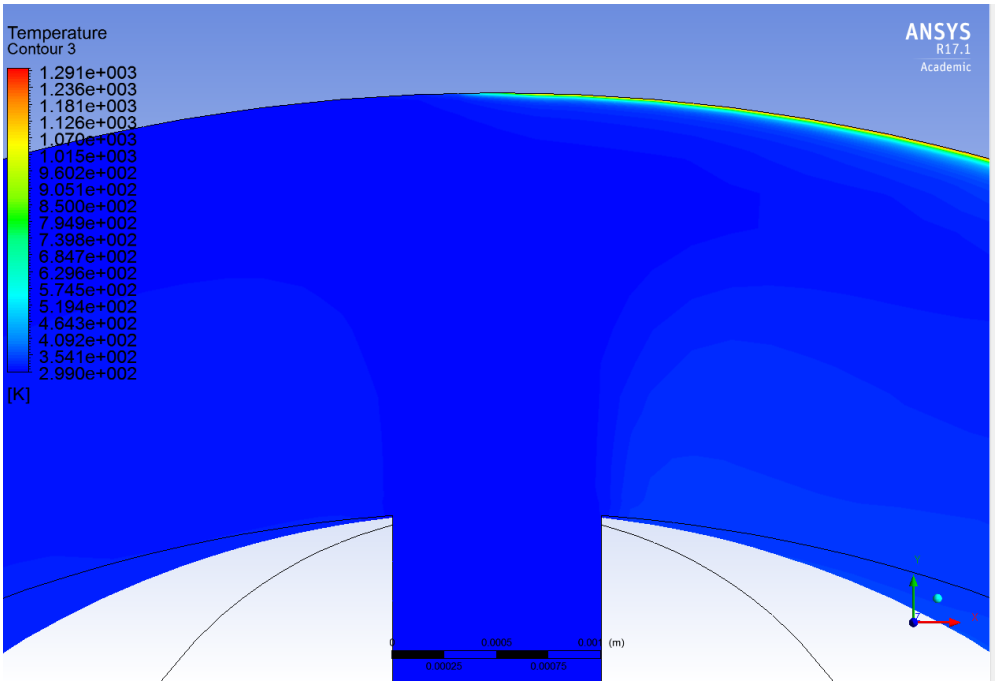

Figure 4.47 Development of thermal boundary layer for heated from one side case

Figure 4.47 depicts the thickness of the thermal boundary layer and its dimension relative to the passage width. Since the Prandtl number of helium is at the order of 1, the hydrodynamic boundary layer thickness is also close to that of the thermal boundary layer.

Additional analyses were performed to examine the effect of non-uniform incident heat flux on the armor tile on both flow uniformity and peak surface temperature. The analyses were performed using a full 3D geometry because of the assumed asymmetric incident heat flux. A slightly less dense mesh has been used due to computational limitations. Two non-uniform heat flux cases where heat fluxes of either $10MW/m^2$ or $12MW/m^2$ are applied to only one side (right hand side) of the armor tile starting from the corresponding location of the end-point of the slot on the armor tile (Figure 4.48) with zero heat flux on the remainder of the tile have been modeled. The corresponding average heat flux values over the entire tile surface are 4.75 and 5.71 MW/m^2, respectively. The calculations were performed for a mass flow rate of 40 g/s (*Re=40,000*). The non-uniform incident heat flux will cause the coolant flowing in the right direction after issuing from the slot (see Figure 4.49) to be significantly hotter than the coolant flowing in the opposite direction. The higher coolant temperature will increase its viscosity and reduce its density so that the flow rate through the right side of the annulus may be less than half of the flow rate issuing from the jet.

Table 12 compares the mass flow rates for the right (heated) and left (unheated) sides of the annulus for the two cases analyzed. The sum of the two mass flow rates is less than 40 g/s since part of the coolant flow near the exit section directly exits the module after issuing from the slot without impinging on the inner surface of the outer tube. The results shown in Table 12 are surprising, inasmuch as the flow rate through the right

(heated) side of the annulus is slightly higher than that on the unheated side. This may be caused by a higher bypass fraction on the unheated side (i.e. direct exit from the slot to the discharge plane without impingement on the inner surface of the outer tube). A similar result was obtained in the previous cases constant surface temperature boundary condition case (Table 10 and Table 11). Nevertheless, the difference in flow rate between the heated and unheated sides is relatively small, namely 1.09% and 1.42% for the 10MW/m^2 and 12MW/m^2, respectively. Hence, the impact of non-uniformity in the incident heat flux on the flow distribution will likely be insignificant.

Of more concern is the effect of non-uniform heat flux on the calculated peak surface temperature. Here, the calculated maximum armor surface temperatures for the two non-symmetric heat flux cases described above are compared against the corresponding values for cases with uniform heat flux at the same average heat flux values, namely 4.75 and 5.71 MW/m^2 for the 10MW/m^2 and 12MW/m^2, respectively. The same 3D mesh geometry is used for both the uniform and non-uniform heat flux cases. The results are summarized in Table 13. For the non-uniform 12MW/m^2 heat flux case, the peak surface temperature (1301 K) is nearly equal to the melting point of the material, while the maximum surface temperature for the corresponding case with a uniform heat flux at the same average value (5.71 MW/m^2) is only 975 K. Similarly, for the non-uniform 10MW/m^2 heat flux case, the peak surface temperature is 1130 K, versus 854 K for the corresponding case with a uniform heat flux at the same average value (4.75 MW/m^2). Comparing the surface temperatures for the non-uniform heat flux cases against those for uniform heat flux cases with the same average heat flux is appropriate, inasmuch as cases with uniform heat fluxes of 10MW/m^2 and 12MW/m^2 result in excessively high maximum surface

temperatures of 1551 and 1872 K, respectively. The above results indicate that the primary concern in cases with non-uniform heating is the increase in maximum temperature (i.e. reduction in mechanical strength) rather than flow mal-distribution. The above simulations also indicate that this particular design is not prone to coolant mal-distribution or flow instability at least for the non-uniform heat flux cases considered here.

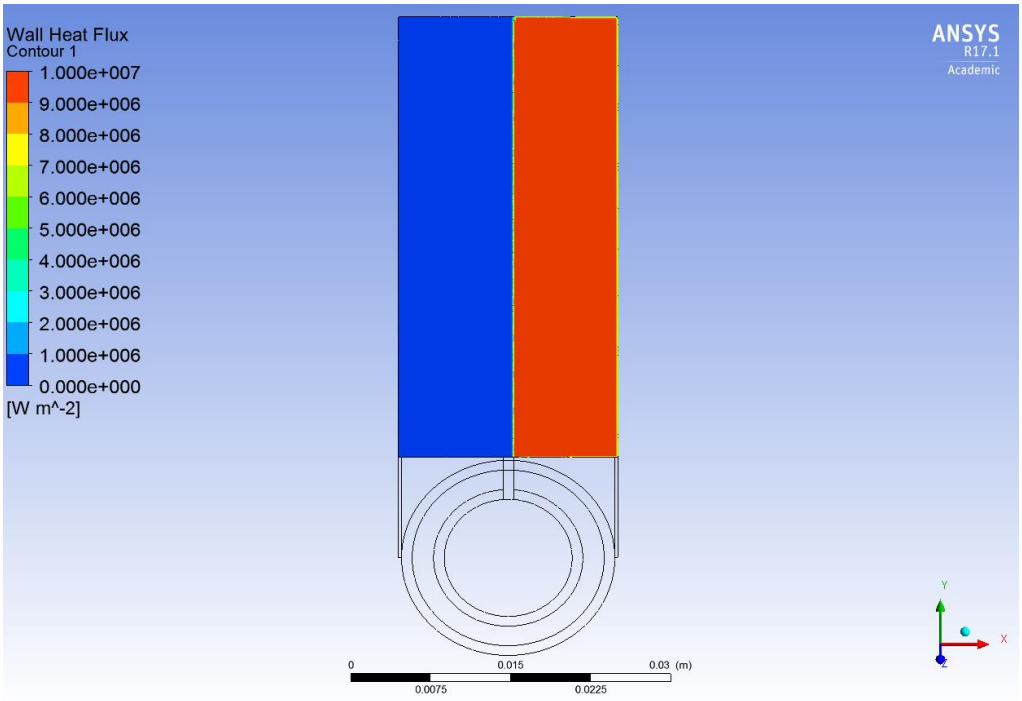

Figure 4.48 Non-uniform heat flux on the top of the armor tile

Table 12 Comparison of mass flow rate for right and left sides with heat flux applied to the top of the armor tile

	kilograms/second		
Temperature / Mass Flow	Left Side	Right Side	*% Difference*
10 MW/m^2 non-uniform(right side heated)	1.9566E-02	1.9782E-02	*1.09%*
12 MW/m^2 non-uniform(right side heated)	1.9528E-02	1.9810E-02	*1.42%*

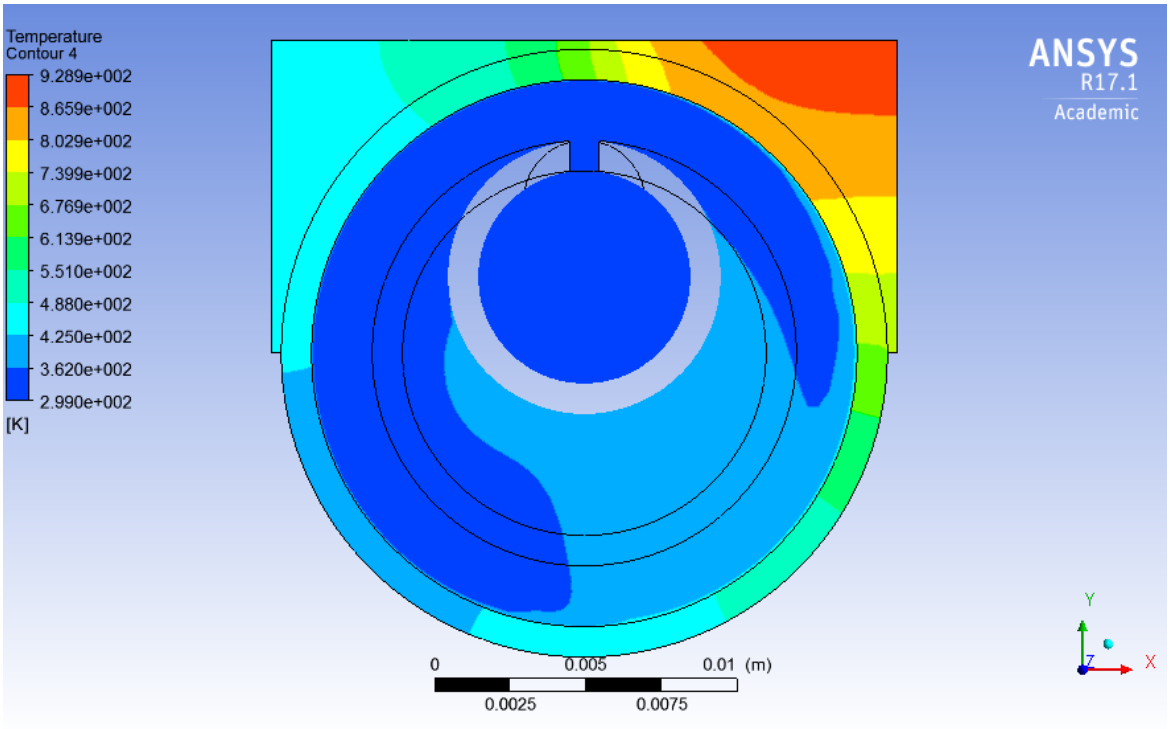

Figure 4.49 Temperature contour plot at the mid-section of the tube

Table 13 The maximum surface temperature for different heat fluxes

one side(non-uniform)	Max. Surface Temperature	All over the surface (uniform)	Max. Surface Temperature
12 MW/m^2	1301 K	5.71 MW/m^2	975 K
10 MW/m^2	1130 K	4.75 MW/m^4	854 K
		12 MW/m^2	1872 K
		10 MW/m^2	1551 K

4.2.6 Effect of Inclined Inlet

In the base geometry, Helium enters the system in the horizontal direction and then turns to the vertical direction. Due to inertia, it takes some time to change its trajectory and thus the stagnant zone is large. Providing inclined flow at the inlet may decrease the area of the stagnant zone.

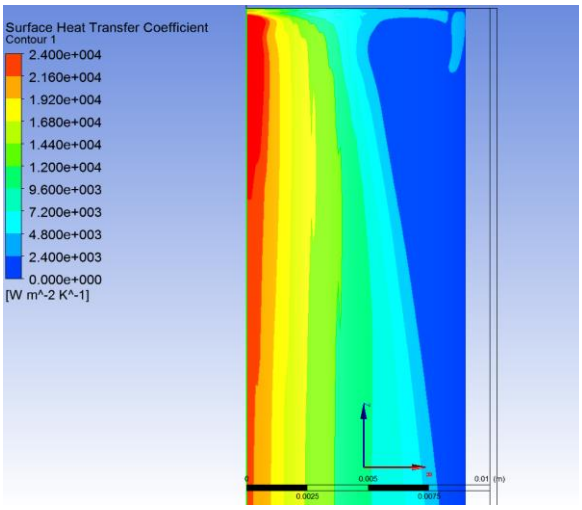

Figure 4.50 Top view of HTC contour plot with 45 degree inclined inlet

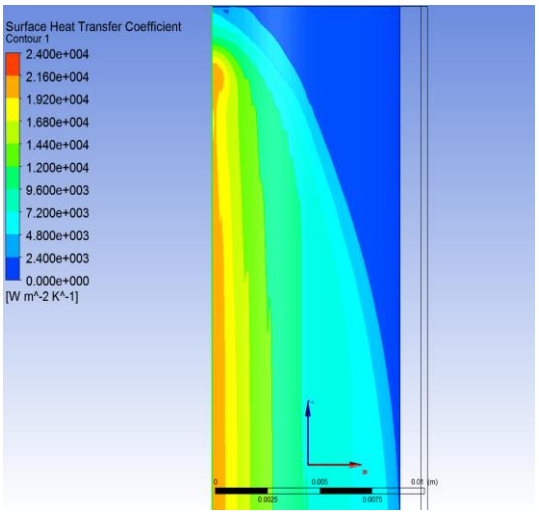

Figure 4.51 Top view of HTC contour plot with horizontal inlet

In Figure 4.50, with 45 degrees inclined inlet, the heat transfer coefficient is much higher at the inlet and it covers a larger area starting from very near the inlet.

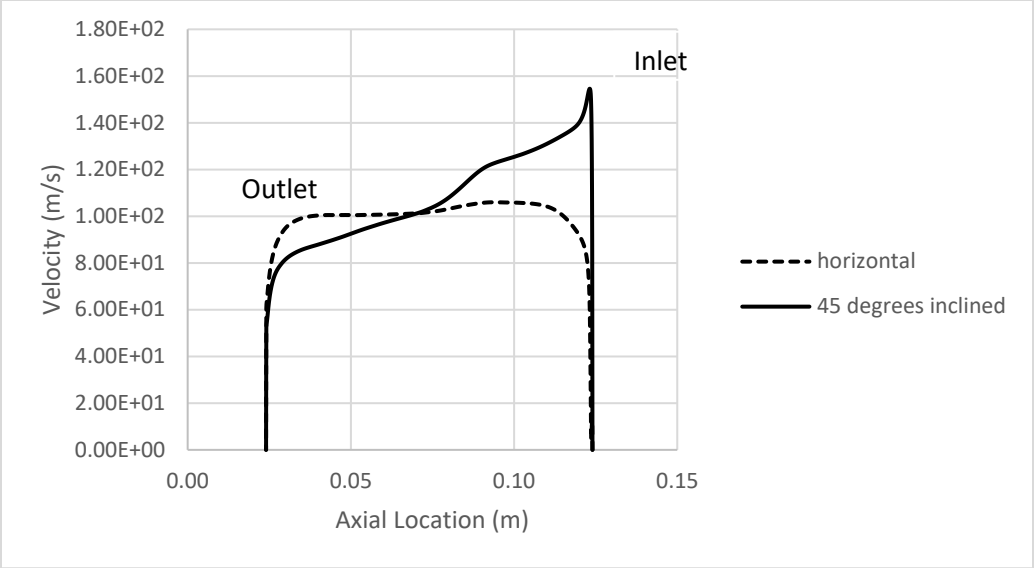

Figure 4.52 Comparison of jet velocity for horizontal and inclined inlet

The velocity profile along the Z-axis in Figure 4.52 explains the high HTC at the inlet. The velocity varies by a factor of two between the outlet and the inlet sides.

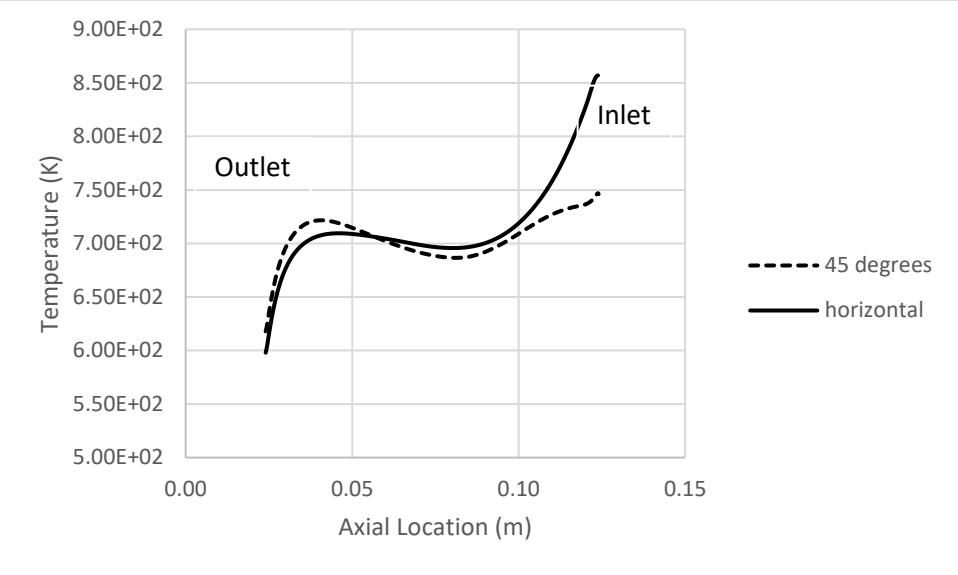

Figure 4.53 Temperature comparison of horizontal and inclined inlet cases at the top of the armor tile

Having higher heat transfer at the problematic zone, the inlet side, decreased the peak temperature at the inlet side on the symmetry axis of the top of the armor tile by about 100 K. The maximum temperature at the outlet side increased a few degrees; however, the highest temperature is still at the inlet side. On the other hand, due to more non-uniform velocity distribution along the slot, pressure drop increases. In this case, the pressure drop is 8 kPa less than horizontal inlet condition at 40 g/s mass flow rate (*Re* = 40,000).

4.2.7 Effect of Slot Width

Different slot widths between 0.5 mm and 1 mm have been investigated for the same conditions; 40 g/s mass flow rate (*Re* = 40,000), 4 MPa outlet pressure and 5MW/m^2 heat flux. Unsurprisingly, with decreasing slot width, jet velocity and HTC increased and

eventually overall temperatures have decreased. However, remarkably, the change in the inlet side temperature is twice that in the outlet side temperature.

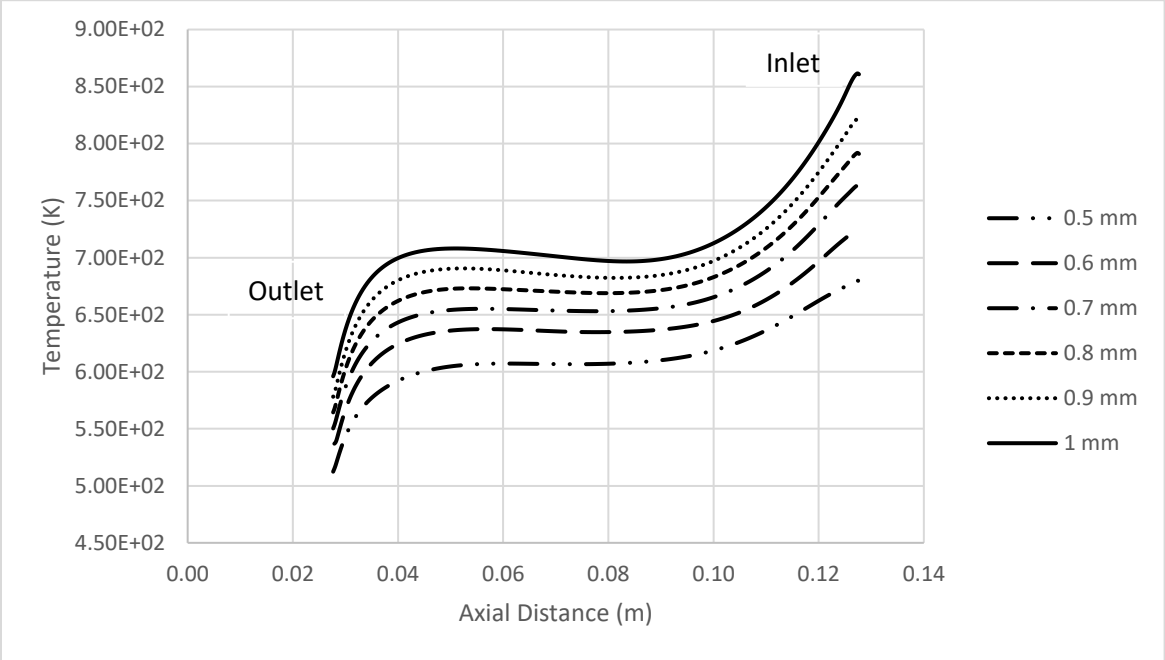

Figure 4.54 Temperature comparison of different slot widths at the top of the armor tile

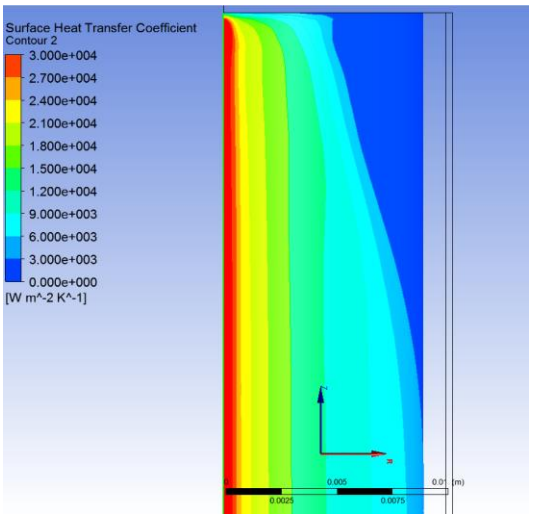

Figure 4.55 Top view of HTC contour plot with 0.5 mm slot

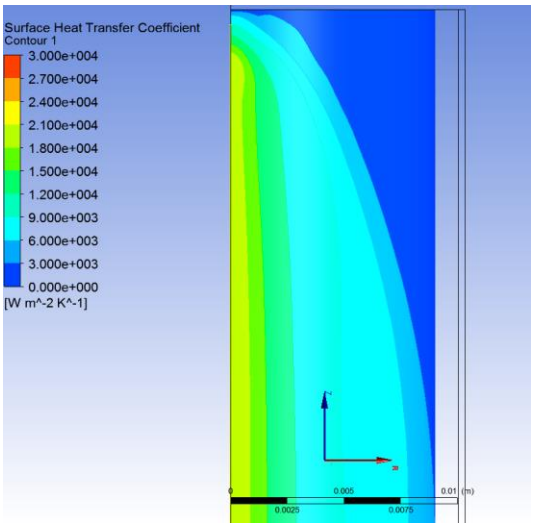

Figure 4.56 Top view of HTC contour plot with 1.0 mm slot

When Figure 4.55 and Figure 4.56 are compared, it can be seen that flow develops more rapidly in 0.5 mm slot width case. This suggests that the ratio between the horizontal and vertical velocity components of helium flow has an important role in the uniformity of flow distribution, particularly at the inlet, where flow needs to make a 90 degree turn in the vertical direction after entering the system. This is basically the result of vector components of the flow just after the slot passage. If we consider a fluid particle from a Lagrangian perspective, the vertical component of the velocity, namely the jet velocity, determines the time when the particle impinges on the cooled surface, and the horizontal velocity determines the location of the impingement. Therefore, increasing the ratio of jet velocity to horizontal velocity leads to a smaller stagnant zone.

Obviously, contraction of slot width comes with a pressure drop disadvantage. Decreasing the slot width from 1.0 mm to 0.5 mm almost triples the total pressure drop as can be seen in Figure 4.57.

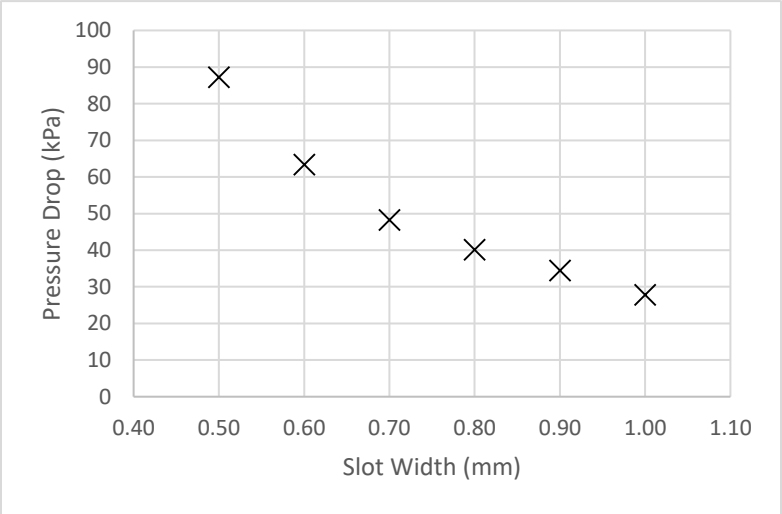

Figure 4.57 Comparison of pressure drop for different slot widths

4.2.8 Effect of Bridge

This study does not involve a mechanical analysis of the divertor. However, it is unlikely for the jet consisting of single continuous slot to maintain a constant width because of structural integrity. Under pressure, it might be deformed substantially enough to have deteriorated heat transfer. Since the inner tube is fixed at both ends, a single bridge in the middle is expected to be sufficient to maintain a consistent width. To investigate the possible implications of the flow disruption at the jet, a 1 mm long bridge was modeled.

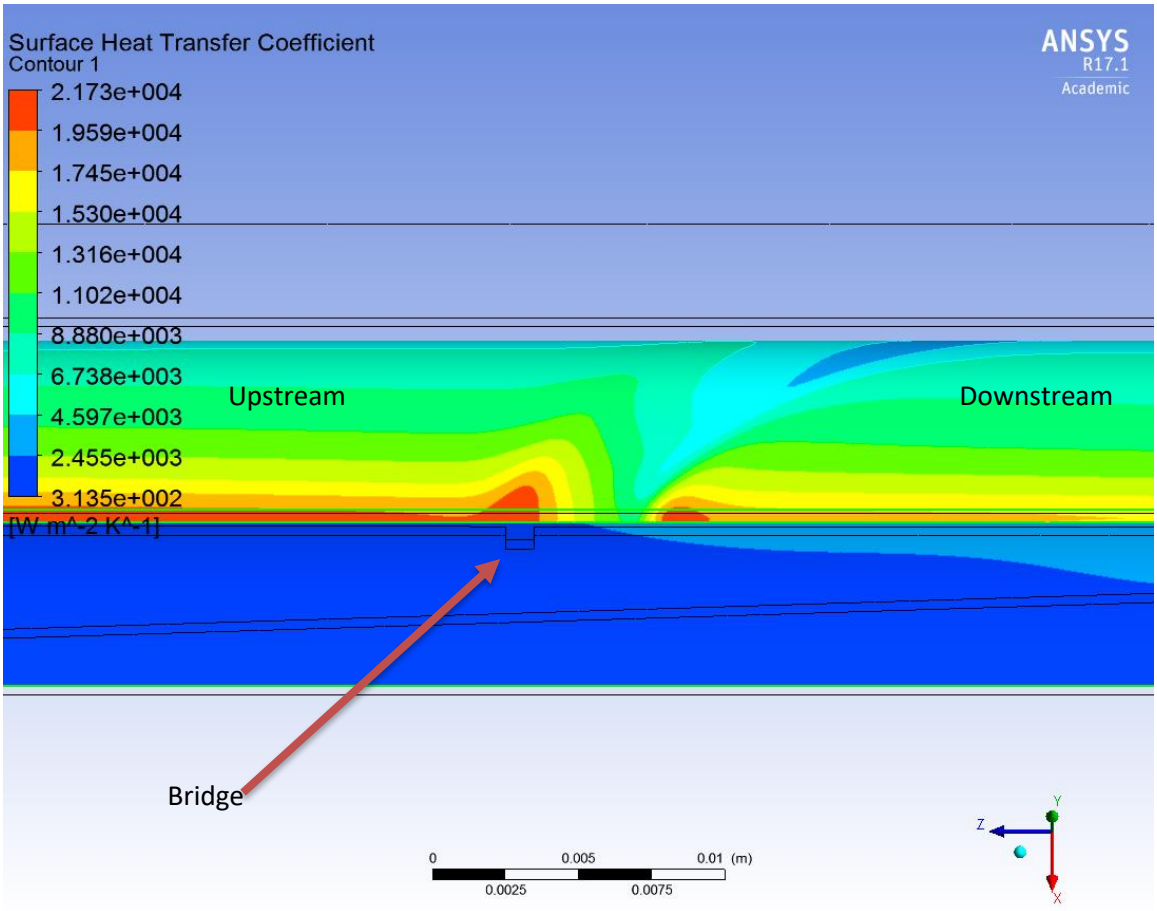

Figure 4.58 HTC contours at the bridge

In Figure 4.58, the highest heat transfer coefficient occurs at the location just above the bridge, and the lowest occurs a few millimeters after it. The bridge acts as a second inlet, and another stagnant zone develops downstream of it.

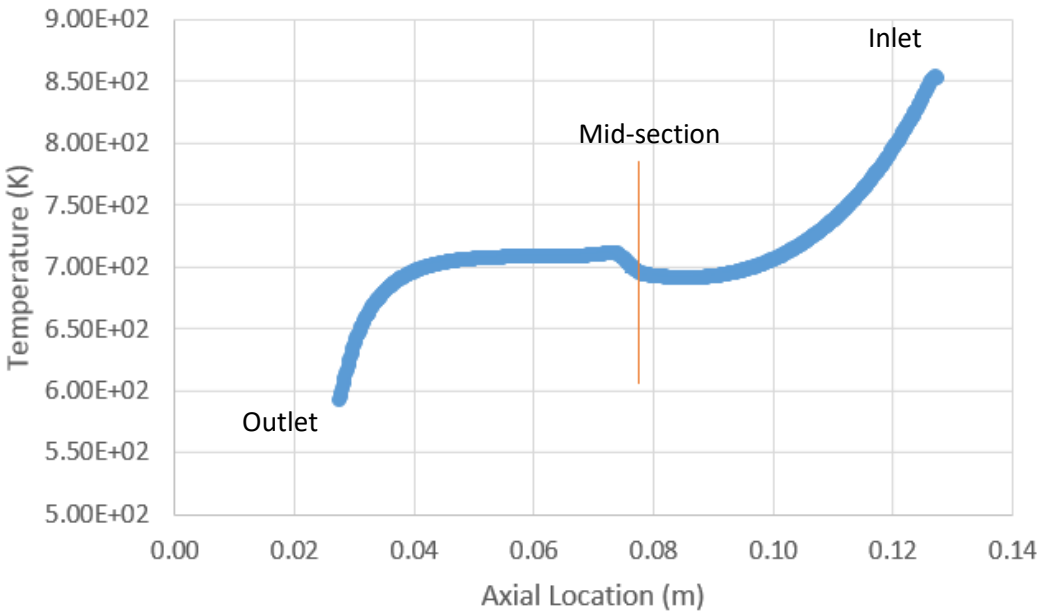

Figure 4.59 Temperature distribution at the top of armor tile

As can be seen in Figure 4.59, in parallel to the HTC pattern, temperature reaches its local peak not exactly at the mid-section but a few millimeters beyond it. This is the result of the horizontal component of the flow.

In Figure 4.60, the wake region of the bridge causes the temperature level to stay elevated after the local maximum point for a while. However, this increase is much less than that at inlet.

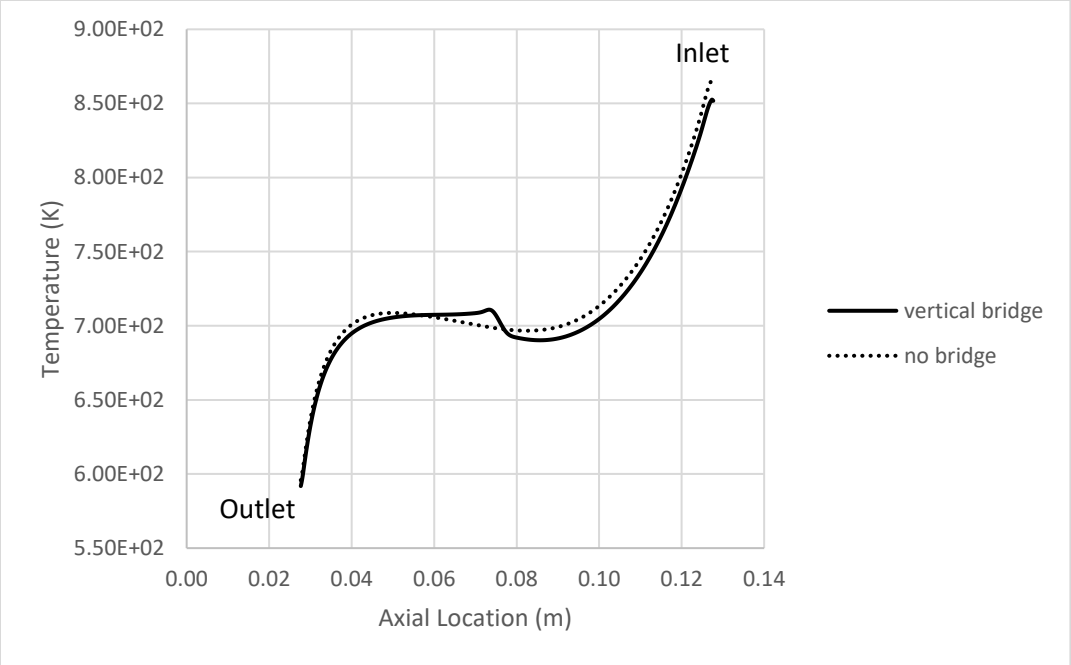

Figure 4.60 Temperature comparison at the top of armor tile

Parallelogram Bridge

In this bridge design, to mitigate the flow perturbation caused by the bridge, it is oriented parallel to the jet velocity vector. The flow streamlines are therefore parallel to the wall, and should reduce the extent of the stagnant zone.

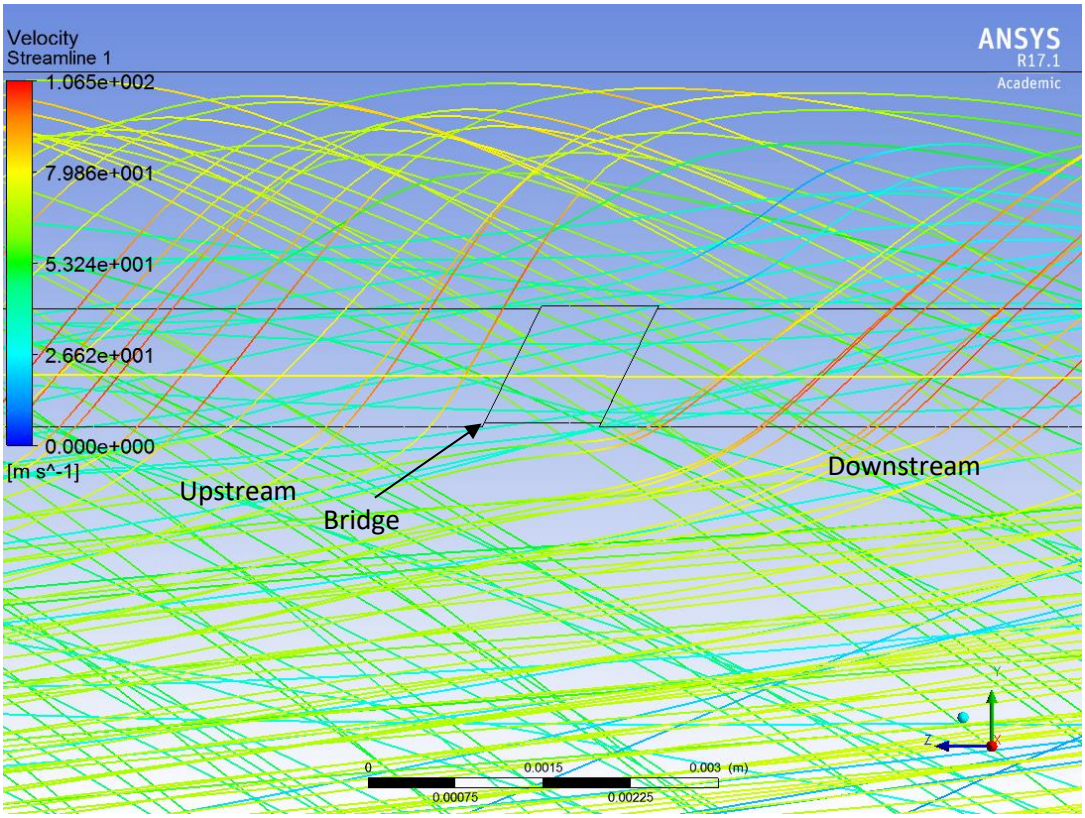

Figure 4.61 Parallelogram bridge and streamlines

In Figure 4.61, the flow patterns before and after the bridge are still different from those for the case with no bridge. Downstream of the bridge, streamlines are more inclined toward the right side; this causes impingement, and therefore causes the heat transfer to be less effective.

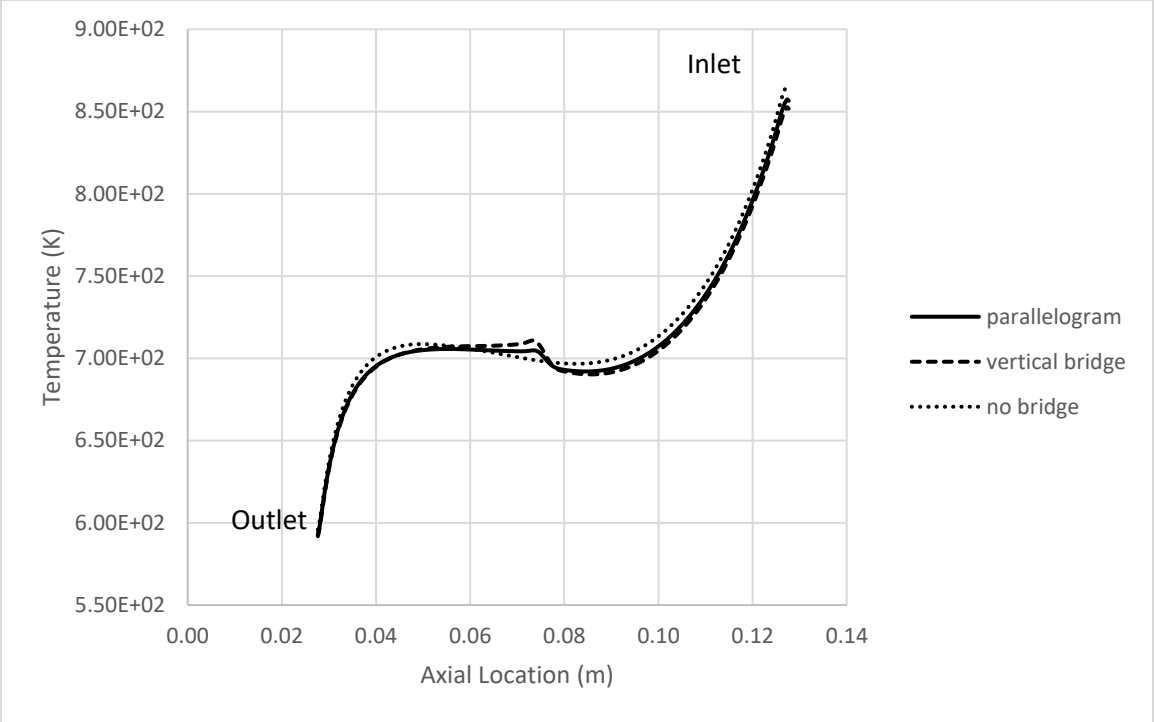

Figure 4.62 Temperature distribution at the top of armor tile

One benefit of this design is the decrease in temperature at the local peak. The overshoot after the bridge is less than was obtained with the vertical bridge case, and the parallelogram bridge has less of an effect on the temperature, as the temperature returns to the previous levels more quickly than was the case for the vertical bridge case.

0.5 mm Bridge Case

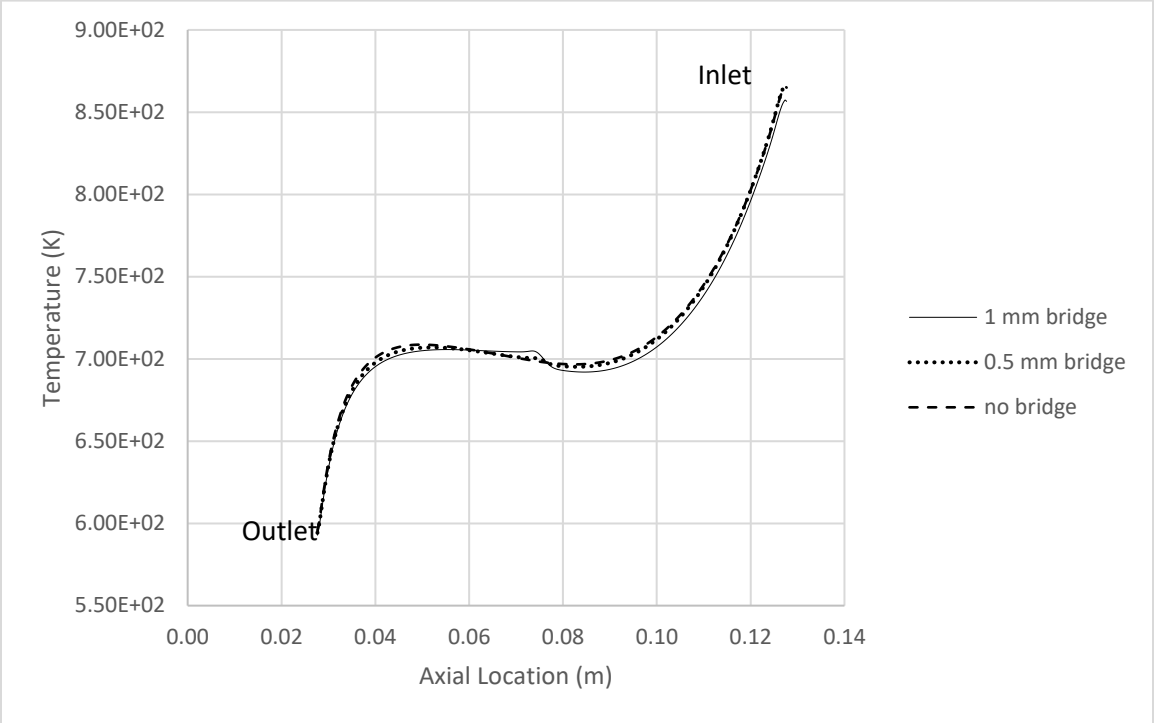

Figure 4.63 Temperature distribution at the top of armor tile

In Figure 4.63, the peak at the bridge is significantly less for the 0.5 mm case than for the 1 mm case. In addition, before the bridge, the temperature is slightly higher for the 0.5 mm case due to increased flow cross-section, which causes lower jet velocities. The jet velocities for the three cases are given in Figure 4.64. Before the bridge, the jet velocity is higher for the 0.5 mm bridge case than for the no bridge case, and it is the highest for 1 mm bridge case.

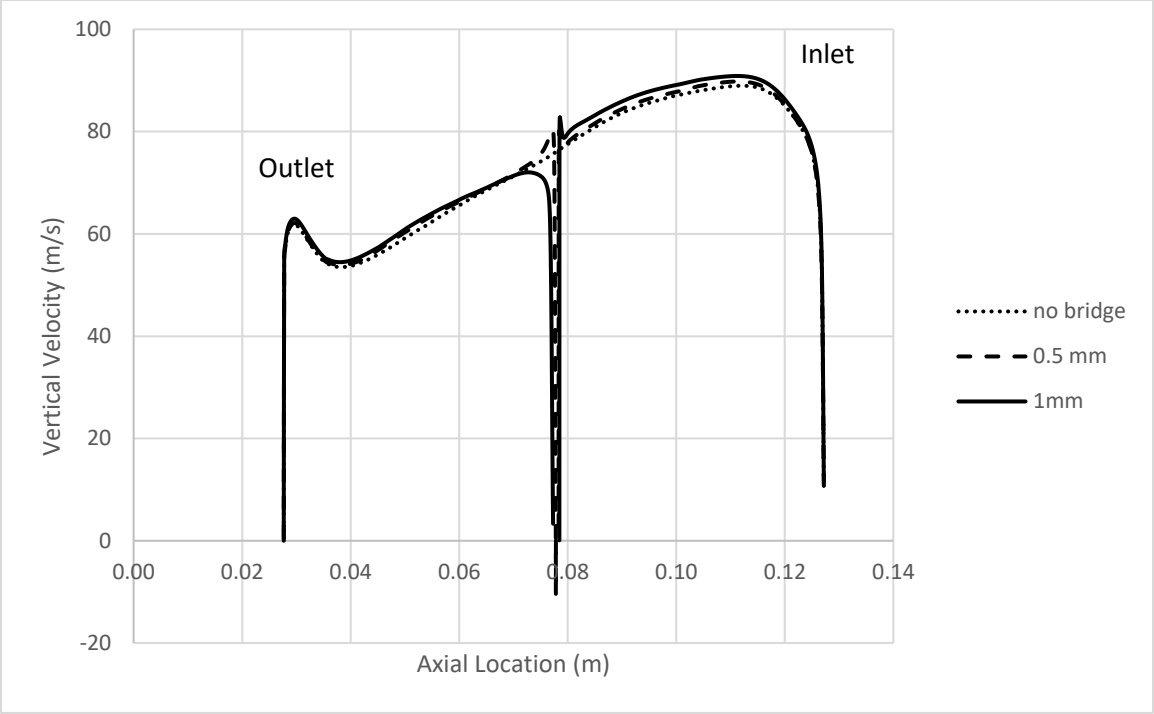

Figure 4.64 Vertical Jet Velocity at the Slot

4.2.9 Parametric Study

CuCrZr alloys are annealed at different temperatures, usually between 600 ℃ and 800 ℃, for different applications. At temperatures above 800 ℃, the strength of CuCrZr degrades rapidly [55]. Therefore, the temperature of the divertor under mechanical stress should not exceed its annealing temperature. To determine the allowable operation range with different mass flow rates and heat fluxes, a parametric design study was conducted. In this case, a constant contraction to 2 mm diameter inlet manifold is used at 4 MPa outlet pressure. The results are given in Figure 4.65, and the corresponding pressure drops are given in Figure 4.67. It is obvious that above the melting temperature, the material melts

down, but the model does not consider phase change, and the simulations that exceed the melting point are not realistic.

In Figure 4.66, results of constant contraction to 2 mm diameter inlet manifold with two "auxiliary" slots are given. For simplicity, results for only mass flow rates of 40 g/s (*Re* = 40,000) and 80 g/s (*Re* =80,000) are included. According to the simulations, the "auxiliary" slots increased the uniform heat flux capacity by nearly 1 MW/m^2 for a mass flow rate of 40 g/s and 2 MW/m^2 for 80 g/s based on the recommended temperature for the mechanical properties of the copper alloy (~1000 K)

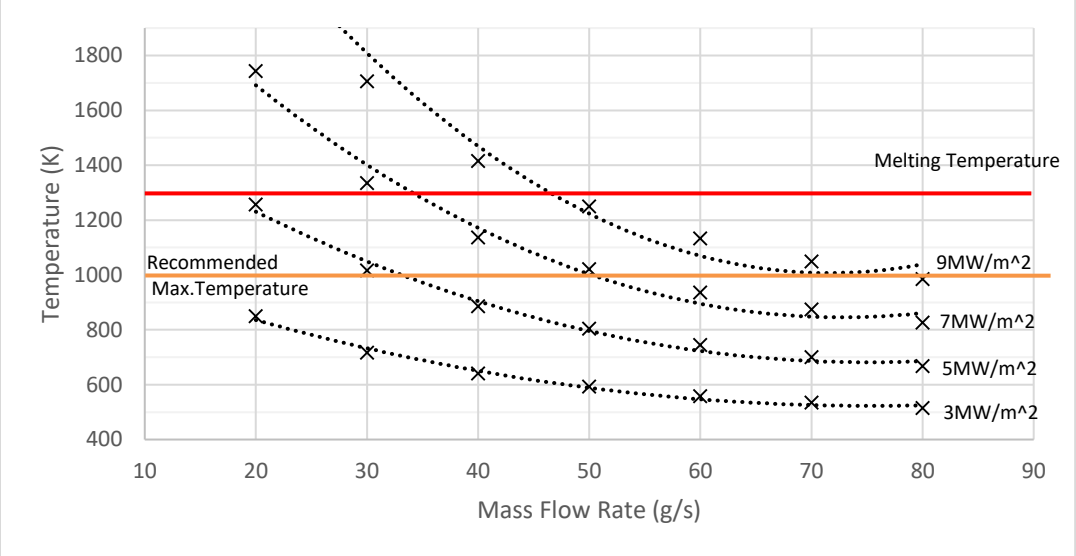

Figure 4.65 Max. Surface Temperature at Different Heat Fluxes and Mass Flow Rates

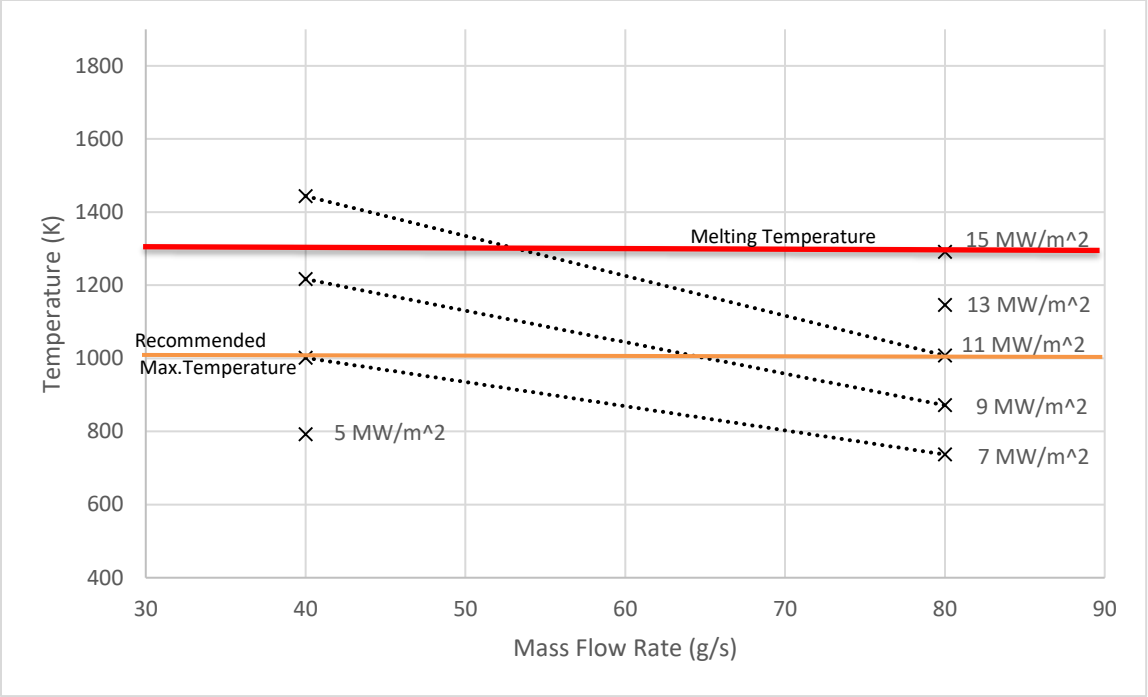

Figure 4.66 Max. Surface Temperature at Different Heat Fluxes and Mass Flow Rates with Double Slot

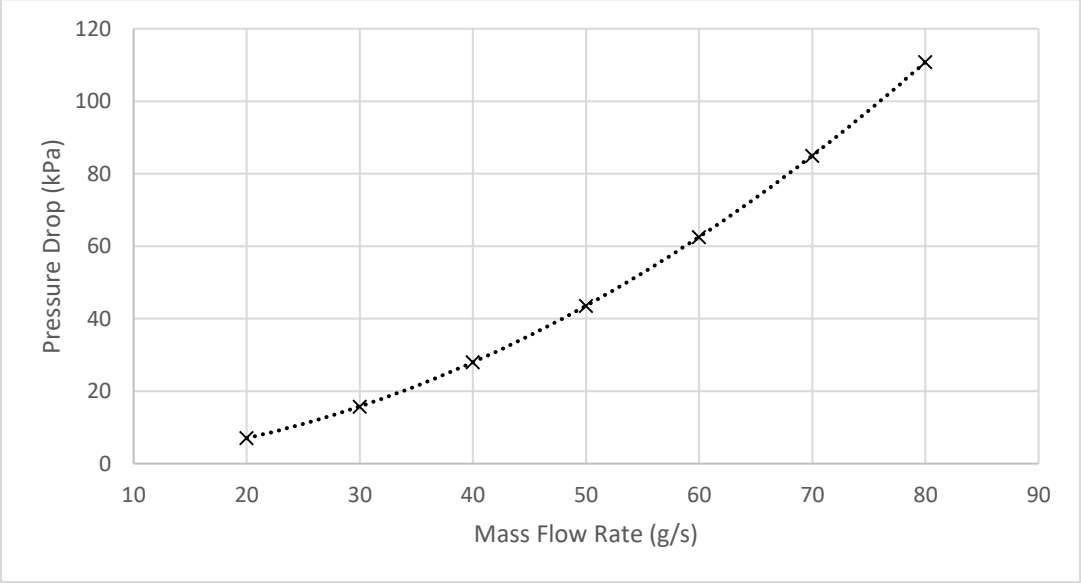

Figure 4.67 Pressure Drops at Different Mass Flow Rates

4.2.10 Effect of Armor Layer Thickness

In the ARIES-CS T-tube design, and consequently in the model presented here, the armor layer thickness is 0.3 mm. In MPEX, that thickness may not be sufficient for steady state operation. Therefore, to see how the thickness of the armor tile affects temperature, its thickness was increased in 4 mm increments. Since most of the thermal resistance belongs to the fluid side (more than an order of magnitude), a drastic temperature rise is not expected.

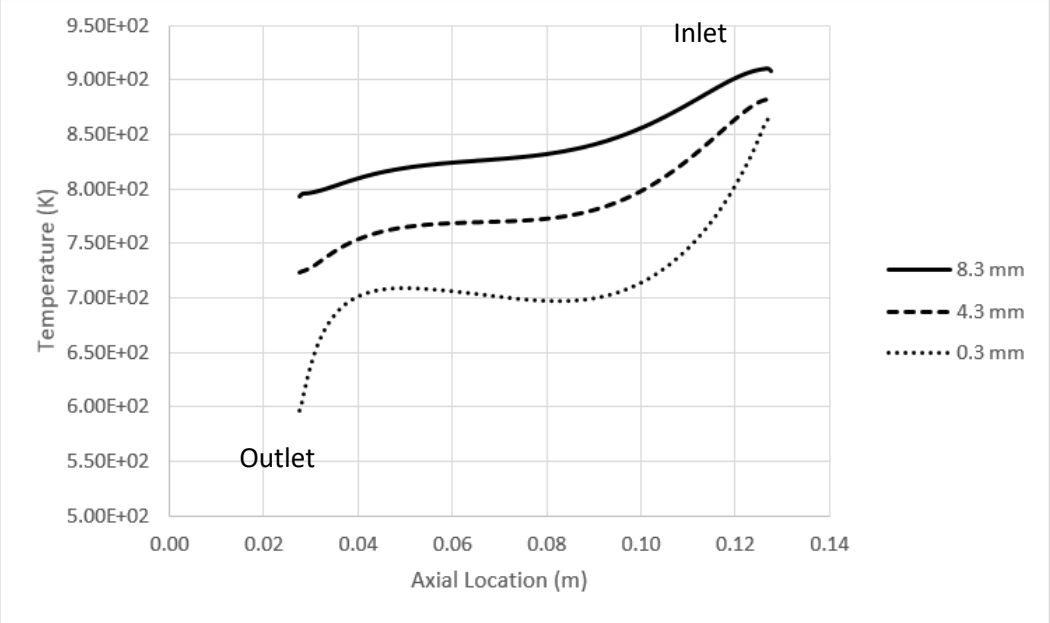

Figure 4.68 Temperature comparison for different armor thickness

In Figure 4.68, the average surface temperature increase is around 50 K, and the maximum surface temperature increase is around 20 K for each additional 4 mm of armor. The high conductivity of the material (CuCrZr) plays a moderating role, and the temperature variation of 8.3 mm thick armor along the axis decreased by a factor of two compared with that for 0.3 mm armor.

4.2.11 Materials Evaluation

It is most probable that the divertor will be under cyclic thermal loads, which deteriorates the thermal conductivity of CuCrZr. To our knowledge, there is no study that investigates the thermal conductivity of this alloy after a number of cycles. However, Davis et al. pointed out that reaging CuCrZr at 925 °C resulted in a 22% to 32% reduction in thermal conductivity [55]. Therefore, a few simulations were performed of this alloy with a 30% lower thermal conductivity. The temperature results are given in Figure 4.69.

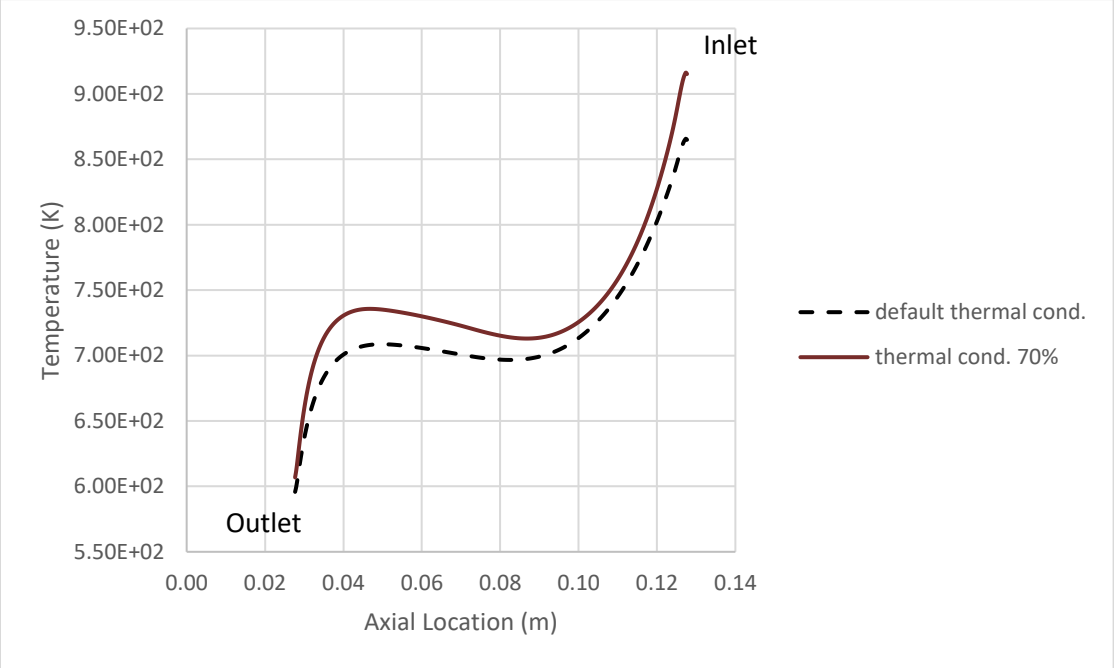

Figure 4.69 Temperature profiles at the top of the armor tile for two different thermal conductivity

A 30% reduction in thermal conductivity causes a 22 K increase in overall surface temperature and a 60 K in maximum surface temperature. A 30% reduction in thermal conductivity is the worst case, and even under this circumstance, the temperature difference may be acceptable.

Because local heat fluxes might exceed 12 MW/m^2, keeping the temperature below recommended values is not possible with a mass flow rate that is in the range of acceptable pressure drops (~100 kPa) based on a previous experimental test that is similar to the work presented in this thesis [59]. Therefore, simulations were performed for another high temperature resistant material, Titanium-Zirconium-Molybdenum (TZM) alloy.

Even though TZM alloy has very low thermal conductivity (around one-third that of the copper alloy), it has a very high melting temperature (more than 2700 K) and a high recrystallization temperature (around 1700 K). We therefore expect that the surface temperatures will be significantly higher, but they should still be in the acceptable range for the same boundary conditions with the copper alloy. The results for 5 MW/m^2 heat flux are given in Figure 4.70. As expected, the surface temperatures are considerably higher for TZM than for CuCrZr.

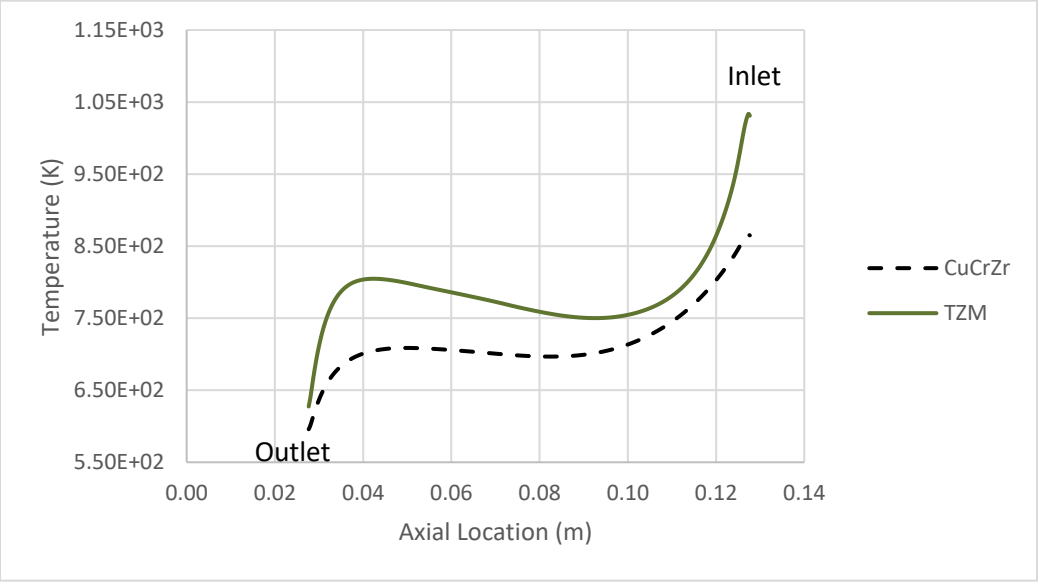

Figure 4.70 Temperature profiles at the top of the armor tile for CuCrZr and TZM

A parametric study similar to the one presented in Figure 4.65 was repeated with TZM, and the result are given in Figure 4.71. Due to the low thermal conductivity of the TZM, the temperature gradient is greater at the inlet side, and at the corner, the temperature reaches very high levels. Based on the results of the parametric study, this material can handle up to 8 MW/m^2 of uniform heat flux without exceeding its recrystallization temperature at 40 g/s helium mass flow rate. Once the heat flux exceeds 13 MW/m^2, the material will start to melt. At 80g/s mass flow rate, the divertor can safely dissipate 11 MW/m^2 uniform heat flux.

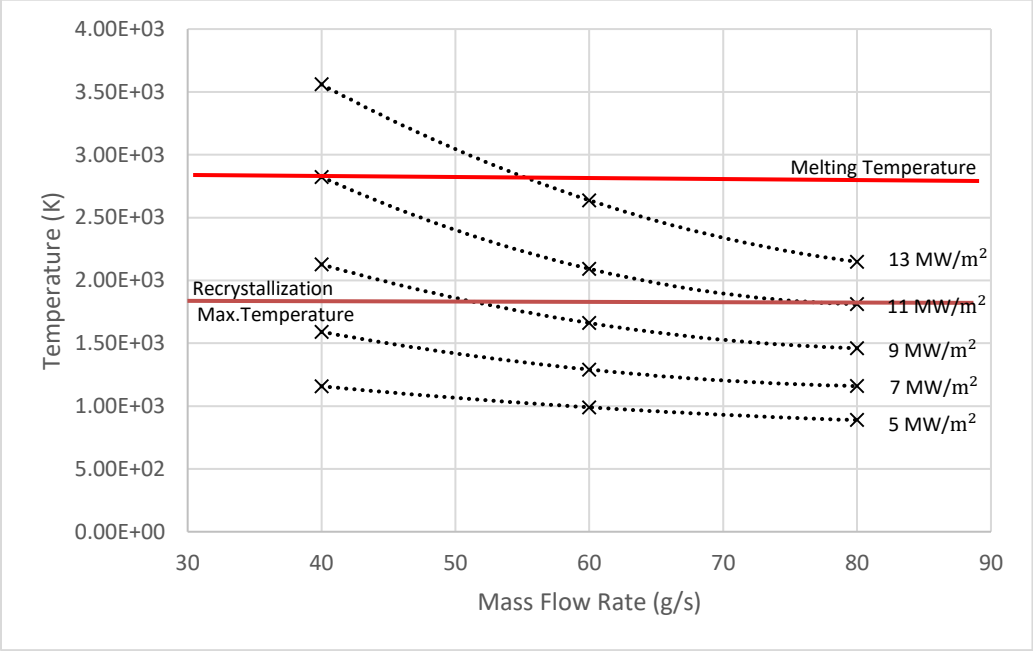

Figure 4.71 Max. Surface Temperature at Different Heat Fluxes and Mass Flow Rates

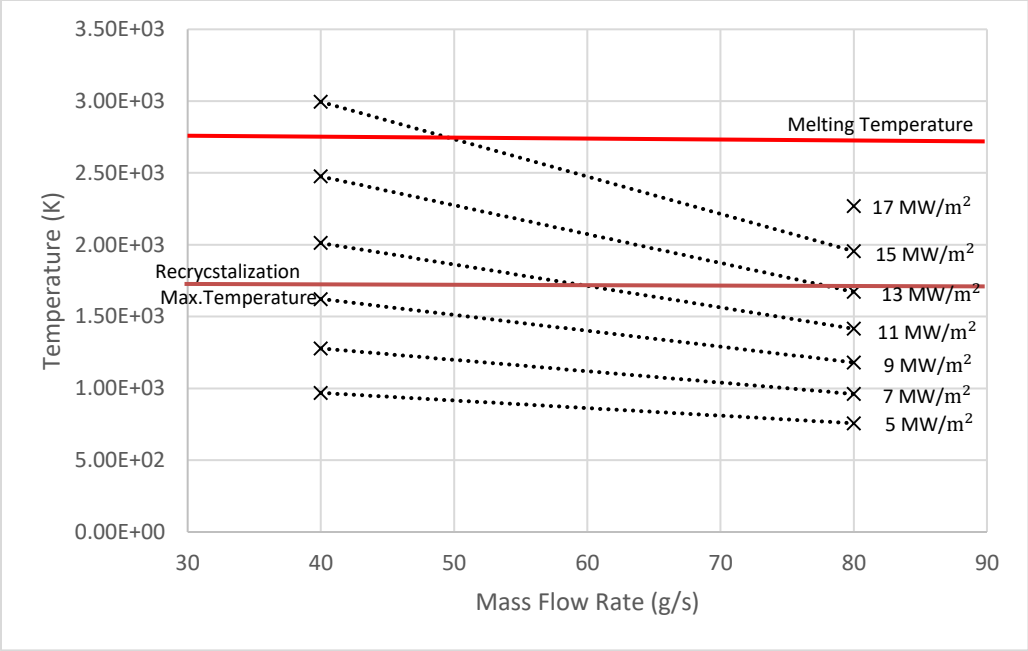

Figure 4.72 Max. Surface Temperature at Different Heat Fluxes and Mass Flow Rates with Double Slot

In Figure 4.72, results for a constant contraction to 2 mm diameter inlet manifold with two "auxiliary" slots are given. For simplicity, only 40 g/s (*Re* = 40,000) and 80 g/s (*Re* =80,000) cases are included. According to the simulations, similar to the copper alloy case, partial secondary slot has increased the uniform heat flux capacity nearly 1 MW/m^2 for 40 g/s and 2 MW/m^2 for 80 g/s mass flow rates based on the recrystallization temperature of TZM (~1700 K)

4.2.12 Sensitivity to Turbulence Model

Every turbulence model has a different way to solve the governing equations, and based on the flow characteristics, their accuracy in predicting the actual flow parameters may vary. Therefore, the literature has been reviewed to find studies reporting turbulence models that are in good agreement with experimental results for impinging jets.

Koncar et al. reported a good agreement for HEMJ design between experimental data and numerical results with the SST K-Omega model [60]. In the study, they used ANSYS™ CFX® 11.0 to investigate the optimum diameter and the distribution of the jets in the HEMJ cartridge. The 3-D model consists of 400,000 hexahedral elements, which represent a 30° 'wedge' of the full model with periodic boundary conditions. In another study, Gayton used the Spalart-Almaras turbulence model in ANSYS™ Fluent® to compare HTC in the numerical model of a helium-cooled flat-plate (HCFP) divertor design, which utilizes either round or planar jets, to experimental results [61]. The 3D half model has 1.67 million mixed quadrilateral and hexahedral cells. The results showed that the SA turbulence model predicted the HTC within a 5% range.

Based on the conclusions reported in the previous studies, the simulations were repeated by using the SST K-Omega and SA turbulence models to investigate how different turbulence models affected these results. The temperature profile obtained for these two turbulence models is given in Figure 4.73, and compared with the previous results obtained with the SKE model.

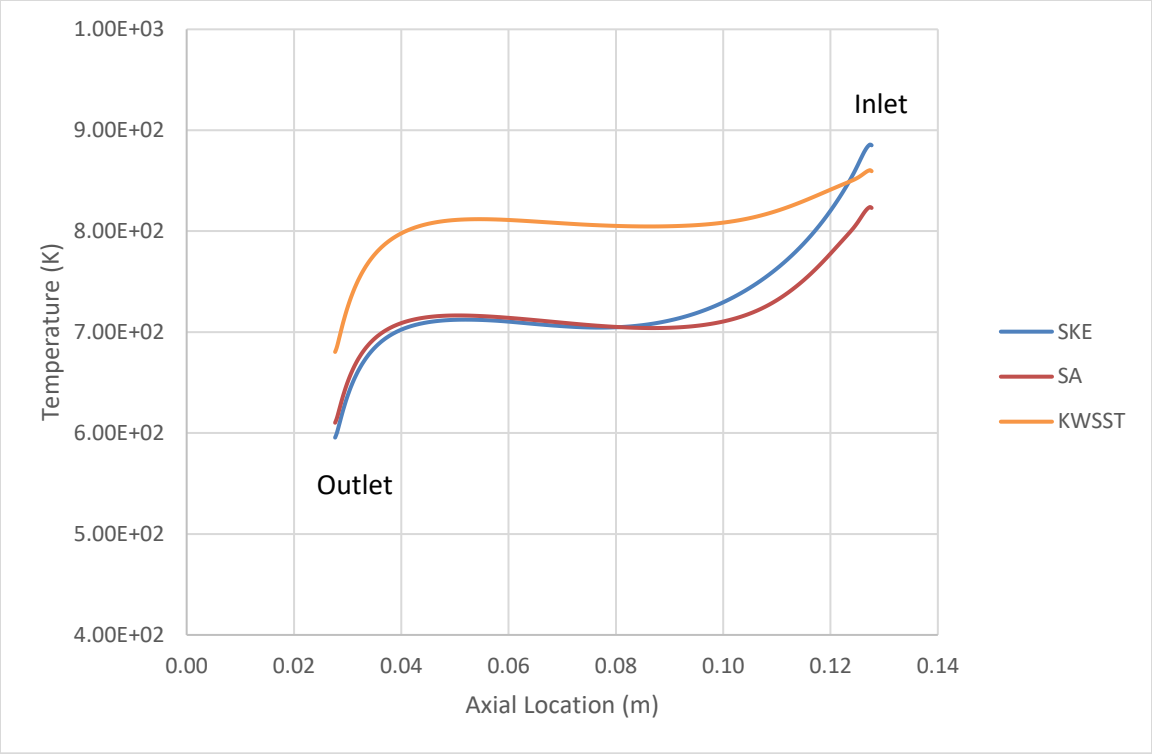

Figure 4.73 Temperature profiles at the top of the armor tile for different turbulence models.

The highest average surface temperature was observed with the SST K-Omega turbulence model. Although all three models give similar maximum surface temperatures, the SKE model gives the highest maximum surface temperature. It therefore appears, admittedly based on a single case, that the model used in this thesis (SKE) is the most conservative one in terms of predicting the highest surface temperature and the highest temperature variation along the axis.

CHAPTER 5. CONCLUSIONS AND RECOMMENDATIONS

In this study, the thermal-hydraulic performance of the T-tube divertor concept has been numerically simulated and evaluated using a commercial CFD software package, ANSYS™ Fluent®. Both the counter and parallel flow configurations have been examined. As presented in the previous Chapter, after specifying a structurally robust and physically manufacturable geometry, additional parametric studies and further modifications were examined on the geometry to see if these modifications can improve the suitability of this concept for cooling targets in a linear plasma simulator. This Chapter summarizes these results and provides recommendations for future work.

5.1 Conclusions

The following conclusions are drawn from the results presented in the previous chapters. They are divided based on flow configuration.

5.1.1 Counter-Flow

The counter-flow configuration gives acceptable thermal performance for short length divertors. It outperforms the parallel flow configuration for a straight (*i.e.*, constant cross-section) inner tube when the axial extent of the test section is less than 10 cm. However, the counter-flow configuration is not as scalable to longer divertor modules as the parallel flow case due to quick degradation of HTC along the tube axis, and its thermal performance is less sensitive, in terms of improving axial variation along the tube axis, to inner tube modifications than parallel flow. In counter-flow, the helium flow stagnates near the dead end, and this stagnant zone becomes larger with increasing tube length. The

reduced cross-sectional area, due to having both inlet and exit at the same side, also leads to a greater pressure drop and a lower flow rate. These cannot be resolved with changes to the inlet manifold; instead, resolving these issues would require significant changes to the channel geometry at the exhaust end rather than the inlet manifold, which is beyond the scope of this thesis.

Several design modifications were analyzed; the conclusions drawn from these analyses are given below:

a. Flow through a slot with a linearly increasing width was considered in an attempt to reduce the flow stagnation region at the dead end. Although increasing the slot width at the far side of the inlet allowed more coolant to flow from the dead end side of the slot, this modification significantly decreased the jet velocity for a given mass flow rate and increased the temperature variations along the tube axis.
b. The wall thickness of the inner tube was linearly tapered along the axis in an attempt to lower the pressure drop between the inner tube and the annulus at the dead end, and increase the jet velocity. Unfortunately, this modification did not reduce the temperature variations.
c. The slot was tapered through the inner tube wall thickness at an angle of 45° (Figure 4.8) in an attempt to decrease the pressure drop across the slot. However, this modification had no noticeable effect on the flow compared to the case with a "straight" (*i.e.*, untampered) slot.

d. Three different contraction geometries from the inlet to the dead end were considered for the inlet manifold: a linear (*i.e.*, constant-slope) contraction, an exponential contraction and a contraction consisting of three linear contractions with different slopes. The model with the linear contraction had the best thermal performance of the three, with a maximum surface temperature nearly 150K less than that for the straight inlet manifold case with no contraction.

5.1.2 Parallel Flow

Because the counter-flow configuration had a poor overall flow distribution due to stagnant flow region at the end, the parallel flow configuration, where the inlet and outlet are on the opposite ends of the T-tube, was also investigated. Only the linear contraction case from the three different contraction geometries (Figure 4.10) was considered for the parallel flow configuration, along with some other modifications as discussed in Chapter 4. A parametric study was then performed on the most promising of the parallel flow configurations to determine the allowable range of operating conditions.

The main issue with the parallel flow configuration is the stagnant zone at the inlet side. Two approaches to reduce the negative effect of this stagnant zone on the temperature distribution were evaluated here: (1) increasing the vertical jet velocity at the slot, which has a substantial effect on performance; and (2) reducing the axial velocity in the annulus.

The conclusions drawn from these analyses are summarized below:

a. By contracting the inner tube at the locations where the temperatures are lower, the axial velocity in the inner tube was minimized for higher temperature sections. For this reason, an inlet manifold with a parabolically varying cross-sectional area was simulated. Unfortunately, the temperature rise on the inlet side was found to be greater than that for the case with a straight (*i.e.*, constant-area) inner tube
b. The slot width was modified to become increasingly narrow from the outlet to the inlet in order to equalize heat extraction at both ends at the expense of decreased total heat removal. Nevertheless, due to a lower pressure drop at the outlet side, the flow rate and jet velocity decreased at the inlet side, increasing temperature variations.
c. The linear manifold contraction geometry considered for the counter-flow configuration restricted the flow at the outlet side and increased the jet velocity at the inlet side when used in parallel flow. This helps to reduce the effects of the stagnant zone at the inlet, and the contraction increases the cross-sectional area of the annulus, reducing axial velocity and pressure drop. In parallel flow, the linear contraction decreased the maximum surface temperature by more than 200K (*vs.* 150K for the counter-flow case). The contracting inlet manifold modification is not considered as an optional feature for the parallel flow configuration due to the inferior performance of the straight inner tube case for parallel flow than counter-flow.
d. The variations in the divertor temperature distribution along the axis changes with the contraction ratio of the inner tube. Four different outlet diameters ranging from

2 mm to 5 mm were investigated. The 2 mm case has the best performance, with a slight increase in pressure drop compared to the straight inner tube case. Even smaller inner tube diameters may further improve temperature uniformity on the heated surface; however, this will result in a larger pressure drop.

e. Introducing additional partial slots at the inlet reduces the negative effects of the stagnant zone at the inlet. Adding two 15 mm long and 0.5 mm wide slots located 30 degrees azimuthally from the main slot was found to reduce the highest temperature at the center of the top of the armor tile by more than 100K. It also decreased the pressure drop by nearly 10 kPa at a mass flow rate of 40 g/s (*Re* = 40,000).

f. In experimental studies of the T-tube divertor, the flow to the divertor will typically be fully developed turbulent flow. In the simulations, a uniform velocity profile at the inlet was used instead for simplicity. The results indicate that the difference between imposing a boundary condition of fully-developed flow and a uniform flow is negligible.

g. In the actual fusion reactor, the heat flux on the divertor will probably be non-uniform. Localized hot spots may cause flow instabilities in some designs, which could lead to material failure. This specific design was found to be fairly insensitive to helium mal-distribution for non-uniform heating. This is attributed to the heat transfer characteristics of impinging jets, which are isothermal before impingement, and the expansion in the exhaust volume after impingement due to the contracting inner tube, which allows the heated coolant to expand easily in the annulus. The maximum observed variation in mass flow rate is less than 3% for the

worst-case scenario, which corresponds to a boundary condition on the temperature of the melting point of the solid on one side and a boundary condition of zero heat transfer on the other side. For the axially non-uniform heating case, the maximum variation in mass flow rate is less than 1%.

h. Supplying the helium obliquely, instead of along the horizontal axis, increases the vertical component of the jet velocity at the inlet, which enhances the heat transfer at the inlet. An inlet inclined at 45° may reduce the maximum temperature at the center of the top of the armor tile by as much as 90K, although it also increases the pressure drop by nearly 8 kPa at a mass flow rate of 40 g/s (Re = 40,000). However, it may not be possible to "tilt" the inlet by this much in MPEX.

i. The slot width has a substantial effect on cooling at a given mass flow rate, presumably because it directly affects the velocity. Additionally, the slot width directly affects the ratio of vertical to horizontal velocity exiting the slot, which significantly impacts the stagnant zone. A reduction of slot width from 1.0 mm to 0.5 mm reduces the average and maximum surface temperatures by nearly 100K and 180K, respectively.

j. Even if it were possible to machine a slot along the entire length of the T-tube, the slot cannot maintain a constant width under dynamic loads without links (bridges) across its thickness. Although mechanical stresses were not considered here, the addition of a 0.5 mm or 1.0 mm bridge midway along the axis increases the local surface temperature by a few degrees. Additionally, the bridges reduce the maximum surface temperature at the inlet by restricting the flow and directing more

flow to inlet. Therefore, adding a few bridges across the slot does not appear to have much adverse effect on the thermal performance of the divertor.

k. A parametric study of the effects of mass flow rate and incident heat flux was used to determine the operating parameter range of the divertor with an inlet manifold consisting of a constant-slope contraction to a 2 mm diameter. At the initial design mass flow rate of 40 g/s (*Re* = 40,000), this divertor configuration can handle a uniform heat flux of 6 MW/m^2 without exceeding the recommended maximum temperature (~1000 K) based on the mechanical properties of the copper alloy. Heat fluxes exceeding 8 MW/m^2 will melt the plasma-facing material. Doubling the mass flow rate to 80 g/s mass flow rate (*Re* = 80,000), which increases the pressure drop to around 100 kPa, increases the maximum uniform heat flux that can be accommodated by the divertor without affecting the mechanical properties of the copper alloy to 9 MW/m^2. Adding two partial slots at the inlet increases these values for maximum attainable heat flux to 7 MW/m^2 at a mass flow rate of 40 g/s, and to almost 11 MW/m^2 at 80 g/s mass flow rate.

l. The thickness of the armor layer in the original T-tube design and the design presented in this thesis is 0.3 mm. Increasing the thickness of this armor layer does not significantly increase the maximum surface temperature for an armor made of the copper alloy due to its high thermal conductivity. Although the average surface temperature increases by almost 100K, the increase in the maximum surface temperature is less than 50 K for an 8.3 mm armor layer thickness.

m. Over-aging of the CuCrZr alloy may result in a considerable decrease in its thermal conductivity. Additionally, operating above 925 °C, may cause a permanent 30%

reduction in the copper alloy's thermal conductivity [55]. In this case, the maximum surface temperatures would be 70K higher than the temperatures in the cases evaluated with non-aged material properties.

n. Since it is not possible to extract the desired heat flux of 12 MW/m^2 by using the copper alloy, a refractory material, Titanium-Zirconium-Molybdenum (TZM) alloy, was considered in a set of simulations with the same contraction geometry. The results show that a layer of TZM armor can accommodate heat fluxes of an 8 MW/m^2 and 11 MW/m^2 at mass flow rates of 40 g/s (*Re* = 40,000) and 80 g/s (*Re* = 80,000), respectively, without exceeding its recrystallization temperature (~1700K). Adding two partial slots at the inlet increases the maximum attainable heat flux to almost 10 MW/m^2 at 40 g/s and to 13 MW/m^2 at 80 g/s.

o. The results indicate that the selected turbulence model, the standard *k*-ε, is the most conservative choice in terms of the predicted maximum surface temperature and the maximum surface temperature variation along the axis. However, it has not been verified nor validated against experiment that the standard *k*-ε is the most accurate turbulence model for the geometry presented in this thesis.

p. Based on the simulations performed in this study, the best thermal performance was obtained with the geometry that has a constant-slope (linear) contraction at the inlet manifold to an outlet diameter of 2 mm and two partial slots located at 30 degrees from the zenith. Increasing the total cross-section with an additional slot also helps to decrease the total pressure drop in the system by about 8 kPa at a mass flow rate of 40 g/s (*Re* = 40,000). Furthermore, the additional slots give a more uniform transverse temperature distribution at the inlet due to a wider azimuthal

impingement region. On the other hand, inclining the inlet increases the total pressure drop (by~10 kPa at a mass flow rate of 40 g/s) because it increases the jet velocity at the inlet. This suggests that adding two partial slots will give better performance than inclining the inlet. Finally, adding these partial slots increases the heat removal capacity of the divertor to 9 MW/m^2 at 40 g/s and 11 MW/m^2 at 80 g/s without exceeding 1000 K in the copper alloy. If the divertor armor is instead made of TZM, the same configuration will withstand nearly 9 MW/m^2 at 40 g/s and 13 MW/m^2 at 80 g/s without exceeding its recrystallization temperature of ~1700K.

5.2 Future Work and Recommendation

The following suggestions and recommendations are offered to complement and extend this Master's thesis:

- The mass flow rates used in these simulations were chosen from previous studies. Although the Reynolds numbers are matched, the pressure drop at a given mass flow rate will be different due to differences in coolant inlet pressures (i.e., densities), and velocities. Actual measured mass flow rates and pressure drops from experimental data should therefore be used in future simulations if available.
- Even if it is not possible to conduct experiments at the prototypical conditions, some experimental data are required for validation purposes.
- Any eccentricity in the position of the inner tube with respect to the outer tube could affect the pressure drop in the annulus. This effect should be investigated further using numerical simulations.

- Optimizing the azimuthal location and dimensions of the additional slots to provide a more uniform temperature distribution on the heated surface should be considered.
- The thermal-hydraulic performance of multiple T-tube cartridges in parallel should be investigated for the target plate assembly.
- Mechanical stress analyses should to be performed to account for thermal and mechanical stresses, and to optimize the number of bridges and their dimensions to minimize slot deformation.
- There is little knowledge at present about how thermal conductivity degrades over several thermal cycles at higher temperatures. This degradation, once quantified, should be included in these models to evaluate current proposed armor materials. If it is impractical to obtain appropriate experimental validation data, verification with another CFD software package should be considered.

APPENDIX A

The user defined function (UDF) used for materials as an input file is provided below. Units are K for temperature, W/m·K for thermal conductivity, Kg/m^3 for density, J/Kg·K for specific heat and Pa·s for viscosity.

(

(helium-real fluid

(chemical-formula . he)

(density (constant . 0.1625))

(specific-heat (polynomial piecewise-linear (200 . 5200.975) (225 . 5194.996) (250 . 5191.174) (275 . 5188.704) (300 . 5187.105) (325 . 5186.08) (350 . 5185.443) (375 . 5185.069) (400 . 5184.877) (425 . 5184.811) (450 . 5184.833) (475 . 5184.915) (500 . 5185.039) (525 . 5192.985476) (550 . 5185.362) (575 . 5185.544) (600 . 5185.732) (625 . 5185.923) (650 . 5186.114) (675 . 5186.302) (700 . 5186.488) (725 . 5186.669) (750 . 5186.846) (775 . 5187.017) (800 . 5187.183) (825 . 5187.343) (850 . 5187.498) (875 . 5187.647) (900 . 5187.791) (925 . 5187.929) (950 . 5188.063) (975 . 5188.191) (1000 . 5188.314) (1025 . 5188.433) (1050 . 5188.547) (1075 . 5188.657) (1100 . 5188.763) (1125 . 5188.865) (1150 . 5188.964) (1175 . 5189.058) (1200 . 5189.15) (1225 . 5189.238) (1250 . 5189.323) (1275 . 5189.404) (1300 . 5189.484) (1325 . 5189.56) (1350 . 5189.634) (1375 . 5189.705) (1400 . 5189.774) (1425 . 5189.841)))

(thermal-conductivity (polynomial piecewise-linear (200 . 0.1257070) (225 . 0.1351572) (250 . 0.1443899) (275 . 0.1534200) (300 . 0.1622617) (325 . 0.1709278) (350 . 0.1794304) (375 . 0.1877801) (400 . 0.1959870) (425 . 0.2040599) (450 . 0.2120069) (475 . 0.2198355) (500 . 0.2275524) (525 . 0.2351637) (550 . 0.2426751) (575 . 0.2500918) (600 . 0.2574183) (625 . 0.2646592) (650 . 0.2718184) (675 . 0.2788996) (700 . 0.2859063) (725 . 0.2928417) (750 . 0.2997086) (775 . 0.30651) (800 . 0.3132483) (825 . 0.319926) (850 . 0.3265454) (875 . 0.3331084) (900 . 0.3396173) (925 . 0.3460737) (950 . 0.3524795) (975 . 0.3588363)

(1000 . 0.3651458) (1025 . 0.3714093) (1050 . 0.3776283) (1075 . 0.3838042) (1100 . 0.3899381) (1125 . 0.3960313) (1150 . 0.402085) (1175 . 0.4081002) (1200 . 0.414078) (1225 . 0.4200194) (1250 . 0.4259252) (1275 . 0.4317965) (1300 . 0.437634) (1325 . 0.4434386) (1350 . 0.4492111) (1375 . 0.4549522) (1400 . 0.4606627) (1425 . 0.4663433) (1450 . 0.4719946) (1475 . 0.4776174) (1500 . 0.4832121)))

(viscosity (polynomial piecewise-linear (200 . 0.00001582165) (225 . 0.00001697721) (250 . 0.0000180987) (275 . 0.00001919024) (300 . 0.00002025515) (325 . 0.0000213553) (350 . 0.00002243521) (375 . 0.0000234964) (400 . 0.00002454021) (425 . 0.00002556781) (450 . 0.00002658025) (475 . 0.00002757847) (500 . 0.00002856332) (525 . 0.00002953555) (550 . 0.00003049585) (575 . 0.00003144484) (600 . 0.0000323831) (625 . 0.00003331115) (650 . 0.00003422946) (675 . 0.00003513848) (700 . 0.00003603862) (725 . 0.00003693024) (750 . 0.00003781371) (775 . 0.00003868935) (800 . 0.00003955746) (825 . 0.00004041832) (850 . 0.0000412722) (875 . 0.00004211934) (900 . 0.00004295999) (925 . 0.00004379435) (950 . 0.00004462264) (975 . 0.00004544505) (1000 . 0.00004626176) (1025 . 0.00004707296) (1050 . 0.00004787879) (1075 . 0.00004867943) (1100 . 0.00004947501) (1125 . 0.00005026569) (1150 . 0.00005105159) (1175 . 0.00005183284) (1200 . 0.00005260956) (1225 . 0.00005338188) (1250 . 0.00005414989) (1275 . 0.00005491372) (1300 . 0.00005567345) (1325 . 0.0000564292) (1350 . 0.00005718104) (1375 . 0.00005792907) (1400 . 0.00005867338) (1425 . 0.00005941405) (1450 . 0.00006015116) (1475 . 0.00006088479) (1500 . 0.000061615)))

(molecular-weight (constant . 4.002602))

)

(copper-alloy solid

(chemical-formula . cucr1zr)

(density (constant . 8790))

(specific-heat (polynomial piecewise-linear (273 . 387) (293 . 388) (373 . 392) (473 . 400) (573 . 410) (673 . 422) (773 . 437) (873 . 454) (973 . 473) (1173 . 518)))

(thermal-conductivity (polynomial piecewise-linear (293 . 379) (327 . 373) (373 . 365) (423 . 359) (473 . 355) (523 . 352) (573 . 351) (623 . 351) (673 . 352) (723 . 354) (773 . 357) (823 . 358) (873 . 362) (923 . 367) (973 . 372) (1023 . 379)))

)

(TZM-alloy solid

(chemical-formula . ti-zr-mo)

(density (constant . 10200))

(specific-heat (polynomial piecewise-linear (300 . 272) (400 . 271) (600 . 272) (700 . 274) (800 . 276) (900 . 280) (1000 . 285) (1200 . 295) (1500 . 318) (1600 . 326) (1900 . 362) (2000 . 372) (2100 . 387) (2500 . 446) (2600 . 462)))

(thermal-conductivity (polynomial piecewise-linear (300 . 127.5) (400 . 125.5) (600 . 120.5) (700 . 118.4) (800 . 115.5) (900 . 113) (1000 . 110) (1200 . 103.8) (1500 . 94.58) (1600 . 91.2) (1900 . 82.86) (2000 . 80.4) (2100 . 77.84) (2500 . 69.1) (2600 . 67.4)))

)

)

REFERENCES

[1] Grenon, M., *Global Energy Resources.* Annual Review of Energy, 1977. **2**(1): p. 67-94.

[2] Rachkov, V., et al., *From the first nuclear power plant to fourth-generation nuclear power installations [on the 60th anniversary of the World's First nuclear power plant]*. Thermal Engineering, 2014. **61**(5): p. 327-336.

[3] *Magnetic fusion technology*, ed. J. Brotankova and T.J. Dolan. 2013: London : Springer.

[4] Kikuchi, M., *Frontiers in Fusion Research*. Frontiers in fusion research: physics and fusion, ed. SpringerLink. 2011: London : Springer London : Imprint: Springer.

[5] *Fusion and industry together for the future*. 2009, Luxembourg: Luxembourg : Publications Office.

[6] Ihli, T., et al., *Design and performance study of the helium-cooled T-tube divertor concept.* Fusion Engineering and Design, 2007. **82**(3): p. 249-264.

[7] Rapp, J. *Materials research brings fusion power closer to reality*. 2016 [cited 2017 04/10]; Available from: https://www.ornl.gov/blog/ornl-review/materials-research-brings-fusion-power-closer-reality.

[8] R, N., *HyperPhysics*. [Online] http://hyperphysics.phy-astr.gsu.edu/hbase/NucEne/nucbin.html#c2.

[9] Stacey, W.M., *Fusion An Introduction to the Physics and Technology of Magnetic Confinement Fusion*. 2nd ed.. ed. Fusion 2e - Technology of Magnetic Confinement Fusion. 2010, Hoboken Weinheim: Hoboken : Wiley.

[10] Norajitra, P., *Divertor development for a future fusion power plant*. 2014: KIT Scientific Publishing.

[11] Charry León, C.H., *Numerical simulation of water-cooled sample holders for high-heat flux testing of low-level irradiated materials*. 2014, Georgia Institute of Technology.

[12] Song, Y., *Tokamak Engineering Mechanics*. Mechanical Engineering Series, ed. W. Wu and S. Du. 2013, Berlin/Heidelberg: Berlin/Heidelberg : Springer.

[13] Ghoranneviss, M. and S. Meshkani, *Techniques for improving plasma confinement in IR-T1 Tokamak.* International Journal of Hydrogen Energy, 2016. **41**(29): p. 12555-12562.

[14] McCracken, G., *Fusion The Energy of the Universe*. 2nd ed.. ed. Complementary Science, ed. P. Stott. 2012, Burlington: Burlington : Elsevier Science.

[15] *ITER Organization*. [2017]; Available from: http://www.iter.org/.

[16] Abdel-Khalik, S., et al., *Thermal-hydraulic studies in support of the ARIES-CS T-tube divertor design.* Fusion Science and Technology, 2008. **54**(3): p. 864-877.

[17] Clark, R.E.H., *Nuclear Fusion Research Understanding Plasma-Surface Interactions*. Springer Series in Chemical Physics, ed. D.H. Reiter and SpringerLink. 2006: Berlin, Heidelberg : Springer Berlin Heidelberg.

[18] Ueda, Y., et al., *Research status and issues of tungsten plasma facing materials for ITER and beyond.* Fusion Engineering and Design, 2014. **89**(7-8): p. 901-906.

[19] Kreter, A., et al., *LINEAR PLASMA DEVICE PSI-2 FOR PLASMA-MATERIAL INTERACTION STUDIES.* Fusion Science and Technology, 2015. **68**(1): p. 8-14.
[20] Rapp, J., et al. *The Material Plasma Exposure eXperiment MPEX: Pre-design, development and testing of source concept*. in *Fusion Engineering (SOFE), 2015 IEEE 26th Symposium on*. 2015. IEEE.
[21] Lumsdaine, A., et al., *Pre-conceptual design activities for the materials plasma exposure experiment.* Fusion Engineering and Design, 2016. **109-111**: p. 1714-1718.
[22] Rapp, J., et al. *Developing the science and technology for the material plasma exposure experiment (MPEX)*. in *APS Meeting Abstracts*. 2016.
[23] J.B.O. Caughman R.H. Goulding T.M. Biewer T.S. Bigelow C.J. Beers, I.H.C., J. Caneses, S.J. Diem, D. Donavan, A. Fadnek, D.T. Fehling, R.C. Isler, N. Kafle, E.H. Martin, C.M. Parish, J. Rapp, H. B. Ray, G.C. Shaw, M.A. Showers, and K. Wang, *Plasma Source Development for Fusion Relevant Material Testing*. 2017: Submitted for Publication

[24] Brown, R.W., et al., *Magnetic resonance imaging: physical principles and sequence design*. 2014: John Wiley & Sons.
[25] Biewer, T.M. and G. Shaw, *Initial implementation of a Thomson scattering diagnostic for Proto-MPEX a).* Review of Scientific Instruments, 2014. **85**(11).
[26] Crosatti, L., *Experimental and numerical investigation of the thermal performance of gas-cooled divertor modules*. 2008, Thesis (Ph.D.)---Mechanical Engineering, Georgia Institute of Technology, 2008.: Atlanta, Ga.
[27] Weathers, J.B., *Thermal performance of helium-cooled divertors for magnetic fusion applications*. 2007, Thesis (M. S.)--Mechanical Engineering, Georgia Institute of Technology, 2008.
[28] Youchison, D.L. and R.E. Nygren, *Flow Instabilities in Refractory Metal Porous Media Helium-Cooled Plasma Facing Components*. Conference: Proposed for presentation at the 26th Symposium on Fusion Engineering held June 1-4, 2015 in Austin, TX. 2015: ; Sandia National Laboratories (SNL-NM), Albuquerque, NM (United States). Medium: ED; Size: 6 p.
[29] Góral, D., F. Kluza, and K. Kozłowicz, *Assessment of Heat Transfer and Mass Change During Fruits and Vegetables Impingement Pre-Cooling.* International Journal of Food Engineering, 2014. **10**(1): p. 183-189.
[30] Lienhard, J. *Heat transfer by impingement of circular free-surface liquid jets*. in *Proceedings of 18th National and 7th ISHMT-ASME Heat and Mass Transfer Conference, Guwahati, India*. 2006.
[31] Zuckerman, N. and N. Lior, *Jet Impingement Heat Transfer: Physics, Correlations, and Numerical Modeling.* Advances in Heat Transfer, 2006. **39**: p. 565-631.
[32] Jambunathan, K., et al., *A review of heat transfer data for single circular jet impingement.* International Journal of Heat and Fluid Flow, 1992. **13**(2): p. 106-115.
[33] Gao, N. and D. Ewing, *Investigation of the effect of confinement on the heat transfer to round impinging jets exiting a long pipe.* International Journal of Heat and Fluid Flow, 2006. **27**(1): p. 33-41.

[34] Hartnett, J.P., T.F. Irvine, and Y.I. Cho, *Advances in Heat Transfer*. 1993: Elsevier Science.
[35] Choo, K., T.Y. Kang, and S.J. Kim, *The effect of inclination on impinging jets at small nozzle-to-plate spacing.* International Journal of Heat and Mass Transfer, 2012. **55**(13–14): p. 3327-3334.
[36] San, J.-Y. and W.-Z. Shiao, *Effects of jet plate size and plate spacing on the stagnation Nusselt number for a confined circular air jet impinging on a flat surface.* International Journal of Heat and Mass Transfer, 2006. **49**(19–20): p. 3477-3486.
[37] Stevens, J. and B.W. Webb, *Local heat transfer coefficients under an axisymmetric, single-phase liquid jet.* Journal of Heat Transfer , Series C), 1991. **113**(1).
[38] Zhou, D.W. and S.-J. Lee, *Forced convective heat transfer with impinging rectangular jets.* International Journal of Heat and Mass Transfer, 2007. **50**(9): p. 1916-1926.
[39] Zukowski, M., *Heat transfer performance of a confined single slot jet of air impinging on a flat surface.* International Journal of Heat and Mass Transfer, 2013. **57**(2): p. 484-490.
[40] Lee, D.H., et al., *Heat transfer with fully developed slot jets impinging on confined concave and convex surfaces.* International Journal of Heat and Mass Transfer, 2015. **88**: p. 218-223.
[41] Gardon, R. and J.C. Akfirat, *Heat Transfer Characteristics of Impinging Two-Dimensional Air Jets.* Journal of Heat Transfer, 1966. **88**(1): p. 101-107.
[42] Lee, J., et al., *Effects of Jet-To-Target Plate Distance and Reynolds Number on Jet Array Impingement Heat Transfer.* Journal of Turbomachinery, 2014. **136**(5): p. 051013.
[43] Wilcox, D.C., *Turbulence modeling for CFD*. 2nd print., Nov. 1994 (with corr.). ed. 1994, La Cãnada, CA: La Cãnada, CA : DCW Industries, Inc.
[44] Hinze, J.O., *Turbulence*. 2d ed.. ed. 1975, New York: New York : McGraw-Hill.
[45] ANSYS, *17.1," Fluent Theory Guide "*. ANSYS Help Viewer, 2016.
[46] Spalart, P. and S. Allmaras, *A one-equation turbulence model for aerodynamic flows*, in *30th Aerospace Sciences Meeting and Exhibit*. 1992, American Institute of Aeronautics and Astronautics.
[47] Launder, B. and D. Spalding, *Lectures in mathematical models of turbulence, 1972*. Academic Press, London, England.
[48] Yakhot, V. and S.A. Orszag, *Renormalization group analysis of turbulence. I. Basic theory.* Journal of scientific computing, 1986. **1**(1): p. 3-51.
[49] Shih, T.-H., et al., *A new k-ϵ eddy viscosity model for high reynolds number turbulent flows.* Computers and Fluids, 1995. **24**(3): p. 227-238.
[50] Launder, B.E. and D.B. Spalding, *The numerical computation of turbulent flows.* Computer methods in applied mechanics and engineering, 1974. **3**(2): p. 269-289.
[51] Fidkowski, K.J. and D.L. Darmofal, *A triangular cut-cell adaptive method for high-order discretizations of the compressible Navier–Stokes equations.* Journal of Computational Physics, 2007. **225**(2): p. 1653-1672.

[52] Yang, Y.-T., T.-C. Wei, and Y.-H. Wang, *Numerical study of turbulent slot jet impingement cooling on a semi-circular concave surface.* International Journal of Heat and Mass Transfer, 2011. **54**(1): p. 482-489.
[53] G. Chochua, W.S.S.T.A.B.J.L.L.P.D.L., *A COMPUTATIONAL AND EXPERIMENTAL INVESTIGATION OF TURBULENT JET AND CROSSFLOW INTERACTION.* Numerical Heat Transfer, Part A: Applications, 2000. **38**(6): p. 557-572.
[54] Yang, G., M. Choi, and J.S. Lee, *An experimental study of slot jet impingement cooling on concave surface: effects of nozzle configuration and curvature.* International Journal of Heat and Mass Transfer, 1999. **42**(12): p. 2199-2209.
[55] Davis, J.W. and P.D. Smith, *ITER material properties handbook.* Journal of Nuclear Materials, 1996. **233**: p. 1593-1596.
[56] *Thermophysical Properties of Fluid Systems*. 2016 [cited 2017 04/11]; Available from: http://webbook.nist.gov/chemistry/fluid/.
[57] Burke, J.A., et al., *Optimization of the ARIES T-tube divertor concept.* Fusion Science and Technology, 2011. **60**(1): p. 213-217.
[58] Hermsmeyer, S. and K. Kleefeldt, *Review and comparative assessment of helium-cooled divertor concepts*. Vol. 6597. 2001: FZKA.
[59] Youchison, D.L., et al., *Thermal performance and flow instabilities in a multi-channel, helium-cooled, porous metal divertor module.* Fusion Engineering and Design, 2000. **49**: p. 407-415.
[60] Končar, B., P. Norajitra, and K. Oblak, *Effect of nozzle sizes on jet impingement heat transfer in He-cooled divertor.* Applied Thermal Engineering, 2010. **30**(6): p. 697-705.
[61] Gayton, E.F., *Experimental and numerical investigation of the thermal performance of the gas-cooled divertor plate concept*, E. Nuclear, Editor. 2009, Georgia Institute of Technology.